arXiv:1707.00372v5 [stat.ML] 25 Jan 2018

DEEP CONVOLUTIONAL FRAMELETS: A GENERAL DEEP LEARNING FRAMEWORK FOR INVERSE PROBLEMS*

JONG CHUL YE*†, YOSEOB HAN*, AND EUNJU CHA*

Abstract. Recently, deep learning approaches with various network architectures have achieved significant performance improvement over existing iterative reconstruction methods in various imaging problems. However, it is still unclear *why* these deep learning architectures work for specific inverse problems. Moreover, in contrast to the usual evolution of signal processing theory around the classical theories, the link between deep learning and the classical signal processing approaches such as wavelets, non-local processing, compressed sensing, etc, are not yet well understood. To address these issues, here we show that the long-searched-for missing link is the convolution framelets for representing a signal by convolving local and non-local bases. The convolution framelets was originally developed to generalize the theory of low-rank Hankel matrix approaches for inverse problems, and this paper further extends the idea so that we can obtain a deep neural network using multilayer convolution framelets with perfect reconstruction (PR) under rectilinear linear unit nonlinearity (ReLU). Our analysis also shows that the popular deep network components such as residual block, redundant filter channels, and concatenated ReLU (CReLU) do indeed help to achieve the PR, while the pooling and unpooling layers should be augmented with high-pass branches to meet the PR condition. Moreover, by changing the number of filter channels and bias, we can control the shrinkage behaviors of the neural network. This discovery reveals the limitations of many existing deep learning architectures for inverse problems, and leads us to propose a novel theory for *deep convolutional framelets* neural network. Using numerical experiments with various inverse problems, we demonstrated that our deep convolution framelets network shows consistent improvement over existing deep architectures. This discovery suggests that the success of deep learning is not from a magical power of a black-box, but rather comes from the power of a novel signal representation using non-local basis combined with data-driven local basis, which is indeed a natural extension of classical signal processing theory.

Key words. Convolutional neural network, framelets, deep learning, inverse problems, ReLU, perfect reconstruction condition

AMS subject classifications. Primary, 94A08, 97R40, 94A12, 92C55, 65T60, 42C40 ; Secondary, 44A12

1. Introduction.

Deep learning approaches have achieved tremendous success in classification problems [44] as well as low-level computer vision problems such as segmentation [59], denoising [76], super-resolution [42, 61], etc. The theoretical origin of its success has been investigated [58, 63], and the exponential expressivity under a given network complexity (in terms of VC dimension [3] or Rademacher complexity [5]) has been often attributed to its success. A deep network is also known to learn high-level abstractions/features of the data similar to the visual processing in human brain using multiple layers of neurons with non-linearity [47].

Inspired by the success of deep learning in low-level computer vision, several machine learning approaches have been recently proposed for image reconstruction problems. In X-ray computed tomography (CT), Kang et al [39] provided the first systematic study of deep convolutional neural network (CNN) for low-dose CT and showed that a deep CNN using directional wavelets is more efficient in removing low-dose related CT noises. Unlike these low-dose artifacts from reduced tube currents, the streaking artifacts originated from sparse projection views show globalized artifacts that are difficult to remove using conventional denoising CNNs [15, 52]. Han et al [29] and Jin et al [35] independently proposed a residual learning using U-Net [59] to remove the global streaking artifacts caused by sparse projection views. In MRI, Wang et al [67] was the first to apply deep learning to compressed sensing MRI (CS-MRI). They trained the deep neural network from downsampled reconstruction images to learn a fully sampled reconstruction. Then, they used the deep learning result either as an initialization or as a regularization term in classical CS approaches. Multilayer percep-

*The authors would like to thanks Dr. Cynthia MaCollough, the Mayo Clinic, the American Association of Physicists in Medicine (AAPM), and grant EB01705 and EB01785 from the National Institute of Biomedical Imaging and Bioengineering for providing the Low-Dose CT Grand Challenge data set. This work is supported by National Research Foundation of Korea, Grant number NRF-2016R1A2B3008104, NRF-2015M3A9A7029734, and NRF-2017M3C7A1047904.

*Bio Imaging and Signal Processing Lab., Department of Bio and Brain Engineering, Korea Advanced Institute of Science and Technology, 291 Daehak-ro, Yuseong-gu, Daejeon 34141, Republic of Korea (jong.ye@kaist.ac.kr; hanyoseob@kaist.ac.kr; eunju.cha@kaist.ac.kr).

†Address all correspondence to J. C. Ye at jong.ye@kaist.ac.kr, Ph.:+82-42-3504320, Fax:+82-42-3504310.

tron was developed for accelerated parallel MRI [46, 45]. Deep network architecture using unfolded iterative compressed sensing (CS) algorithm was also proposed [25]. Instead of using handcrafted regularizers, the authors in [25] tried to learn a set of optimal regularizers. Domain adaptation from sparse view CT network to projection reconstruction MRI was also proposed [30]. These pioneering works have consistently demonstrated impressive reconstruction performances, which are often superior to the existing iterative approaches. However, the more we have observed impressive empirical results in image reconstruction problems, the more unanswered questions we encounter. For example, to our best knowledge, we do not have the complete answers to the following questions that are critical to a network design:

1. What is the role of the filter channels in convolutional layers ?
2. Why do some networks need a fully connected layers whereas the others do not ?
3. What is the role of the nonlinearity such as rectified linear unit (ReLU) ?
4. Why do we need a pooling and unpooling in some architectures ?
5. What is the role of by-pass connection or residual network ?
6. How many layers do we need ?

Furthermore, the most troubling issue for signal processing community is that the link to the classical signal processing theory is still not fully understood. For example, wavelets [17] has been extensively investigated as an efficient signal representation theory for many image processing applications by exploiting energy compaction property of wavelet bases. Compressed sensing theory [19, 14] has further extended the idea to demonstrate that an accurate recovery is possible from undersampled data, if the signal is sparse in some frames and the sensing matrix is incoherent. Non-local image processing techniques such as non-local means [8], BM3D [16], etc have also demonstrated impressive performance for many image processing applications. The link between these algorithms have been extensively studied for last few years using various mathematical tools from harmonic analysis, convex optimization, etc. However, recent years have witnessed that a blind application of deep learning toolboxes sometimes provides even better performance than mathematics-driven classical signal processing approaches. Does this imply the dark age of signal processing or a new opportunity ?

Therefore, the main goal of this paper is to address these open questions. In fact, our paper is not the only attempt to address these issues. For instance, Papyan et al [56] showed that once ReLU nonlinearity is employed, the forward pass of a network can be interpreted as a deep sparse coding algorithm. Wiatowski et al [69] discusses the importance of pooling for networks, proving that it leads to translation invariance. Moreover, several works including [23] provided explanations for residual networks. The interpretation of a deep network in terms of unfolded (or unrolled) sparse recovery is another prevailing view in research community [24, 71, 25, 35]. However, this interpretation still does not give answers to several key questions: for example, why do we need multichannel filters ? In this paper, we therefore depart from this existing views and propose a new interpretation of a deep network as a novel *signal representation* scheme. In fact, signal representation theory such as wavelets and frames have been active areas of researches for many years [50], and Mallat [51] and Bruna et al [7] proposed the wavelet scattering network as a translation invariant and deformation-robust image representation. However, this approach does not have learning components as in the existing deep learning networks.

Then, what is missing here? One of the most important contributions of our work is to show that the geometry of deep learning can be revealed by *lifting* a signal to a high dimensional space using Hankel structured matrix. More specifically, many types of input signals that occur in signal processing can be factored into the left and right bases as well as a sparse matrix with energy compaction properties when lifted into the Hankel structure matrix. This results in a frame representation of the signal using the left and right bases, referred to as the non-local and local base matrices, respectively. The origin of this nomenclature will become clear later. One of our novel contributions was the realization that the non-local base determines the network architecture such as pooling/unpooling, while the local basis allows the network to learn convolutional filters. More specifically, the application-specific domain knowledge leads to a better choice of a non-local basis, on which to learn the local basis to maximize the performance.

In fact, the idea of exploiting the two bases by the so-called convolution framelets was originally proposed by Yin et al [74]. However, the aforementioned close link to the deep neural network was not revealed in [74]. Most importantly, we demonstrate for the first time that the convolution framelet representation can be equivalently represented as an encoder-decoder convolution layer, and multi-layer convolution framelet expansion is also feasible by relaxing the conditions in [74]. Furthermore, we derive the perfect reconstruction (PR) condition under rectified linear unit (ReLU). The mysterious role of the redundant multichannel filters can be then easily understood as an important tool to meet the PR condition. Moreover, by augmenting local filters with paired filters with opposite phase, the ReLU nonlinearity disappears and the deep convolutional framelet becomes a linear signal representation. However, in order for the deep network to satisfy the PR condition, the number of channels should increase exponentially along the layer, which is difficult to achieve in practice. Interestingly, we can show that an insufficient number of filter channels results in shrinkage behavior via a low rank approximation of an extended Hankel matrix, and this shrinkage behavior can be exploited to maximize network performance. Finally, to overcome the limitation of the pooling and unpooling layers, we introduce a multi-resolution analysis (MRA) for convolution framelets using wavelet non-local basis as a generalized pooling/unpooling. We call the new class of deep network using convolution framelets as the *deep convolutional framelets*.

1.1. Notations. For a matrix A, $R(A)$ denotes the range space of A and $N(A)$ refers to the null space of A. $P_{R(A)}$ denotes the projection to the range space of A, whereas $P_{R(A)}^{\perp}$ denotes the projection to the orthogonal complement of $R(A)$. The notation 1_n denotes a n-dimensional vector with 1's. The $n\times n$ identity matrix is referred to as $I_{n\times n}$. For a given matrix $A\in\mathbb{R}^{m\times n}$, the notation $A^{\dagger}$ refers to the generalized inverse. The superscript $^{\top}$ of $A^{\top}$ denotes the Hermitian transpose. Because we are mainly interested in real valued cases, $^{\top}$ is equivalent to the transpose ^{T}. The inner product in matrix space is defined by $\langle A,B\rangle = \mathrm{Tr}(A^{\top}B)$, where $A,B\in\mathbb{R}^{n\times m}$. For a matrix A, $\|A\|_F$ denotes its Frobenius norm. For a given matrix $C\in\mathbb{R}^{n\times m}$, c_j denotes its j-th column, and c_{ij} is the (i,j) elements of C. If a matrix $\Psi\in\mathbb{R}^{pd\times q}$ is partitioned as $\Psi=\begin{bmatrix}\Psi_1^{\top} & \cdots & \Psi_p^{\top}\end{bmatrix}^{\top}$ with sub-matrix $\Psi_i\in\mathbb{R}^{d\times q}$, then ψ_j^i refers to the j-th column of Ψ_i. A vector $\overline{v}\in\mathbb{R}^n$ is referred to the flipped version of a vector $v\in\mathbb{R}^n$, i.e. its indices are reversed. Similarly, for a given matrix $\Psi\in\mathbb{R}^{d\times q}$, the notation $\overline{\Psi}\in\mathbb{R}^{d\times q}$ refers to a matrix composed of flipped vectors, i.e. $\overline{\Psi}=\begin{bmatrix}\overline{\psi}_1 & \cdots & \overline{\psi}_q\end{bmatrix}$. For a block structured matrix $\Psi\in\mathbb{R}^{pd\times q}$, with a slight abuse of notation, we define $\overline{\Psi}$ as

$$\overline{\Psi}=\begin{bmatrix}\overline{\Psi}_1\\ \vdots\\ \overline{\Psi}_p\end{bmatrix},\quad \text{where}\quad \overline{\Psi}_i=\begin{bmatrix}\overline{\psi_1^i} & \cdots & \overline{\psi_q^i}\end{bmatrix}\in\mathbb{R}^{d\times q}. \tag{1}$$

Finally, Table 1 summarizes the notation used throughout the paper.

2. Mathematics of Hankel matrix. Since the Hankel structured matrix is the key component in our theory, this section discusses various properties of the Hankel matrix that will be extensively used throughout the paper.

2.1. Hankel matrix representation of convolution. Hankel matrices arise repeatedly from many different contexts in signal processing and control theory, such as system identification [21], harmonic retrieval, array signal processing [33], subspace-based channel identification [64], etc. A Hankel matrix can be also obtained from a convolution operation [72], which is of particular interest in this paper. Here, to avoid special treatment of boundary condition, our theory is mainly derived using the circular convolution.

Let $f=[f[1],\cdots,f[n]]^T\in\mathbb{R}^n$ and $\psi=[\psi[1],\cdots,\psi[d]]^T\in\mathbb{R}^d$. Then, a single-input single-output (SISO) convolution of the input f and the filter $\overline{\psi}$ can be represented in a matrix form:

$$y=f\circledast\overline{\psi}=\mathbb{H}_d(f)\psi\ , \tag{2}$$

Notation	Definition
Φ	non-local basis matrix at the encoder
$\tilde{\Phi}$	non-local basis matrix at the decoder
Ψ	local basis matrix at the encoder
$\tilde{\Psi}$	local basis matrix at the decoder
b_{enc}, b_{dec}	encoder and decoder biases
ϕ_i	i-th non-local basis or filter at the encoder
$\tilde{\phi}_i$	i-th non-local basis or filter at the decoder
ψ_i	i-th local basis or filter at the encoder
$\tilde{\psi}_i$	i-th local basis or filter at the decoder
C	convolutional framelet coefficients at the encoder
$\tilde{C}$	convolutional framelet coefficients at the decoder
n	input dimension
d	convolutional filter length
p	number of input channels
q	number of output channels
f	single channel input signal, i.e. $f \in \mathbb{R}^n$
Z	a p-channel input signal, i.e. $Z \in \mathbb{R}^{n\times p}$
$\mathbb{H}_d(\cdot)$	Hankel operator, i.e. $\mathbb{H}_d : \mathbb{R}^n \mapsto Y \subset \mathbb{R}^{n\times d}$
$\mathbb{H}_{d\|p}(\cdot)$	extended Hankel operator, i.e. $\mathbb{H}_{d\|p} : \mathbb{R}^{n\times p} \mapsto Y \subset \mathbb{R}^{n\times pd}$
$\mathbb{H}_d^\dagger(\cdot)$	generalized inverse of Hankel operator, i.e. $\mathbb{H}_d^\dagger : \mathbb{R}^{n\times d} \mapsto \mathbb{R}^n$
$\mathbb{H}_{d\|p}^\dagger(\cdot)$	generalized inverse of an extended Hankel operator, i.e. $\mathbb{H}_{d\|p}^\dagger : \mathbb{R}^{n\times pd} \mapsto \mathbb{R}^{n\times p}$
U	left singular vector matrix of an (extended) Hankel matrix
V	right singular vector matrix of an (extended) Hankel matrix
Σ	singular value matrix of an (extended) Hankel matrix
$\mathfrak{C}_d(\cdot)$	$n \times d$-circulant matrix

TABLE 1
Notation and definition used throughout the paper.

where $\mathbb{H}_d(f)$ is a wrap-around Hankel matrix:

$$\mathbb{H}_d(f) = \begin{bmatrix} f[1] & f[2] & \cdots & f[d] \\ f[2] & f[3] & \cdots & f[d+1] \\ \vdots & \vdots & \ddots & \vdots \\ f[n] & f[1] & \cdots & f[d-1] \end{bmatrix} \tag{3}$$

Similarly, a single-input multi-output (SIMO) convolution using q filters $\overline{\psi}_1, \cdots, \overline{\psi}_q \in \mathbb{R}^d$ can be represented by

$$Y = f \circledast \overline{\Psi} = \mathbb{H}_d(f)\Psi \tag{4}$$

where

$$Y := \begin{bmatrix} y_1 & \cdots & y_q \end{bmatrix} \in \mathbb{R}^{n\times q}, \ \Psi := \begin{bmatrix} \psi_1 & \cdots & \psi_q \end{bmatrix} \in \mathbb{R}^{d\times q}.$$

On the other hand, multi-input multi-output (MIMO) convolution for the p-channel input $Z = [z_1, \cdots, z_p]$ can be represented by

$$y_i = \sum_{j=1}^{p} z_j \circledast \overline{\psi}_i^j, \quad i = 1, \cdots, q \tag{5}$$

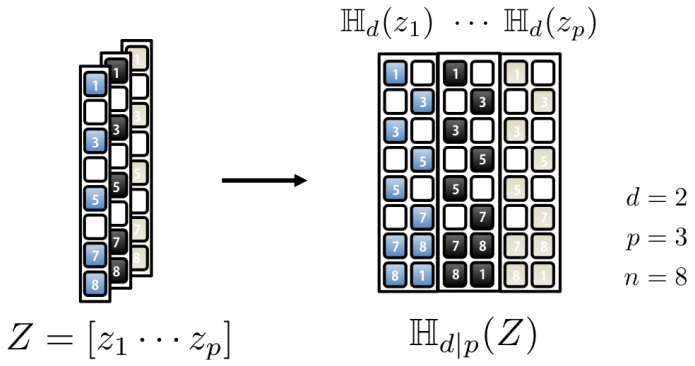


FIG. 1. *Construction of an extended Hankel matrix for 1-D multi-channel input patches.*

where p and q are the number of input and output channels, respectively; $\overline{\psi}_i^j \in \mathbb{R}^d$ denotes the length d- filter that convolves the j-th channel input to compute its contribution to the i-th output channel. By defining the MIMO filter kernel Φ as follows:

$$\Psi = \begin{bmatrix} \Psi_1 \\ \vdots \\ \Psi_p \end{bmatrix} \quad \text{where} \quad \Psi_j = \begin{bmatrix} \psi_1^j & \cdots & \psi_q^j \end{bmatrix} \in \mathbb{R}^{d \times q} \tag{6}$$

the corresponding matrix representation of the MIMO convolution is then given by

$$Y = Z \circledast \overline{\Psi} \tag{7}$$

$$= \sum_{j=1}^{p} \mathbb{H}_d(z_j) \Psi_j \tag{8}$$

$$= \mathbb{H}_{d|p}(Z)\, \Psi \tag{9}$$

where $\overline{\Psi}$ is a flipped block structured matrix in the sense of (1), and $\mathbb{H}_{d|p}(Z)$ is an *extended Hankel matrix* by stacking p Hankel matrices side by side:

$$\mathbb{H}_{d|p}(Z) := \begin{bmatrix} \mathbb{H}_d(z_1) & \mathbb{H}_d(z_2) & \cdots & \mathbb{H}_d(z_p) \end{bmatrix} . \tag{10}$$

For notational simplicity, we denote $\mathbb{H}_{d|1}([z]) = \mathbb{H}_d(z)$. Fig. 1 illustrates the procedure to construct an extended Hankel matrix from $[z_1, z_2, z_3] \in \mathbb{R}^{8\times 3}$ when the convolution filter length d is 2.

Finally, as a special case of MIMO convolution for $q = 1$, the multi-input single-output (MISO) convolution is defined by

$$y = \sum_{j=1}^{p} z_j \circledast \overline{\psi}^j = Z \circledast \Psi = \mathbb{H}_{d|p}(Z)\, \Psi \tag{11}$$

where

$$\Psi = \begin{bmatrix} \psi^1 \\ \vdots \\ \psi^p \end{bmatrix} .$$

The SISO, SIMO, MIMO, and MISO convolutional operations are illustrated in Fig. 2(a)-(d).

The extension to the multi-channel 2-D convolution operation for an image domain CNN (and multi-dimensional convolutions in general) is straight-forward, since similar matrix vector operations can be also used. Only required change is the definition of the (extended) Hankel matrices, which is

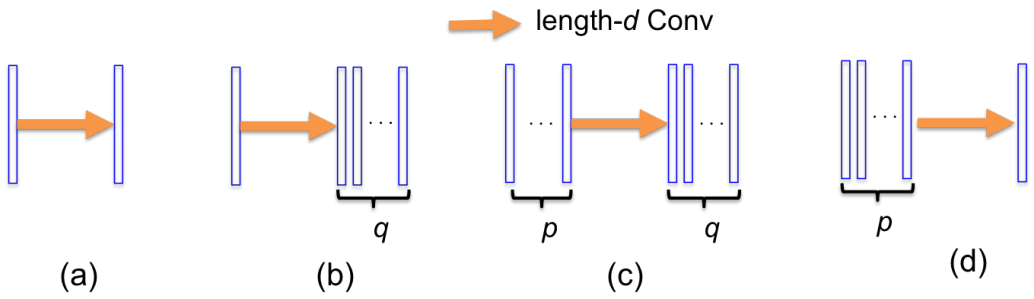


FIG. 2. *1-D convolutional operations and their Hankel matrix representations. (a) Single-input single-output convolution* $y = f \circledast \overline{\psi}$*, (b) SIMO convolution* $Y = f \circledast \overline{\Psi}$*, (c) MIMO convolution* $Y = Z \circledast \overline{\Psi}$*, and (d) MISO convolution* $y = Z \circledast \overline{\Psi}$*,*

now defined as *block* Hankel matrix. Specifically, for a 2-D input $X = [x_1, \cdots, x_{n_2}] \in \mathbb{R}^{n_1 \times n_2}$ with $x_i \in \mathbb{R}^{n_1}$, the block Hankel matrix associated with filtering with $d_1 \times d_2$ filter is given by

$$\mathbb{H}_{d_1,d_2}(X) = \begin{bmatrix} \mathbb{H}_{d_1}(x_1) & \mathbb{H}_{d_1}(x_2) & \cdots & \mathbb{H}_{d_1}(x_{d_2}) \\ \mathbb{H}_{d_1}(x_2) & \mathbb{H}_{d_1}(x_3) & \cdots & \mathbb{H}_{d_1}(x_{d_2+1}) \\ \vdots & \vdots & \ddots & \vdots \\ \mathbb{H}_{d_1}(x_{n_2}) & \mathbb{H}_{d_1}(x_1) & \cdots & \mathbb{H}_{d_1}(x_{d_2-1}) \end{bmatrix} \in \mathbb{R}^{n_1 n_2 \times d_1 d_2}. \tag{12}$$

Similarly, an extended block Hankel matrix from the p-channel $n_1 \times n_2$ input image $X^{(i)} = [x_1^{(i)}, \cdots, x_{n_2}^{(i)}], i = 1, \cdots, p$ is defined by

$$\mathbb{H}_{d_1,d_2|p}\left([X^{(1)} \cdots X^{(p)}]\right) = \begin{bmatrix} \mathbb{H}_{d_1,d_2}(X^{(1)}) & \cdots & \mathbb{H}_{d_1,d_2}(X^{(p)}) \end{bmatrix} \in \mathbb{R}^{n_1 n_2 \times d_1 d_2 p}. \tag{13}$$

Then, the output $Y \in \mathbb{R}^{n_1 \times n_2}$ from the 2-D SISO convolution for a given image $X \in \mathbb{R}^{n_1 \times n_2}$ with 2-D filter $\overline{K} \in \mathbb{R}^{d_1 \times d_2}$ can be represented by a matrix vector form:

$$\text{VEC}(Y) = \mathbb{H}_{d_1,d_2}(X)\text{VEC}(K)$$

where $\text{VEC}(Y)$ denotes the vectorization operation by stacking the column vectors of the 2-D matrix Y. Similarly, 2-D MIMO convolution for given p input images $X^{(j)} \in \mathbb{R}^{n_1 \times n_2}, j = 1, \cdots, p$ with 2-D filter $\overline{K}_{(i)}^{(j)} \in \mathbb{R}^{d_1 \times d_2}$ can be represented by a matrix vector form:

$$\text{VEC}(Y^{(i)}) = \sum_{j=1}^{p} \mathbb{H}_{d_1,d_2}(X^{(j)})\text{VEC}(K_{(i)}^{(j)}), \quad i = 1, \cdots, q \tag{14}$$

Therefore, by defining

$$\mathcal{Y} = \begin{bmatrix} \text{VEC}(Y^{(1)}) & \cdots & \text{VEC}(Y^{(q)}) \end{bmatrix} \tag{15}$$

$$\mathcal{K} = \begin{bmatrix} \text{VEC}(K_{(1)}^{(1)}) & \cdots & \text{VEC}(K_{(q)}^{(1)}) \\ \vdots & \ddots & \vdots \\ \text{VEC}(K_{(1)}^{(p)}) & \cdots & \text{VEC}(K_{(q)}^{(p)}) \end{bmatrix} \tag{16}$$

the 2-D MIMO convolution can be represented by

$$\mathcal{Y} = \mathbb{H}_{d_1,d_2|p}\left([X^{(1)} \cdots X^{(p)}]\right)\mathcal{K}. \tag{17}$$

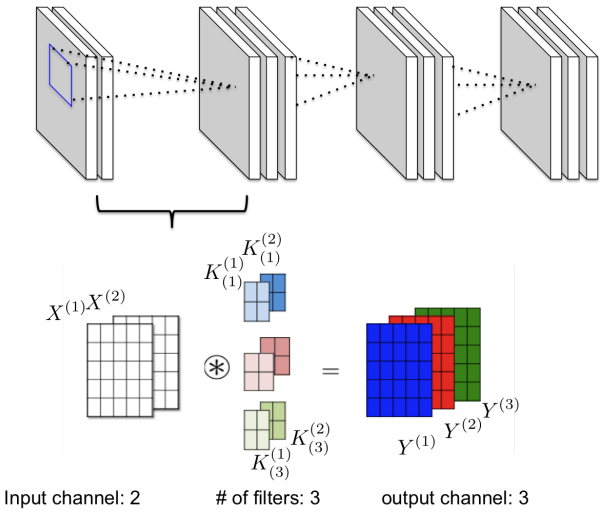


FIG. 3. *2-D CNN convolutional operation. For the first layer filter, the input and output channel numbers are* $p = 2, q = 3$*, respectively, and the filter dimension is* $d_1 = d_2 = 2$*. Thus, the corresponding convolution operation can be represented by* $\text{VEC}(Y^{(j)}) = \sum_{i=1}^{2} \mathbb{H}_{d_1,d_2}\left(X^{(i)}\right) \text{VEC}(K^{(i)}_{(j)})$ *where* $X^{(i)}$ *and* $Y^{(j)}$ *denotes the* i*-th input and* j*-th output channel image, respectively; and* $K^{(i)}_{(j)}$ *denotes the* i*-th input channel filter to yield* j*-th channel output.

Due to these similarities between 1-D and 2-D convolutions, we will therefore use the 1-D notation throughout the paper for the sake of simplicity; however, readers are advised that the same theory applies to 2-D cases.

In convolutional neural networks (CNN), unique multi-dimensional convolutions are used. Specifically, to generate q output channels from p input channels, each channel output is computed by first convolving p- 2D filters and p- input channel images, and then applying the weighted sum to the outputs (which is often referred to as 1×1 convolution). For 1-D signals, this operation can be written by

$$y_i = \sum_{j=1}^{p} w_j \left(z_j \circledast \overline{\psi}_i^j \right), \quad i = 1, \cdots, q \tag{18}$$

where w_j denotes the 1-D weighting. Note that this is equivalent to an MIMO convolution, since we have

$$\begin{aligned} Y &= \sum_{j=1}^{p} w_j \mathbb{H}_d(z_j) \Psi_j \\ &= \sum_{j=1}^{p} \mathbb{H}_d(z_j) \Psi_j^w \\ &= \mathbb{H}_{d|p}\left(Z\right) \Psi^w = Z \circledast \overline{\Psi}^w \end{aligned} \tag{19}$$

where

$$\overline{\Psi}^w = \begin{bmatrix} w_1 \overline{\Psi}_1 \\ \vdots \\ w_p \overline{\Psi}_p \end{bmatrix} . \tag{20}$$

The aforementioned matrix vector operations using the extended Hankel matrix also describe the filtering operation (14) in 2-D CNNs as shown in Fig. 3.

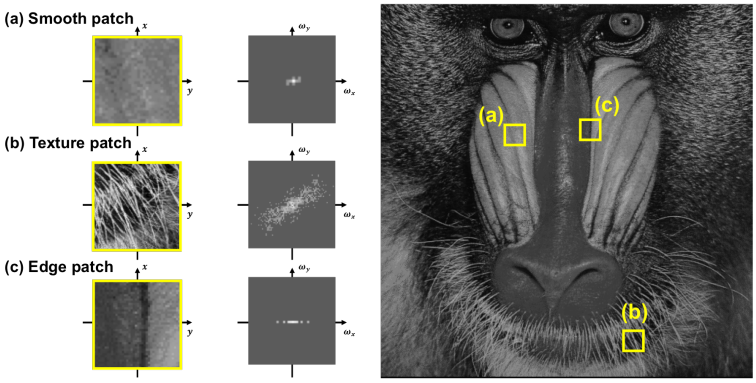


FIG. 4. *Spectral components of patches from (a) smooth background, (b) texture, and (c) edge.*

Throughout the paper, we denote the space of the wrap-around Hankel structure matrices of the form in (3) as $\mathcal{H}(n,d)$, and an extended Hankel matrix composed of p Hankel matrices of the form in (10) as $\mathcal{H}(n,d;p)$. The basic properties of Hankel matrix used in this paper are described in Lemma 14 in Appendix A. In the next section, we describe advanced properties of the Hankel matrix that will be extensively used in this paper.

2.2. Low-rank property of Hankel Matrices. One of the most intriguing features of the Hankel matrix is that it often has a low-rank structure and its low-rankness is related to the sparsity in the Fourier domain (for the case of Fourier samples, it is related to the sparsity in the spatial domain)[72, 37].

Note that many types of image patches have sparsely distributed Fourier spectra. For example, as shown in Fig. 4(a), a smoothly varying patch usually has spectrum content in the low-frequency regions, while the other frequency regions have very few spectral components. Similar spectral domain sparsity can be observed in the texture patch shown in Fig. 4(b), where the spectral components of patch are determined by the spectrum of the patterns. For the case of an abrupt transition along the edge as shown in Fig. 4(c), the spectral components are mostly localized along the ω_x axis. In these cases, if we construct a Hankel matrix using the corresponding image patch, the resulting Hankel matrix is low-ranked [72]. This property is extremely useful as demonstrated by many applications [37, 34, 55, 48, 49, 36]. For example, this idea can be used for image denoising [38] and deconvolution [53] by modeling the underlying intact signals to have low-rank Hankel structure, from which the artifacts or blur components can be easily removed.

In order to understand this intriguing relationship, consider a 1-D signal, whose spectrum in the Fourier domain is sparse and can be modelled as the sum of Diracs:

$$\hat{f}(\omega) = 2\pi \sum_{j=0}^{r-1} c_j \delta(\omega - \omega_j) \qquad \omega_j \in [0, 2\pi], \tag{21}$$

where $\{\omega_j\}_{j=0}^{r-1}$ refer to the corresponding harmonic components in the Fourier domain. Then, the corresponding discrete time-domain signal is given by:

$$f[k] = \sum_{j=0}^{r-1} c_j e^{-ik\omega_j} \ . \tag{22}$$

Suppose that we have a $r+1$-length filter $h[k]$ which has the following z-transform representation [66]:

$$\hat{h}(z) = \sum_{l=0}^{r} h[l] z^{-l} = \prod_{j=0}^{r-1} (1 - e^{-i\omega_j} z^{-1}) \ . \tag{23}$$

Then, it is easy to see that

$$(f \circledast h)[k] = 0, \quad \forall k, \tag{24}$$

because

$$\begin{aligned}(h * f)[k] &= \sum_{l=0}^{r} h[l] f[k-l] \\ &= \sum_{l=0}^{r} \sum_{j=0}^{r-1} c_j h[l] u_j^{k-l} \\ &= \sum_{j=0}^{r-1} c_j \underbrace{\left(\sum_{l=0}^{r} h[p] u_j^{-l} \right)}_{\hat{h}(u_j)} u_j^k = 0 \end{aligned} \tag{25}$$

where $u_j = e^{-i\omega_j}$ and the last equality comes from (23) [66]. Thus, the filter h annihilates the signal f, so it is referred to as the *annihilating filter*. Moreover, using the notation in (2), Eq. (24) can be represented by

$$\mathbb{H}_d(f)\overline{h} = 0 \quad .$$

This implies that Hankel matrix $\mathbb{H}_d(f)$ is rank-deficient. In fact, the rank of the Hankel matrix can be explicitly calculated as shown in the following theorem:

THEOREM 1. *[72] Let $r+1$ denote the minimum length of annihilating filters that annihilates the signal $f = [f[1], \cdots, f[n]]^T$. Then, for a given Hankel structured matrix $\mathbb{H}_d(f) \in \mathcal{H}(n,d)$ with $d > r$, we have*

$$\text{RANK}\mathbb{H}_d(f) = r, \tag{26}$$

where RANK$(\cdot)$ *denotes a matrix rank.*

Thus, if we choose a sufficiently large d, the resulting Hankel matrix is low-ranked. This relationship is quite general, and Ye et al [72] further showed that the rank of the associated Hankel matrix $\mathbb{H}_d(f)$ is r if and only if f can be represented by

$$f[k] = \sum_{j=0}^{p-1} \sum_{l=0}^{m_j-1} c_{j,l} k^l \lambda_j{}^k \ , \quad \text{where} \quad r = \sum_{j=0}^{p-1} m_j \ < d \tag{27}$$

for some $|\lambda_j| \leq 1,\ j = 1, \cdots, m_j$. If $\lambda_j = e^{-i\omega_j}$, then it is directly related to the signals with the finite rate of innovations (FRI) [66]. Thus, the low-rank Hankel matrix provides an important link between FRI sampling theory and compressed sensing such that a sparse recovery problem can be solved using the measurement domain low-rank interpolation [72].

In [34], we also showed that the rank of the extended Hankel matrix in (10) is low, when the multiple signals $Z = [z_1, \cdots z_p]$ has the following structure:

$$\hat{z}_i = f \circledast \overline{h}_i, \quad i = 1, \cdots, p \tag{28}$$

such that the Hankel matrix $\mathbb{H}_d(z_i)$ has the following decomposition:

$$\mathbb{H}_d(z_i) = \mathbb{H}_n(f)\mathfrak{C}_d(h_i) \quad \in \mathbb{C}^{n\times d} \tag{29}$$

where $\mathbb{H}_n(f)$ is $n \times n$ wrap-around Hankel matrix, and $\mathfrak{C}_d(h)$ for any $h \in \mathbb{R}^m$ with $m \leq n$ is defined

by

$$\mathfrak{C}_d(h) = \overbrace{\begin{bmatrix} h[1] & \cdots & 0 \\ \vdots & \ddots & 0 \\ h[m] & \ddots & h[1] \\ 0 & \ddots & \vdots \\ \vdots & \vdots & h[m] \\ \vdots & \vdots & \vdots \\ 0 & 0 & 0 \end{bmatrix}}^{d} \in \mathbb{C}^{n\times d} . \tag{30}$$

Accordingly, the extended Hankel matrix $\mathbb{H}_{d|p}(Z)$ has the following decomposition:

$$\mathbb{H}_{d|p}(Z) = \mathbb{H}_n(f) \begin{bmatrix} \mathfrak{C}_d(h_1) & \cdots & \mathfrak{C}_d(h_p) \end{bmatrix} . \tag{31}$$

Due to the rank inequality $\text{RANK}(AB) \leq \min\{\text{RANK}(A), \text{RANK}(B)\}$, we therefore have the following rank bound:

$$\begin{aligned} \text{RANK}\mathbb{H}_{d|p}(Z) &\leq \min\{\text{RANK}\mathbb{H}_n(f), \text{RANK} \begin{bmatrix} \mathfrak{C}(h_1) & \cdots & \mathfrak{C}(h_p) \end{bmatrix}\} \\ &= \min\{r, pd\} \quad . \end{aligned} \tag{32}$$

Therefore, if the filter length d is chosen such that the number of column of the extended matrix is sufficiently large, i.e. $pd > r$, then the concatenated matrix becomes low-ranked.

Note that the low-rank Hankel matrix algorithms are usually performed in a patch-by-patch manner [38, 37]. It is also remarkable that this is similar to the current practice of deep CNN for low level computer vision applications, where the network input is usually given as a patch. Later, we will show that this is not a coincidence; rather it suggests an important link between the low-rank Hankel matrix approach and a CNN.

2.3. Hankel matrix decomposition and the convolution framelets. The last but not least important property of Hankel matrix is that a Hankel matrix decomposition results in a framelet representation whose bases are constructed by the convolution of so-called local and non-local bases [74]. More specifically, for a given input vector $f \in \mathbb{R}^n$, suppose that the Hankel matrix $\mathbb{H}_d(f)$ with the rank $r < d$ has the following singular value decomposition:

$$\mathbb{H}_d(f) = U\Sigma V^\top \tag{33}$$

where $U = [u_1 \cdots u_r] \in \mathbb{R}^{n\times r}$ and $V = [v_1 \cdots v_r] \in \mathbb{R}^{d\times r}$ denote the left and right singular vector bases matrices, respectively; and $\Sigma \in \mathbb{R}^{r\times r}$ is the diagonal matrix whose diagonal components contains the singular values. Then, by multiplying $U^\top$ and V to the left and right of the Hankel matrix, we have

$$\Sigma = U^\top \mathbb{H}_d(f) V \ . \tag{34}$$

Note that the (i, j)-th element of Σ is given by

$$\sigma_{ij} = u_i^\top \mathbb{H}_d(f) v_j = \langle f, u_i \circledast v_j \rangle, \quad 1 \leq i, j \leq r \ , \tag{35}$$

where the last equality comes from (A.3). Since the number of rows and columns of $\mathbb{H}_d(f)$ are n and d, the right-multiplied vector v_j interacts locally with the d neighborhood of the f vector, whereas the left-multiplied vector u_i has a global interaction with the entire n-elements of the f vector. Accordingly, (35) represents the strength of simultaneous global and local interaction of the signal f with bases. Thus, we call u_i and v_j as *non-local* and *local* bases, respectively.

This relation holds for arbitrary bases matrix $\Phi = [\phi_1, \cdots, \phi_m] \in \mathbb{R}^{n\times n}$ and $\Psi = [\psi_1, \cdots, \psi_d] \in \mathbb{R}^{d\times d}$ that are multiplied to the left and right of the Hankel matrix, respectively, to yield the coefficient matrix:

$$c_{ij} = \phi_i^\top \mathbb{H}_d(f)\psi_j = \langle f, \phi_i \circledast \psi_j \rangle, \quad i = 1, \cdots, n, \ j = 1, \cdots, d, \tag{36}$$

which represents the interaction of f with the non-local basis ϕ_i and local basis ψ_j. Using (36) as expansion coefficients, Yin et al derived the following signal expansion, which they called the *convolution framelet* expansion [74]:

PROPOSITION 2 ([74]). *Let ϕ_i and ψ_j denotes the i-th and j-th columns of orthonormal matrix $\Phi \in \mathbb{R}^{n\times n}$ and $\Psi \in \mathbb{R}^{d\times d}$, respectively. Then, for any n-dimensional vector $f \in \mathbb{R}^n$,*

$$f = \frac{1}{d}\sum_{i=1}^{n}\sum_{j=1}^{d}\langle f, \phi_i \circledast \psi_j\rangle \phi_i \circledast \psi_j \tag{37}$$

Furthermore, $\phi_i \circledast \psi_j$ with $i = 1, \cdots, n; j = 1, \cdots, d$ form a tight frame for $\mathbb{R}^n$ with the frame constant d.

This implies that any input signal $f \in \mathbb{R}^n$ can be expanded using the convolution frame $\phi_i \circledast \psi_j$ and the expansion coefficient $\langle f, \phi_i \circledast \psi_j\rangle$. Although the framelet coefficient matrix $[c_{ij}]$ in (36) for general non-local and local bases is not as sparse as (34) from SVD bases, Yin et al [74] showed that the framelet coefficients can be made sufficiently sparse by optimally learning Ψ for a given non-local basis Φ. Therefore, the choice of the non-local bases is one of the key factors in determining the efficiency of the framelet expansion. In the following, several examples of non-local bases Φ in [74] are discussed.

- SVD: From the singular value decomposition in (33), the SVD basis is constructed by augmenting the left singular vector basis $U \in \mathbb{R}^{n\times r}$ with an orthogonal matrix $U_{ext} \in \mathbb{R}^{n\times(n-r)}$:

  $$\Phi_{SVD} = \begin{bmatrix} U & U_{ext} \end{bmatrix}$$

  such that $\Phi_{SVD}^\top \Phi_{SVD} = I$. Thanks to (35), this is the most energy compacting basis. However, the SVD basis is input-signal dependent and the calculation of the SVD is computationally expensive.
- Haar: Haar basis comes from the Haar wavelet transform and is constructed as follows:

  $$\Phi = \begin{bmatrix} \Phi_{low} & \Phi_{high} \end{bmatrix},$$

  where the low-pass and high-pass operators $\Phi_{low}, \Phi_{high} \in \mathbb{R}^{n\times\frac{n}{2}}$ are defined by

  $$\Phi_{low} = \frac{1}{\sqrt{2}}\begin{bmatrix} 1 & 0 & \cdots & 0 \\ 1 & 0 & \cdots & 0 \\ 0 & 1 & \cdots & 0 \\ 0 & 1 & \cdots & 0 \\ \vdots & \vdots & \ddots & \vdots \\ 0 & 0 & \cdots & 1 \\ 0 & 0 & \vdots & 1 \end{bmatrix}, \quad \Phi_{high} = \frac{1}{\sqrt{2}}\begin{bmatrix} 1 & 0 & \cdots & 0 \\ -1 & 0 & \cdots & 0 \\ 0 & 1 & \cdots & 0 \\ 0 & -1 & \cdots & 0 \\ \vdots & \vdots & \ddots & \vdots \\ 0 & 0 & \cdots & 1 \\ 0 & 0 & \vdots & -1 \end{bmatrix}$$

  Note that the non-zero elements of each column of Haar basis is two, so one level of Haar decomposition does not represent a global interaction. However, by cascading the Haar basis, the interaction becomes global, resulting in a multi-resolution decomposition of the input signal. Moreover, Haar basis is a useful global basis because it can sparsify the piecewise constant signals. Later, we will show that the average pooling operation is closely related to the Haar basis.

- DCT: The discrete cosine transform (DCT) basis is an interesting global basis proposed by Yin et al [74] due to its energy compaction property proven by JPEG image compression standard. The DCT bases matrix is a fully populated dense matrix, which clearly represents a global interaction. To the best of our knowledge, the DCT basis have never been used in deep CNN, which could be an interesting direction of research.

In addition to the non-local bases used in [74], we will also investigate the following non-local bases:

- Identity matrix: In this case, $\Phi = I_{n\times n}$, so there is no global interaction between the basis and the signal. Interestingly, this non-local basis is quite often used in CNNs that do not have a pooling layer. In this case, it is believed that the local structure of the signal is more important and local-bases are trained such that they can maximally capture the local correlation structure of the signal.
- Learned basis: In extreme case where we do not have specific knowledge of the signal, the non-local bases can be also learnt. However, a care must be taken, since the learned non-local basis has size of $n \times n$ that quickly becomes very large for image processing applications. For example, if one is interested in processing 512×512 (i.e. $n = 2^9 \times 2^9$) image, the required memory to store the learnable non-local basis becomes 2^{37}, which is not possible to store or estimate. However, if the input patch size is sufficiently small, this may be another interesting direction of research in deep CNN.

3. Main Contributions: Deep Convolutional Framelets Neural Networks. In this section, which is our main theoretical contribution, we will show that the convolution framelets by Yin et al [74] is directly related to the deep neural network if we relax the condition of the original convolution framelets to allow multilayer implementation. The multi-layer extension of convolution framelets, which we call the *deep convolutional framelet*, can explain many important components of deep learning.

3.1. Deep Convolutional Framelet Expansion. While the original convolution framelets by Yin et al [74] exploits the advantages of the low rank Hankel matrix approaches using two bases, there are several limitations. First, their convolution framelet uses only orthonormal basis. Second, the significance of multi-layer implementation was not noticed. Here, we discuss its extension to relax these limitations. As will become clear, this is a basic building step toward a deep convolutional framelets neural network.

PROPOSITION 3. *Let $\Phi = [\phi_1, \cdots, \phi_m] \in \mathbb{R}^{n\times m}$ and $\Psi = [\psi_1, \cdots, \psi_q] \in \mathbb{R}^{d\times q}$ denote the non-local and local bases matrices, respectively. Suppose, furthermore, that $\tilde{\Phi} = [\tilde{\phi}_1, \cdots, \tilde{\phi}_m] \in \mathbb{R}^{n\times m}$ and $\tilde{\Psi} = [\tilde{\psi}_1, \cdots, \tilde{\psi}_q] \in \mathbb{R}^{d\times q}$ denote their* dual bases *matrices such that they satisfy the frame condition:*

$$\tilde{\Phi}\Phi^\top = \sum_{i=1}^{m} \tilde{\phi}_i \phi_i^\top = I_{n\times n}, \tag{38}$$

$$\Psi\tilde{\Psi}^\top = \sum_{j=1}^{q} \psi_j \tilde{\psi}_j^\top = I_{d\times d} \ . \tag{39}$$

Then, for any input signal $f \in \mathbb{R}^n$, we have

$$f = \frac{1}{d}\sum_{i=1}^{m}\sum_{j=1}^{q} \langle f, \phi_i \circledast \psi_j\rangle \tilde{\phi}_i \circledast \tilde{\psi}_j \ , \tag{40}$$

or equivalently,

$$f = \frac{1}{d}\sum_{i=1}^{m} \left(\tilde{\Phi} c_j\right) \circledast \tilde{\psi}_j \ , \tag{41}$$

where c_j is the j-th column of the framelet coefficient matrix

$$C = \Phi^\top \left(f \circledast \overline{\Psi}\right) \tag{42}$$

$$= \begin{bmatrix} \langle f, \phi_1 \circledast \psi_1 \rangle & \cdots & \langle f, \phi_1 \circledast \psi_q \rangle \\ \vdots & \ddots & \vdots \\ \langle f, \phi_m \circledast \psi_1 \rangle & \cdots & \langle f, \phi_m \circledast \psi_q \rangle \end{bmatrix} \in \mathbb{R}^{m \times q} \quad . \tag{43}$$

Proof. Using the frame condition (38) and (39), we have

$$\mathbb{H}_d(f) = \tilde{\Phi}\Phi^\top \mathbb{H}_d(f)\Psi\tilde{\Psi}^\top = \tilde{\Phi}C\tilde{\Psi}^\top \ ,$$

where $C \in \mathbb{R}^{m\times q}$ denotes the framelet coefficient matrix computed by

$$C = \Phi^\top \mathbb{H}_d(f)\Psi = \Phi^\top \left(f \circledast \overline{\Psi}\right)$$

and its (i,j)-th element is given by

$$c_{ij} = \phi_i^\top \mathbb{H}_d(f)\psi_j = \langle f, \phi_i \circledast \psi_j \rangle$$

where we use (A.3) for the last equality. Furthermore, using (A.6) and (A.7), we have

$$\begin{aligned} f = \mathbb{H}_d^\dagger \left(\mathbb{H}_d(f)\right) = \mathbb{H}_d^\dagger \left(\tilde{\Phi}C\tilde{\Psi}^\top\right) \\ &= \frac{1}{d}\sum_{j=1}^{q} \left(\tilde{\Phi}c_j\right) \circledast \tilde{\psi_j} \\ &= \sum_{i=1}^{m}\sum_{j=1}^{q} \langle f, \phi_i \circledast \psi_j \rangle \tilde{\phi_i} \circledast \tilde{\psi_j} \end{aligned}$$

This concludes the proof. ∎

Note that the so-called perfect recovery condition (PR) represented by (40) can be equivalently studied using:

$$f = \mathbb{H}_d^\dagger \left(\tilde{\Phi}(\Phi^\top \mathbb{H}_d(f)\Psi)\tilde{\Psi}^\top\right) \ . \tag{44}$$

Similarly, for a given matrix input $Z \in \mathbb{R}^{n\times p}$, the perfect reconstruction condition for a matrix input Z can be given by

$$Z = \mathbb{H}_{d|p}^\dagger \left(\tilde{\Phi}(\Phi^\top \mathbb{H}_{d|p}(Z)\Psi)\tilde{\Psi}^\top\right) \ . \tag{45}$$

which is explicitly represented in the following proposition:

PROPOSITION 4. *Let $\Phi, \tilde{\Phi} \in \mathbb{R}^{n\times m}$ denote the non-local basis and its dual, and $\Psi, \tilde{\Psi} \in \mathbb{R}^{pd\times q}$ denote the local basis and its dual, respectively, which satisfy the frame condition:*

$$\tilde{\Phi}\Phi^\top = \sum_{i=1}^{m} \tilde{\phi_i}\phi_i^\top = I_{n\times n}, \tag{46}$$

$$\Psi\tilde{\Psi}^\top = \sum_{j=1}^{q} \psi_j\tilde{\psi_j}^\top = I_{pd\times pd} \ . \tag{47}$$

Suppose, furthermore, that the local bases matrix have block structure:

$$\Psi^\top = \begin{bmatrix} \Psi_1^\top & \cdots & \Psi_p^\top \end{bmatrix}, \quad \tilde{\Psi}^\top = \begin{bmatrix} \tilde{\Psi}_1^\top & \cdots & \tilde{\Psi}_p^\top \end{bmatrix} \tag{48}$$

with $\Psi_i, \tilde{\Psi}_i \in \mathbb{R}^{d\times q}$, whose j-th column is represented by ψ_j^i and $\tilde{\psi}_j^i$, respectively. Then, for any matrix $Z = [z_1 \cdots z_p] \in \mathbb{R}^{n\times p}$, we have

$$Z = \frac{1}{d}\sum_{i=1}^{m}\sum_{j=1}^{q}\sum_{k=1}^{p}\left[\langle z_k, \phi_i \circledast \psi_j^k\rangle \tilde{\phi}_i \circledast \tilde{\psi}_j^1 \quad \cdots \quad \langle z_k, \phi_i \circledast \psi_j^k\rangle \tilde{\phi}_i \circledast \tilde{\psi}_j^p\right] \tag{49}$$

or equivalently,

$$Z = \frac{1}{d}\left[\sum_{j=1}^{q}\left(\tilde{\Phi}c_j\right) \circledast \tilde{\psi}_j^1 \quad \cdots \quad \sum_{j=1}^{q}\left(\tilde{\Phi}c_j\right) \circledast \tilde{\psi}_j^p\right] \tag{50}$$

where c_j is the j-th column of the framelet coefficient matrix

$$\begin{aligned} C &= \Phi^\top\left(Z \circledast \overline{\Psi}\right) \\ &= \sum_{k=1}^{p}\begin{bmatrix} \langle z_k, \phi_1 \circledast \psi_1^k\rangle & \cdots & \langle z_k, \phi_1 \circledast \psi_q^k\rangle \\ \vdots & \ddots & \vdots \\ \langle z_k, \phi_m \circledast \psi_1^k\rangle & \cdots & \langle z_k, \phi_m \circledast \psi_q^k\rangle \end{bmatrix} \in \mathbb{R}^{m\times q} \quad . \end{aligned} \tag{51}$$

Proof. For a given $Z \in \mathbb{R}^{n\times p}$, using the frame condition (38) and (39), we have

$$\mathbb{H}_{d|p}(Z) = \tilde{\Phi}\Phi^\top \mathbb{H}_{d|p}(Z)\Psi\tilde{\Psi}^\top = \tilde{\Phi}C\tilde{\Psi}^\top \ .$$

where $C \in \mathbb{R}^{m\times q}$ denotes the framelet coefficient matrix computed by

$$C = \Phi^\top \mathbb{H}_{d|p}(Z)\Psi = \Phi^\top\left(Z \circledast \overline{\Psi}\right)$$

and its (i,j)-th element is given by

$$c_{ij} = \phi_i^\top \mathbb{H}_{d|p}(Z)\psi_j = \sum_{k=1}^{p}\langle z_k, \phi_i \circledast \psi_j^k\rangle$$

Furthermore, using (A.6), (A.7) and (A.8), we have

$$\begin{aligned} Z = \mathbb{H}_{d|p}^\dagger\left(\mathbb{H}_{d|p}(Z)\right) &= \mathbb{H}_{d|p}^\dagger\left(\tilde{\Phi}C\tilde{\Psi}^\top\right) \\ &= \left[\mathbb{H}_d^\dagger\left(\tilde{\Phi}C\tilde{\Psi}_1^\top\right) \quad \cdots \quad \mathbb{H}_d^\dagger\left(\tilde{\Phi}C\tilde{\Psi}_p^\top\right)\right] \\ &= \frac{1}{d}\left[\sum_{j=1}^{q}\left(\tilde{\Phi}c_j\right) \circledast \tilde{\psi}_j^1 \quad \cdots \quad \sum_{j=1}^{q}\left(\tilde{\Phi}c_j\right) \circledast \tilde{\psi}_j^p\right] \\ &= \frac{1}{d}\sum_{i=1}^{m}\sum_{j=1}^{q}\sum_{k=1}^{p}\left[\langle z_k, \phi_i \circledast \psi_j^k\rangle \tilde{\phi}_i \circledast \tilde{\psi}_j^1 \quad \cdots \quad \langle z_k, \phi_i \circledast \psi_j^k\rangle \tilde{\phi}_i \circledast \tilde{\psi}_j^p\right] \end{aligned}$$

This concludes the proof. ∎

REMARK 1. *Compared to Proposition 2, Propositions 3 and 4 are more general, since they consider the redundant and non-orthonormal non-local and local bases by allowing relaxed conditions, i.e. $m \geq n$ or $q \geq d$. The specific reason for $q \geq d$ is to investigate existing CNNs that have large number of filter channels at lower layers. The redundant global basis with $m \geq n$ is also believed to be useful for future research, so Proposition 3 is derived by considering further extension. However, since most of the existing deep networks use the condition $m = n$, we will mainly focus on this special case for the rest of the paper.*

REMARK 2. *For the given SVD in (33), the frame conditions (38) and (39) can be further relaxed to the following conditions:*

$$\tilde{\Phi}\Phi^\top = P_{R(U)}, \quad \Psi\tilde{\Psi}^\top = P_{R(V)}$$

due to the following matrix identity:

$$\mathbb{H}_d(f) = P_{R(U)}\mathbb{H}_d(f)P_{R(V)} = \tilde{\Phi}\left(\Phi^\top \mathbb{H}_d(f)\Psi\right)\tilde{\Psi}^\top.$$

In these case, the number of bases for non-local and local basis matrix can be smaller than that of Proposition 3 and Proposition 4, i.e. $m = r < n$ and $q = r < d$. Therefore, smaller number of bases still suffices for PR.

Finally, using Propositions 3 and 4 we will show that the convolution framelet expansion can be realized by two matched convolution layers, which has striking similarity to neural networks with encoder-decoder structure [54]. Our main contribution is summarized in the following Theorem.

THEOREM 5 (**Deep Convolutional Framelets Expansion**). *Under the assumptions of Proposition 4, we have the following decomposition of input $Z \in \mathbb{R}^{n\times p}$:*

$$Z = \left(\tilde{\Phi}C\right) \circledast \nu(\tilde{\Psi}) \tag{52}$$

$$C = \Phi^\top \left(Z \circledast \overline{\Psi}\right) \ , \tag{53}$$

where the decoder-layer convolutional filter $\nu(\tilde{\Psi})$ is defined by

$$\nu(\tilde{\Psi}) := \frac{1}{d}\begin{bmatrix} \tilde{\psi}_1^1 & \cdots & \tilde{\psi}_1^p \\ \vdots & \ddots & \vdots \\ \tilde{\psi}_q^1 & \cdots & \tilde{\psi}_q^p \end{bmatrix} \in \mathbb{R}^{dq\times p} \tag{54}$$

Similarly, under the assumptions of Proposition 3, we have the following decomposition of $f \in \mathbb{R}^n$:

$$f = \left(\tilde{\Phi}C\right) \circledast \nu(\tilde{\Psi}) \tag{55}$$

$$C = \Phi^\top \left(f \circledast \overline{\Psi}\right). \tag{56}$$

where

$$\nu(\tilde{\Psi}) := \frac{1}{d}\begin{bmatrix} \tilde{\psi}_1 \\ \vdots \\ \tilde{\psi}_q \end{bmatrix} \in \mathbb{R}^{dq} \tag{57}$$

Proof. First, note that (50) corresponds to a decoder layer convolution:

$$\begin{aligned} Z &= \frac{1}{d}\begin{bmatrix} \sum_{j=1}^q \left(\tilde{\Phi}c_j\right) \circledast \tilde{\psi}_j^1 & \cdots & \sum_{j=1}^q \left(\tilde{\Phi}c_j\right) \circledast \tilde{\psi}_j^p \end{bmatrix} \\ &= \left(\tilde{\Phi}C\right) \circledast \nu(\tilde{\Psi}) \end{aligned}$$

where $\nu(\tilde{\Psi})$ is defined by (54) and the last equality comes from the definition of MIMO convolution in (5) and (7). On the other hand, from (51), we have

$$C = \Phi^\top \left(Z \circledast \overline{\Psi}\right).$$

Similarly, using the defintion of the MISO convolution (11), Eq. (41) can be represented by

$$f = \left(\tilde{\Phi}C\right) \circledast \nu(\tilde{\Psi})$$

where $\nu(\tilde{\Psi})$ is defined by (57). Finally, (56) comes from (42). This concludes the proof. ∎

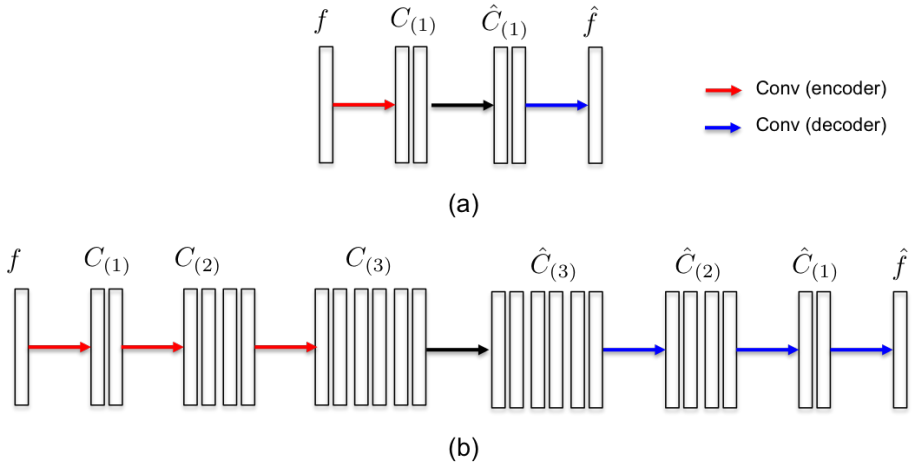


FIG. 5. *(a) One layer encoder-decoder, and (b) multi-layer encoder-decoder architectures.*

REMARK 3 (**Non-local basis as a generalized pooling/unpooling**). *Note that there exists a major difference in the encoder and decoder layer convolutions. Aside from the difference in the specific convolutional filters, the non-local basis matrix $\Phi^\top$ should be applied later to the filtered signal in the case of encoder (53), whereas the non-local basis matrix $\tilde{\Phi}$ should be multiplied first before the local filtering is applied in the decoder layer. This is in fact similar to the pooling and unpooling operations because the pooling is performed after filtering while unpooling is applied before filtering. Hence, we can see that the non-local basis is a generalization of the pooling/unpooling operations.*

Existing CNNs often incorporate the bias estimation for each layer of convolution. Accordingly, we are interested in extending our deep convolutional framelet expansion under bias estimation. Specifically, with the bias estimation, the encoder and decoder convolutions should be modified as:

$$C = \Phi^\top (Z \circledast \overline{\Psi} + 1_n b_{enc}^\top) \tag{58}$$

$$\hat{Z} = \left(\tilde{\Phi} C\right) \circledast \nu(\tilde{\Psi}) + 1_n b_{dec}^\top \tag{59}$$

where $1_n \in \mathbb{R}^n$ denotes the vector with 1, and $b_{enc} \in \mathbb{R}^q$ and $b_{dec} \in \mathbb{R}^p$ denote the encoder and decoder layer biases, respectively. Then, the following theorem shows that there exists a unique bias vector $b_{dec} \in \mathbb{R}^p$ for a given encoder bias vector $b_{enc} \in \mathbb{R}^q$ that satisfies the PR:

THEOREM 6 (**Matched Bias**). *Suppose that $\Phi, \tilde{\Phi} \in \mathbb{R}^{n\times m}$ and $\Psi, \tilde{\Psi} \in \mathbb{R}^{pd\times q}$ satisfies the assumptions of Proposition 4. Then, for a given bias $b_{enc} \in \mathbb{R}^q$ at the encoder layer, (58) and (59) satisfy the PR if the decoder bias is given by*

$$1_n b_{dec}^\top = -\mathbb{H}_{d|p}^\dagger \left(1_n b_{enc}^\top \tilde{\Psi}^\top\right), \tag{60}$$

or equivalently

$$b_{dec}[i] = -1_d^\top \tilde{\Psi}_i b_{enc}, \quad i = 1, \cdots, p. \tag{61}$$

Proof. See Appendix B. ∎

The simple convolutional framelet expansion using (56)(55) and (53)(52) (or (58) and (59) when including bias) is so powerful that a CNN with the encoder-decoder architecture emerges from them by inserting the encoder-decoder pair (56) and (55) between the encoder-decoder pair (53) and (52) as illustrated by the red and blue lines, respectively, in Fig. 5(a)(b). In general, the L-layer implementation of the convolutional framelets can be recursively defined. For example, the first layer

encoder-decoder architecture without considering bias is given by

$$\begin{aligned} f &= \mathbb{H}^{\dagger}_{d_{(1)}|p_{(1)}}\left(\tilde{\Phi}^{(1)}\hat{C}^{(1)}\tilde{\Psi}^{(1)\top}\right) \\ &= \left(\tilde{\Phi}^{(1)}\hat{C}^{(1)}\right) \circledast \nu(\tilde{\Psi}^{(1)}) \end{aligned}$$

where the decoder part of framelets coefficient at the i-th layer, $\hat{C}^{(i)} \in \mathbb{R}^{n\times q_{(i)}}$, $q_{(i)} \geq d_{(i)}p_{(i)}$, is given by

$$\hat{C}^{(i)} = \begin{cases} \mathbb{H}^{\dagger}_{d_{(i+1)}|p_{(i+1)}}\left(\tilde{\Phi}^{(i+1)}\hat{C}^{(i+1)}\tilde{\Psi}^{(i+1)}\right) = \left(\tilde{\Phi}^{(i+1)}\hat{C}^{(i+1)}\right) \circledast \nu(\tilde{\Psi}^{(i+1)}), & 1 \leq i < L \\ C^{(L)}, & i = L \end{cases} \tag{62}$$

whereas the encoder part framelet coefficients $C^{(i)} \in \mathbb{R}^{n\times q_{(i)}}$ are given by

$$C^{(i)} = \begin{cases} \Phi^{(i)\top}\mathbb{H}_{d_{(i)}|p_{(i)}}(C^{(i-1)})\Psi^{(i)} = \Phi^{(i)\top}\left(C^{(i-1)} \circledast \overline{\Psi}^{(i)}\right), & 1 \leq i \leq L \\ f, & i = 0 \end{cases} \tag{63}$$

Here, $d_{(i)}$ and $p_{(i)}$ denotes the filter length and the number of input channels at the i-th layer, respectively, and $q_{(i)}$ refers to the number of output channels. The specific number of channels will be analyzed in the following section.

3.2. Properties of Deep Convolutional Framelets. In this section, several important properties of deep convolutional framelets are explained in detail. First, the perfect reconstruction (PR) conditions in (56)(55) and (53)(52) can be also analyzed in the Fourier domain as shown in the following Proposition:

PROPOSITION 7 (**Fourier Analysis of Filter Channels**). *Suppose that Φ and $\tilde{\Phi}$ satisfy the frame condition (38). Then, the PR condition given by (53) and (52) with $\Psi^{\top} = \begin{bmatrix}\Psi_1^{\top} & \cdots & \Psi_p^{\top}\end{bmatrix}$ and $\tilde{\Psi}^{\top} = \begin{bmatrix}\tilde{\Psi}_1^{\top} & \cdots & \tilde{\Psi}_p^{\top}\end{bmatrix}$ can be represented by*

$$I_{p\times p} = \frac{1}{d}\begin{bmatrix} \widehat{\psi_1^1}^* & \cdots & \widehat{\psi_q^1}^* \\ \vdots & \ddots & \vdots \\ \widehat{\psi_1^p}^* & \cdots & \widehat{\psi_q^p}^* \end{bmatrix}\begin{bmatrix} \widehat{\tilde{\psi}_1^1} & \cdots & \widehat{\tilde{\psi}_1^p} \\ \vdots & \ddots & \vdots \\ \widehat{\tilde{\psi}_q^1} & \cdots & \widehat{\tilde{\psi}_q^p} \end{bmatrix} \tag{64}$$

where $\widehat{\psi}$ denotes the Fourier transform of ψ, and the superscript * is the complex conjugate. In particular, the PR condition given by (56) and (55) can be represented by

$$\frac{1}{d}\sum_{i=1}^{q} \widehat{\psi_i}^* \widehat{\tilde{\psi}_i} = 1. \tag{65}$$

Furthermore, if the local basis Ψ is orthormal, then we have

$$\frac{1}{d}\sum_{i=1}^{d} |\widehat{\psi_i}|^2 = 1. \tag{66}$$

Proof. See Appendix C. ∎

REMARK 4. *Note that (66) and (65) are equivalent to the perfect reconstruction conditions for the orthogonal and biorthogonal wavelet decompositions, respectively [50, 17]. However, without the frame condition (38) for the non-local bases, such simplification is not true. This is another reason why we are interested in imposing the frame condition (38) for the non-local bases in order to use the connection to the classical wavelet theory [50].*

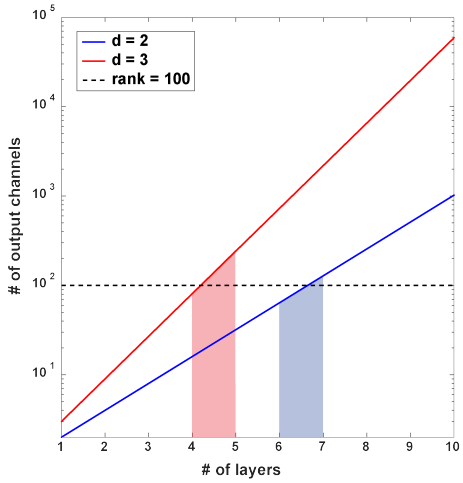


FIG. 6. *The exponential increase in the number of output channels. Note that the y-axis is in the log-scale.*

The following proposition shows that a sufficient condition for fulfilling PR is that the number of input channels should increase multiplicatively along the layers:

PROPOSITION 8 (**Number of Filter Channels**). *A sufficient condition to achieve PR is that the number of output channel* $q_{(l)}, l = 1, \cdots, L$ *satisfies*

$$q_{(l)} \geq q_{(l-1)} d_{(l)}, \quad l = 1, \cdots, L, \tag{67}$$

where $d_{(i)}$ *is the filter length at the* i*-th layer and* $q_{(0)} = 1$.

Proof. See Appendix D. ∎

An intuitive explanation of Proposition 8 is that the cascaded application of two multi-channel filter banks is equivalent to applying a combined filter bank generated by each combination of two filters in each stage, so the output dimension of the filter bank increases multiplicatively. As a special case of Proposition 8, we can derive the following sufficient condition:

$$q_{(l)} = \prod_{i=1}^{l} d_{(i)}, \quad l = 1, \cdots, L \quad ,$$

which is obtained by choosing the minimum number of output channels at each layer. This implies that the number of channels increase exponentially with respect to layers as shown in Fig. 6, which is difficult to meet in practice due to the memory requirement. Then, a natural question is why we still prefer a deep network to a shallow one. Proposition 9 provides an answer to this question.

PROPOSITION 9 (**Rank Bound of Hankel Matrix**). *Suppose that* $\Phi^{(l)} = I_{n\times n}, \forall l \geq 1$. *Then, the rank of the extended Hankel matrix* $\mathbb{H}_{d_{(l)}|p_{(l)}}(C^{(l-1)})$ *in* (63) *is upper-bounded by*

$$\text{RANK}\mathbb{H}_{d_{(l)}|p_{(l)}}(C^{(l-1)}) \leq \min\{\text{RANK}\mathbb{H}_n(f), d_{(l)}p_{(l)}\} \tag{68}$$

Proof. See Appendix E. ∎

REMARK 5. *Proposition 9 is derived by assuming the identity matrix as non-local basis. While we expect similar results for general non-local basis that satisfies the frame condition* (38)*, the introduction of such non-local basis makes the analysis very complicated due to the non-commutative nature of matrix multiplication and convolution, so we defer its analysis for future study.*

We believe that Eq. (68) is the key inequality to reveal the role of the depth. Specifically, to exploit the low-rank structure of the input signal, the upper bound of (68) should be determined by

the intrinsic property of the signal, $r := \text{RANK}\mathbb{H}_n(f)$, instead of the number of columns of the Hankel matrix, $d_{(l)}p_{(l)}$, which can be chosen arbitrary. Thus, if $d_{(l)} = d, \forall l$, then Eqs.(68) and (68) inform that the number of encoder-decoder layer depth L is given by

$$r \leq d^L \Longleftrightarrow L \geq \log_d(r) \ . \tag{69}$$

This implies that the number of minimum encoder-decoder layer is dependent on the rank structure of the input signal and we need a deeper network for a more complicated signal, which is consistent with the empirical findings. Moreover, as shown in Fig. 6, for a given intrinsic rank, the depth of the network also depends on the filter length. For example, if the intrinsic rank of the Hankel matrix is 100, the network depth with respect to $d = 2$ is 7, whereas it is 5 when longer filter with $d = 3$ is used.

Suppose that there are not sufficient number of output channels at a specific layer, say $l = l^*$, and the signal content is approximated. Then, from the proof of Proposition 9 (in particular, (E.2)), we can easily see that $\text{RANK}\mathbb{H}_{d_{(l)}|p_{(l)}}(C^{(l-1)})$ is upper-bounded by the rank structure of the approximated signal at $l = l_*$. Moreover, if the numbers of channels are not sufficient for all layers, the rank will gradually decrease along the layers. This theoretical prediction will be confirmed later in Discussion using empirical data.

3.3. ReLU Nonlinearity. In order to reveal the link between the convolutional framelets and the deep network, we further need to consider a nonlinearity. Note that the ReLU nonlinearity [22, 31] is currently most widely used for deep learning approaches. Specifically, the ReLU $\rho(\cdot)$ is an element-wise operation for a matrix such that for a matrix $X = [x_{ij}]_{i,j=1}^{n,m} \in \mathbb{R}^{n\times m}$, the ReLU operator provides non-negative part, i.e. $\rho(X) = [\max(0, x_{ij})]_{i,j=1}^{n,m}$. By inserting ReLUs, the L- layer encoder-decoder architecture neural network with bias is defined (with a slight abuse of notation) by

$$\begin{aligned} \mathcal{Q}(f) &:= \mathcal{Q}\left(f; \{\Psi^{(j)}, \tilde{\Psi}^{(j)}, b_{enc}^{(j)}, b_{dec}^{(j)}\}_{j=1}^{L}\right) \\ &= \left(\tilde{\Phi}^{(1)}\rho(\hat{C}^{(1)})\right) \circledast \nu(\tilde{\Psi}^{(1)}) + 1_n b_{dec}^{(1)\top} \end{aligned} \tag{70}$$

where

$$\hat{C}^{(i)} = \begin{cases} \left(\tilde{\Phi}^{(i+1)}\rho(\hat{C}^{(i+1)})\right) \circledast \nu(\tilde{\Psi}^{(i+1)}) + 1_n b_{dec}^{(i+1)\top}, & 1 \leq i < L \\ \rho(C^{(L)}), & i = L \end{cases} \tag{71}$$

and

$$C^{(i)} = \begin{cases} \Phi^{(i)\top}\left(\rho(C^{(i-1)}) \circledast \overline{\Psi}^{(i)} + 1_n b_{enc}^{(i)\top}\right), & 1 \leq i \leq L \\ f, & i = 0 \end{cases} \tag{72}$$

Recall that the PR condition for the deep convolutional framelets was derived without assuming any nonlinearity. Thus, the introduction of ReLU appears counter-intuitive in the context of PR. Interestingly, in spite of ReLU nonlinearity, the following theorem shows that the PR condition can be satisfied when filter channels and bias having opposite phase are available.

PROPOSITION 10 (**PR under ReLU using Opposite Phase Filter Channels**). *Suppose that* $\tilde{\Phi}^{(l)}\Phi^{(l)\top} = I_{n\times n}$ *and* $\Psi^{(l)}, \tilde{\Psi}^{(l)} \in \mathbb{R}^{p_{(l)}d_{(l)}\times 2m_{(l)}}$ *with* $m_{(l)} \geq p_{(l)}d_{(l)}$ *for all* $l = 1, \cdots, L$. *Then, the neural network output in* (70) *satisfies the perfect reconstruction condition, i.e.* $f = \mathcal{Q}(f)$ *if the encoder-decoder filter channels are given by*

$$\Psi^{(l)} = \begin{bmatrix} \Psi_+^{(l)} & -\Psi_+^{(l)} \end{bmatrix}, \quad \tilde{\Psi}^{(l)} = \begin{bmatrix} \tilde{\Psi}_+^{(l)} & -\tilde{\Psi}_+^{(l)} \end{bmatrix} \tag{73}$$

satisfying the condition:

$$\Psi_+^{(l)}\tilde{\Psi}_+^{(l)\top} = I_{p_{(l)}d_{(l)}\times p_{(l)}d_{(l)}}, \qquad \Psi_+^{(l)}, \tilde{\Psi}_+^{(l)} \in \mathbb{R}^{p_{(l)}d_{(l)}\times m_{(l)}} \tag{74}$$

and the encoder-decoder bias pairs $b_{enc}^{(l)}, b_{dec}^{(l)}$ *are given by*

$$b_{enc}^{(l)} = \begin{bmatrix} b_{enc,+}^{(l)T} & -b_{enc,+}^{(l)T} \end{bmatrix}, \quad 1_n b_{dec}^{(l)\top} = -\mathbb{H}_{d|p}^{\dagger}\left(1_n b_{enc,+}^{(l)\top}\tilde{\Psi}^{(l)\top}\right) . \tag{75}$$

Proof. See Appendix F. ∎

REMARK 6. *Eq.* (73) *in Proposition 10 predicts the existence of filter pairs with opposite phase. Amazingly, this theoretical prediction coincides with the empirical observation in deep learning literature. For example, Shang et al [60] observed an intriguing property that the filters in the lower layers form pairs (i.e., filters with opposite phase). To exploit this property for further network performance improvement, the authors proposed so called concatenated ReLU (CReLU) network to explicitly retrieve the negative part of* $\Phi^\top F\Psi_+$ *using* $\rho\left(\Phi^\top F(-\Psi_+)\right)$ *[60].*

REMARK 7. *Note that there are infinite number of filters satisfying* (73)*. In fact, the most important requirement for PR is the* existence *of opposite phase filters as in* (73) *satisfying the frame condition* (74) *rather than the specific filter coefficients. This may suggest the excellent generalization performance of a deep network even from small set of training data set.*

Proposition 10 deals with the PR condition using redundant local filters $\Psi \in \mathbb{R}^{pd\times 2m}$ with $m \geq pd$. This can be easily satisfied at the lower layers of the deep convolutional framelets; however, the number of filter channels for PR grows exponentially according to layers as shown in (67). Thus, at higher layers of deep convolutional framelets, the condition $m \geq pd$ for Proposition 10 may not be satisfied. However, even in this case, we can still achieve PR as long as the extended Hankel matrix at that layer is sufficiently low-ranked.

PROPOSITION 11 (**Low-Rank Approximation with Insufficient Filter Channels**). *For a given input* $X \in \mathbb{R}^{n\times p}$*, let* $\mathbb{H}_{d|p}(X)$ *denotes its extended Hankel matrix whose rank is* r*. Suppose, furthermore, that* $\tilde{\Phi}\Phi^\top = I_{n\times n}$*. Then, there exists* $\Psi \in \mathbb{R}^{pd\times 2m}$ *and* $\tilde{\Psi} \in \mathbb{R}^{pd\times 2m}$ *with* $r \leq m < pd$ *such that*

$$X = \mathbb{H}_{d|p}^{\dagger}(\Phi\rho\left(\Phi^\top \mathbb{H}_{d|p}(X)\Psi\right)\tilde{\Psi}^\top).$$

Proof. See Appendix G. ∎

However, as the network gets deeper, more layers cannot satisfy the condition for Proposition 11. To address this, the residual net [32] is useful. Recall that the residual net (ResNet) has been widely used for image classification as well as image reconstruction. More specifically, the residual net architecture shown in Fig. 7(a) can be represented by

$$\hat{X} = R(F;\Psi,\tilde{\Psi}) := \rho\left(F - \rho(F\Psi)\tilde{\Psi}^\top\right) \tag{76}$$

where $F := \mathbb{H}_{d|p}(X)$. The following result shows that the residual network truncates the least significant subspaces:

PROPOSITION 12 (**High-rank Approximation using Residual Nets**). *For a given nonnegative input* $X \in \mathbb{R}^{n\times p}$*, let* $\mathbb{H}_{d|p}(X)$ *denotes its extended Hankel matrix and its SVD is given by*

$$\mathbb{H}_{d|p}(X) = U\Sigma V^\top = \sum_{i=1}^{r} \sigma_i u_i v_i^\top, \tag{77}$$

where u_i *and* v_i *denotes the left and right singular vectors, and* $\sigma_1 \geq \sigma_2 \geq \cdots \geq \sigma_r > 0$ *are the singular values and* r *denotes the rank. Then, there exists* $\Psi \in \mathbb{R}^{pd\times 2m}$ *and* $\tilde{\Psi} \in \mathbb{R}^{pd\times 2m}$ *with* $r < pd$ *such that*

$$X = \mathbb{H}_{d|p}^{\dagger}(R(F;\Phi,\Psi,\tilde{\Psi})), \tag{78}$$

where $R(F;\Psi,\tilde{\Psi})$ *is given by* (76)*.*

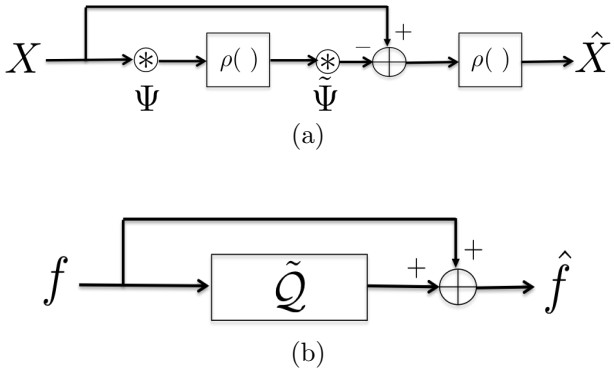


FIG. 7. *Block diagram of (a) a residual block and (b) skipped connection.*

Proof. See Appendix H. ∎

Note that the PR condition for the residual network is much more relaxed than that of Proposition 11, since we do not have any constraint on m that determines the output filter channels number. Specifically, for the case of Proposition 11, the number of output channel filters should be $q = 2m \geq 2r$. On the other hand, the PR condition for residual net only requires the existence of the null space in the extended Hankel matrix (i.e. $r < pd$), and it does not depend on the number of output channels. Therefore, we have more freedom to choose filters.

In addition, Proposition 11 also implies the low rank approximation, if the number of output channels is not sufficient. Specifically, with matched opposite phase filters, we have

$$\Phi\rho\left(\Phi^\top \mathbb{H}_{d|p}(X)\Psi\right)\tilde{\Psi}^\top) = \mathbb{H}_{d|p}(X)\Psi_+\tilde{\Psi}_+^\top \,. \tag{79}$$

Thus, we can choose $\Psi_+, \tilde{\Psi}_+$ such that (79) results in the rank-m approximation of $\mathbb{H}_{d|p}(X)$. On the other hand, from the proof in Appendix H, we can see that

$$R(F;\Phi,\Psi_+,\tilde{\Psi}_+) = \rho\left(\mathbb{H}_{d|p}(X) - U\Sigma V^\top \Psi_+\tilde{\Psi}_+^\top\right) \tag{80}$$

Accordingly, by choosing $\Psi_+, \tilde{\Psi}_+$ such that $\Psi_+\tilde{\Psi}_+^\top = P_{R(v_{pd})}$ where v_{pd} is the singular vector for the least singular value, we can minimize the error of approximating $\mathbb{H}_{d|p}(X)$ using $R(F;\Psi_+,\tilde{\Psi}_+)$. This is why we refer Proposition 12 to as the high rank approximation using residual net.

3.4. Role of perfect reconstruction condition and shrinkage behaviour of network. So far, we have investigated the perfect recovery (PR) condition for deep convolutional framelets. Here, we are now ready to explain why the PR is useful for inverse problems.

Suppose that an analysis operator $\mathcal{W}$, which are composed of frame bases, and the associated synthesis operator $\tilde{\mathcal{W}}^\top$ satisfy the following frame condition:

$$f = \tilde{\mathcal{W}}^\top \mathcal{W} f, \quad \forall f \in H \tag{81}$$

where H denotes the Hilbert space of our interest. Signal processing using frame basis satisfying (81) has been extensively studied for frame-based image processing [50, 11, 10]. One of the important advantages of these frame-based algorithm is the proven convergence [11, 10], which makes the algorithm powerful.

For example, consider a signal denosing algorithm to recover noiseless signal f^* from the noisy measurement $g = f^* + e$, where e is the additive noise. Then, a frame-based denoising algorithm [18, 13, 12] recovers the unknown signal by substituting g for f in the right side of (81) and applies a shrinkage operator S_τ to the framelet coefficients to eliminate the small magnitude noise signals:

$$\hat{f} = \tilde{\mathcal{W}}^\top \mathcal{S}_\tau(\mathcal{W} g) \tag{82}$$

where τ denotes a shrinkage parameter. In denoising, soft- or hard- thresholding shrinkage operations are most widely used. Thus, to make the frame-based denoising algorithm successful, the frame should be energy compacting so that most of the signals are concentrated in a small number of framelet coefficients, whereas the noises are spread out across all framelet coefficients.

As an another example, consider a signal inpainting problem [11, 10], where for a given signal $f \in H$, we measure g only on the index set Λ and our goal is then to estimate the unknown image f on the complementary index set Λ^c. Let P_Λ be the diagonal matrix with diagonal entries 1 for the indices in Λ and 0 otherwise. Then, we have the following identities:

$$\begin{aligned} f &= \mu P_\Lambda f + (I - \mu P_\Lambda) f \\ &= \mu P_\Lambda g + (I - \mu P_\Lambda) \tilde{\mathcal{W}}^\top \mathcal{W} f \end{aligned} \tag{83}$$

where we use the frame condition (81) for the last equality. A straight-forward frame-based inpainting algorithms [11, 10] can be then obtained from (83) as:

$$f_{n+1} = \mu P_\Lambda g + (I - \mu P_\Lambda) \mathcal{W}^\top \mathcal{S}_\tau \left(\mathcal{W} f_n \right) \ , \tag{84}$$

where $\mathcal{S}_\tau$ denotes a shrinkage operator with the parameter τ and f_0 is initialized to $P_\Lambda g$.

Now, note that the computation of our deep convolutional framelet coefficients can represent an analysis operator:

$$\mathcal{W} f := C = \Phi^\top (f \circledast \overline{\Psi})$$

whereas the synthesis operator is given by the decoder part of convolution:

$$\tilde{\mathcal{W}}^\top C := (\Phi C) \circledast \nu(\tilde{\Psi}).$$

If the non-local and local basis satisfy the frame condition (38) and (39) for all layers, they satisfy the PR condition (81). Thus, we could use (82) and (84) for denoising and inpainting applications. Then, what is the shrinkage operator in our deep convolutional framelets?

Although one could still use similar soft- or hard- thresholding operator, one of the unique aspects of deep convolutional framelets is that the number of filter channels can control the shrinkage behaviour. Moreover, the optimal local basis are learnt from the training data such that they give the best shrinkage behavior. More specifically, the low-rank shrinkage behaviour emerges when the number of output filter channels are not sufficient. These results are very useful in practice, since the low-rank approximation of Hankel matrix is good for reducing the noises and artifacts as demonstrated in image denoising [38], artifact removal [36] and deconvolution [53].

To understand this claim, consider the following regression problem under the Hankel structured low-rank constraint:

$$\begin{aligned} \min_{f \in \mathbb{R}^n} \quad & \|f^* - f\|^2 \\ \text{subject to} \quad & \text{RANK} \mathbb{H}_d(f) \leq r < d. \end{aligned} \tag{85}$$

where $f^* \in \mathbb{R}^d$ denotes the ground-truth signal and we are interested in finding rank-r approximation. Then, for any feasible solution f for (85), its Hankel structured matrix $\mathbb{H}_d(f)$ has the singular value decomposition $\mathbb{H}_d(f) = U \Sigma V^\top$ where $U = [u_1 \cdots u_r] \in \mathbb{R}^{n \times r}$ and $V = [v_1 \cdots v_r] \in \mathbb{R}^{d \times r}$ denote the left and the right singular vector bases matrices, respectively; $\Sigma = (\sigma_{ij}) \in \mathbb{R}^{r \times r}$ is the diagonal matrix with singular values. Then, we can find two matrices pairs $\Phi, \tilde{\Phi} \in \mathbb{R}^{n \times n}$ and Ψ, $\tilde{\Psi} \in \mathbb{R}^{d \times r}$ satisfying the conditions

$$\tilde{\Phi} \Phi^\top = I_{n \times n}, \qquad \Psi \tilde{\Psi}^\top = P_{R(V)}, \tag{86}$$

such that

$$\mathbb{H}_d(f) = \tilde{\Phi} \Phi^\top \mathbb{H}_d(f) \Psi \tilde{\Psi}^\top,$$

which leads to the decomposition of f using a single layer deep convolutional framelet expansion:

$$f = \left(\tilde{\Phi} C\right) \circledast \nu(\tilde{\Psi}), \quad \text{where} \quad C = \Phi^\top \left(f \circledast \overline{\Psi}\right) \tag{87}$$

Note that (87) is the general form of the signals that are associated with a rank-r Hankel structured matrix.

Note that the basis $(\Phi, \tilde{\Phi})$ and $(\Psi, \tilde{\Psi})$ are not specified in (89). In our deep convolutional framelets, Φ and $\tilde{\Phi}$ correspond to the generalized pooling and unpooling which are chosen based on domain knowledges, so we are interested in only estimating the filters Ψ, $\tilde{\Psi}$. To restrict the search space furthermore, let $\mathcal{H}_r$ denote the space of such signals that have positive framelet coefficient, i.e. $C \geq 0$:

$$\mathcal{H}_r = \left\{ f \in \mathbb{R}^n \mid f = \left(\tilde{\Phi} C\right) \circledast \nu(\tilde{\Psi}) + 1_n b_{dec}, \quad C = \Phi^\top \left(f \circledast \overline{\Psi} + 1_n b_{enc}^\top\right) \geq 0 \right\} \tag{88}$$

where $b_{enc} \in \mathbb{R}^d, b_{dec} \in \mathbb{R}$ denotes the encoder and decoder biases, respectively. Then, the main goal of the neural network training is to learn $(\Psi, \tilde{\Psi}, b_{enc}, b_{dec})$ from training data $\{(f_{(i)}, f^*_{(i)})\}_{i=1}^N$ assuming that $\{f^*_{(i)}\}$ are associated with rank-r Hankel matrices. More specifically, our regression problem under low-rank Hankel matrix constraint in (85) for the training data can be equivalently represented by

$$\min_{\{f_{(i)}\} \in \mathcal{H}_r} \sum_{i=1}^N \|f^*_{(i)} - f_{(i)}\|^2 = \min_{(\Psi, \tilde{\Psi}, b_{enc}, b_{dec})} \sum_{i=1}^N \left\| f^*_{(i)} - \mathcal{Q}(f_{(i)}; \Psi, \tilde{\Psi}, b_{enc}, b_{dec}) \right\|^2 \tag{89}$$

where

$$\mathcal{Q}(f_{(i)}; \Psi, \tilde{\Psi}, b_{enc}, b_{dec}) = \left(\tilde{\Phi} C[f_{(i)}]\right) \circledast \nu(\tilde{\Psi}) + 1_n b_{dec}$$

$$C[f_{(i)}] = \rho\left(\Phi^\top \left(f_{(i)} \circledast \overline{\Psi} + 1_n b_{enc}^\top\right)\right),$$

where $\rho(\cdot)$ is the ReLU to impose the positivity. After the network is fully trained, the inference for a given noisy input f is simply done by $\mathcal{Q}(f; \Psi, \tilde{\Psi}, b_{enc}, b_{dec})$, which is equivalent to find a denoised solution that has the rank-r Hankel structured matrix. Therefore, using deep convolutional framelets with insufficient channels, we do not need an explicit shrinkage operation. The idea can be further extended to the multi-layer deep convolutional framelet expansion as follows:

DEFINITION 13 (**Deep Convolutional Framelets Training**). *Let $\{f_{(i)}, f^*_{(i)}\}_{i=1}^N$ denote the input and target sample pairs. Then, the deep convolutional framelets training problem is given by*

$$\min_{\{\Psi^{(j)}, \tilde{\Psi}^{(j)}, b^{(j)}_{enc}, b^{(j)}_{(dec)}\}_{j=1}^L} \sum_{i=1}^N \left\| f^*_{(i)} - \mathcal{Q}\left(f_{(i)}; \{\Psi^{(j)}, \tilde{\Psi}^{(j)}, b^{(j)}_{enc}, b^{(j)}_{(dec)}\}_{j=1}^L\right) \right\|^2 \tag{90}$$

where $\mathcal{Q}$ is defined by (70).

Thanks to the inherent shrinkage behaviour from the neural network training, (82) and (84) can be written as:

$$\hat{f} = \mathcal{Q}(g) \tag{91}$$

$$f_{n+1} = \mu P_\Lambda g + (I - \mu P_\Lambda) \mathcal{Q}(f_n) \tag{92}$$

where $\mathcal{Q}(\cdot)$ denotes the deep convolutional framelet output. Note that (91) is in fact the existing deep learning denoising algorithm [70, 9, 4], whereas the first iteration of (92) corresponds to the existing deep learning-based inpainting algorithm [70, 73]. This again confirms that deep convolutional framelets is a general deep learning framework. Later, we will provide numerical experiments using (91) and (92) for image denosing and inpainting applications, respectively.

3.5. Bypass-Connection versus No Bypass-Connection. The by-pass connection in Fig. 7(b) is closely related to ResNet in Fig. 7(a), except that the final level of nonlinearity is not commonly used in by-pass connection and the by-pass connection is normally placed between the input and the output of the network. In practice, researchers empirically determine whether to use bypass connections or not by trial and error.

In order to understand the role of the by-pass connection, we need to revisit the single layer training procedure in (89). Then, the network with the bypass connection can be written by

$$\mathcal{Q}(f_{(i)};\Psi,\tilde{\Psi},b_{enc},b_{dec}) = \tilde{\mathcal{Q}}(f_{(i)};\Psi,\tilde{\Psi},b_{enc},b_{dec}) + f_{(i)},$$

where

$$\tilde{\mathcal{Q}}(f_{(i)};\Psi,\tilde{\Psi},b_{enc},b_{dec}) = \left(\tilde{\Phi}C[f_{(i)}]\right) \circledast \nu(\tilde{\Psi}) + 1_n b_{dec},$$
$$C[f_{(i)}] = \Phi^\top \left(f_{(i)} \circledast \overline{\Psi} + 1_n b_{enc}^\top\right).$$

Next, note that $f_{(i)}$ is contaminated with artifacts so that it can be written by

$$f_{(i)} = f^*_{(i)} + h_{(i)},$$

where $h_{(i)}$ denotes the noise components and $f^*_{(i)}$ refers to the noise-free ground-truth. Therefore, the network training (89) using the by-pass connection can be equivalently written by

$$\min_{(\Psi,\tilde{\Psi},b_{enc},b_{dec})} \sum_{i=1}^N \left\| h_{(i)} + \tilde{\mathcal{Q}}(f^*_{(i)} + h_{(i)};\Psi,\tilde{\Psi},b_{enc},b_{dec}) \right\|^2 \tag{93}$$

Therefore, if we can find an encoder filter $\overline{\Psi}$ such that it approximately annihilates the true signal $f^*_{(i)}$, i.e.

$$f^*_{(i)} \circledast \overline{\Psi} \simeq 0\ , \tag{94}$$

then we have

$$\begin{aligned} C[f^*_{(i)} + h_{(i)}] &= \Phi^\top \left((f^*_{(i)} + h_{(i)}) \circledast \overline{\Psi} + 1_n b_{enc}^\top\right) \\ &\simeq \Phi^\top \left(h_{(i)} \circledast \overline{\Psi} + 1_n b_{enc}^\top\right) \\ &= C[h_{(i)}] \end{aligned}$$

With this filter $\overline{\Psi}$, the decoder filter $\tilde{\Psi}$ can be designed such that

$$\begin{aligned} \left(\tilde{\Phi}C[h_{(i)}]\right) \circledast \nu(\tilde{\Psi}) &= \left(\tilde{\Phi}\Phi^\top \left((h_{(i)}) \circledast \overline{\Psi}\right)\right) \circledast \nu(\tilde{\Psi}) \\ &= h_{(i)} \circledast \overline{\Psi} \circledast \nu(\tilde{\Psi}) \\ &\simeq -h_{(i)}\ , \end{aligned}$$

by minimizing the cost (93). Thus, our deep convolutional framelet with a by-pass connection can recover the artifact signal $h_{(i)}$ (hence, it recovers $f^*_{(i)}$ by subtracting it from $f_{(i)}$). In fact, (94) is equivalent to the filter condition in (80) in ResNet which spans the minimum singular vector subspace.

Using the similar argument, we can see that if the encoder filter annihilates the artifacts, i.,e.

$$h_{(i)} \circledast \overline{\Psi} \simeq 0 \tag{95}$$

then $C[f^*_{(i)} + h_{(i)}] \simeq C[f^*_{(i)}]$ and our deep convolutional framelet *without* the by-connection can recover the ground-truth signal $f^*_{(i)}$ i.e. $\mathcal{Q}(f_{(i)};\Psi,\tilde{\Psi}) \simeq f^*_{(i)}$ by minimizing the cost (93).

In brief, if the true underlying signal has lower dimensional structure than the artifact, then the annihlating filter relationship in (94) is more easier to achieve [66]; thus, the neural network with by-pass connection achieves better performance. On the other hand, if the artifact has lower dimensional

structure, a neural network without by-pass connection is better. This coincides with many empirical findings. For example, in image denoising [40, 76] or streaking artifact problems [28, 35], a residual network works better, since the artifacts are random and have complicated distribution. In contrast, to remove the cupping artifacts in the X-ray interior tomography problem, a CNN without skipped connection is better, since the cupping artifacts are usually smoothly varying [27].

4. Multi-Resolution Analysis via Deep Convolutional Framelets. In deep convolutional framelets, for a given non-local basis, the local convolution filters are learnt to give the best shrinkage behaviour. Thus, non-local basis Φ is an important design parameter that controls the performance. In particular, the energy compaction property for the deep convolutional framelets is significantly affected by Φ. Recall that the SVD basis for the Hankel matrix results in the best energy compaction property; however, the SVD basis varies depending on input signal type so that we cannot use the same basis for various input data.

Therefore, we should choose an analytic non-local basis Φ such that it can approximate the SVD basis and result in good energy compaction property. Thus, wavelet is one of the preferable choices for piecewise continuous signals and images [17]. Specifically, in wavelet basis, the standard pooling and unpooling networks are used as low-frequency path of wavelet transform, but there exists additional high-frequency paths from wavelet transform. Another important motivation for multi-resolution analysis of convolutional framelets is the exponentially large receptive field. For example, Fig. 8 compares the network depth-wise effective receptive field of a multi-resolutional network with pooling against that of a baseline network without pooling layers. With the same size convolutional filters, the effective receptive field is enlarged in the network with pooling layers. Therefore, our multi-resolution analysis (MRA) is indeed derived to supplement the enlarged receptive field from pooling layers with the fine detailed processing using high-pass band convolutional framelets.

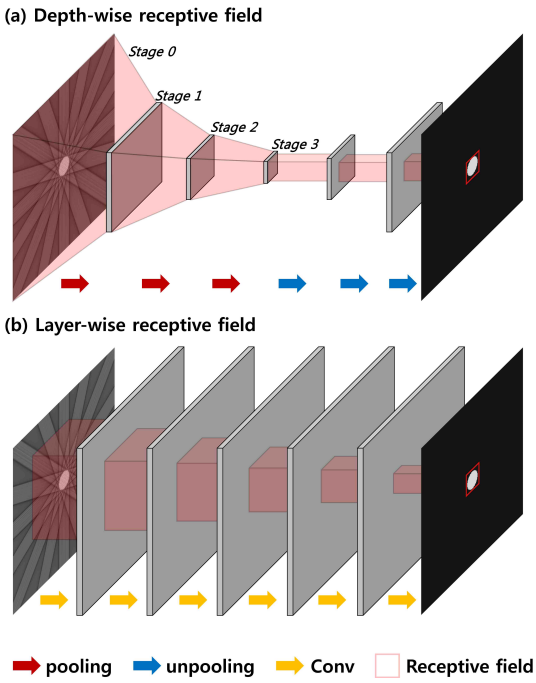


FIG. 8. *Effective receptive field comparison. (a) Multi-resolution network, and (b) CNN without pooling.*

4.1. Limitation of U-Net. Before we explain our multi-resolution deep convolutional framelets, we first discuss the limitations of the popular multi-resolution deep learning architecture called U-net [59], which is a composed of encoder and decoder network with a skipped connection. The U-Net utilizes the pooling and unpooling as shown in Fig. 10(a) to obtain the exponentially large receptive

field. Specifically, the average and max pooling operators $\Phi_{ave}, \Phi_{max} \in \mathbb{R}^{n\times\frac{n}{2}}$ for $f \in \mathbb{R}^n$ used in U-net is defined as follows:

$$\Phi_{ave} = \frac{1}{\sqrt{2}}\begin{bmatrix} 1 & 0 & \cdots & 0 \\ 1 & 0 & \cdots & 0 \\ 0 & 1 & \cdots & 0 \\ 0 & 1 & \cdots & 0 \\ \vdots & \vdots & \ddots & \vdots \\ 0 & 0 & \cdots & 1 \\ 0 & 0 & \vdots & 1 \end{bmatrix}, \Phi_{max} = \begin{bmatrix} b_1 & 0 & \cdots & 0 \\ 1-b_1 & 0 & \cdots & 0 \\ 0 & b_2 & \cdots & 0 \\ 0 & 1-b_2 & \cdots & 0 \\ \vdots & \vdots & \ddots & \vdots \\ 0 & 0 & \cdots & b_{\frac{n}{2}} \\ 0 & 0 & \vdots & 1-b_{\frac{n}{2}} \end{bmatrix} \tag{96}$$

where $\{b_i\}_i$ in max pooling are random $(0, 1)$ binary numbers that are determined by the signal statistics. We can easily see that the columns of max pooling or average pooling are orthogonal to each other; however, it does not constitute a basis because it does not span $\mathbb{R}^n$. Then, what does this network perform?

Recall that for the case of average pooling, the unpooling layer $\tilde{\Phi}$ has the same form as the pooling, i.e. $\tilde{\Phi} = \Phi$. In this case, under the frame condition for the local bases $\Psi\tilde{\Psi}^\top = I_{d\times d}$, the signal after pooling and unpooling becomes:

$$\hat{f} = \mathbb{H}_d^\dagger\left(\Phi(\Phi^\top\mathbb{H}_d(f)\right) = \Phi\Phi^\top f$$

which is basically a low-pass filtered signal and the detail signals are lost. To address this limitation and retain the fine detail, U-net has by-pass connections and concatenation layers as shown in Fig. 10(a). Specifically, combining the low-pass and by-pass connection, the augmented convolutional framelet coefficients C_{aug} can be represented by

$$C_{aug} = \Phi_{aug}^\top\mathbb{H}_d(f)\Psi = \Phi_{aug}^\top(f \circledast \overline{\Psi}) = \begin{bmatrix} C \\ S \end{bmatrix} \tag{97}$$

where

$$\Phi_{aug}^\top := \begin{bmatrix} I \\ \Phi^\top \end{bmatrix}, \quad C := f \circledast \Psi, \quad S := \Phi^\top(f \circledast \overline{\Psi}) \tag{98}$$

After unpooling, the low-pass branch signal becomes $\Phi S = \Phi\Phi^\top(f \circledast \overline{\Psi})$, so the signals at the concatenation layer is then given by

$$W = \begin{bmatrix} \mathbb{H}_d(f)\Psi & \Phi\Phi^\top\mathbb{H}_d(f)\Psi \end{bmatrix} = \begin{bmatrix} f \circledast \overline{\Psi} & \Phi\Phi^\top(f \circledast \overline{\Psi}) \end{bmatrix} \tag{99}$$

where the first element in W comes from the by-pass connection. The final step of recovery can be then represented by:

$$\begin{aligned} \hat{f} &= \mathbb{H}_d^\dagger\left(W\begin{bmatrix} \tilde{\Psi}_1^\top \\ \tilde{\Psi}_2^\top \end{bmatrix}\right) \\ &= \mathbb{H}_d^\dagger(\mathbb{H}_d(f)\Psi\tilde{\Psi}_1^\top) + \mathbb{H}_d^\dagger\left(\Phi\Phi^\top\mathbb{H}_d(f)\Psi\tilde{\Psi}_2^\top\right) \\ &= \frac{1}{d}\sum_{i=1}^{q}\left(f \circledast \overline{\psi}_i \circledast \tilde{\psi}_i^1 + \Phi\Phi^\top(f \circledast \overline{\psi}_i) \circledast \tilde{\psi}_i^2\right) \end{aligned} \tag{100}$$

where the last equality comes from (A.9) and (A.6) in Lemma 14. Note that this does not guarantee the PR because the low frequency component $\Phi\Phi^\top(f \circledast \psi_i)$ is contained in both terms of (100); so the low-frequency component is overly emphasized, which is believed to be the main source of smoothing.

4.2. Proposed multi-resolution analysis. To address the limitation of U-net, here we propose a novel multi-resolution analysis using wavelet non-local basis. As discussed before, at the first layer, we are interested in learning $\Psi^{(1)}$ and $\tilde{\Psi}^{(1)}$ such that

$$\mathbb{H}_{d_{(1)}}(f) = \Phi^{(1)} C^{(1)} \tilde{\Psi}^{(1)\top}, \quad \text{where} \quad C^{(1)} := \Phi^{(1)\top} \mathbb{H}_{d_{(1)}}(f) \Psi^{(1)}$$

For MRA, we decompose the nonlocal orthonormal basis $\Phi^{(1)}$ into the low and high frequency subbands, i.e.

$$\Phi^{(1)} = \begin{bmatrix} \Phi^{(1)}_{low} & \Phi^{(1)}_{high} \end{bmatrix} .$$

For example, if we use Haar wavelet, the first layer operator $\Phi^{(1)}_{low}, \Phi^{(1)}_{high} \in \mathbb{R}^{n \times \frac{n}{2}}$ are given by

$$\Phi^{(1)}_{low} = \frac{1}{\sqrt{2}} \begin{bmatrix} 1 & 0 & \cdots & 0 \\ 1 & 0 & \cdots & 0 \\ 0 & 1 & \cdots & 0 \\ 0 & 1 & \cdots & 0 \\ \vdots & \vdots & \ddots & \vdots \\ 0 & 0 & \cdots & 1 \\ 0 & 0 & \vdots & 1 \end{bmatrix}, \quad \Phi^{(1)}_{high} = \frac{1}{\sqrt{2}} \begin{bmatrix} 1 & 0 & \cdots & 0 \\ -1 & 0 & \cdots & 0 \\ 0 & 1 & \cdots & 0 \\ 0 & -1 & \cdots & 0 \\ \vdots & \vdots & \ddots & \vdots \\ 0 & 0 & \cdots & 1 \\ 0 & 0 & \vdots & -1 \end{bmatrix}$$

Note that $\Phi^{(1)}_{low}$ is exactly the same as the average pooling operation in (96); however, unlike the pooling in U-net, $\Phi^{(1)} = \begin{bmatrix} \Phi^{(1)}_{low} & \Phi^{(1)}_{high} \end{bmatrix}$ now constitutes an orthonormal basis in $\mathbb{R}^n$ thanks to $\Phi^{(1)}_{high}$. We also define the approximate signal $C^{(1)}_{low}$ and the detail signal $C^{(1)}_{high}$:

$$C^{(1)}_{low} := \Phi^{(1)\top}_{low} \mathbb{H}_{d_{(1)}}(f) \Psi^{(1)} = \Phi^{(1)\top}_{low} (f \circledast \overline{\Psi}^{(1)})$$
$$C^{(1)}_{high} := \Phi^{(1)\top}_{high} \mathbb{H}_{d_{(1)}}(f) \Psi^{(1)} = \Phi^{(1)\top}_{high} (f \circledast \overline{\Psi}^{(1)})$$

such that

$$C^{(1)} = \Phi^{(1)\top} \mathbb{H}_{d_{(1)}}(f) \Psi^{(1)} = \begin{bmatrix} C^{(1)}_{low} \\ C^{(1)}_{high} \end{bmatrix}$$

Note that this operation corresponds to the local filtering followed by non-local basis matrix multiplication as shown in the red block of Fig. 9(a). Then, at the first layer, we have the following decomposition:

$$\mathbb{H}_{d_{(1)}}(f) = \Phi^{(1)} C^{(1)} \tilde{\Psi}^{(1)\top} = \Phi^{(1)}_{low} C^{(1)}_{low} \tilde{\Psi}^{(1)\top} + \Phi^{(1)}_{high} C^{(1)}_{high} \tilde{\Psi}^{(1)\top}$$

At the second layer, we proceed similarly using the approximate signal $C^{(1)}_{low}$. More specifically, we are interested in using orthonormal non-local bases: $\Phi^{(2)} = \begin{bmatrix} \Phi^{(2)}_{low} & \Phi^{(2)}_{high} \end{bmatrix}$, where $\Phi^{(2)}_{low}$ and $\Phi^{(2)}_{high}$ transforms the approximate signal $C^{(1)}_{low} \in \mathbb{R}^{n/2 \times d_{(1)}}$ to low and high bands, respectively (see Fig. 9(a)):

$$\mathbb{H}_{d_{(2)}|p_{(2)}}(C^{(1)}_{low}) = \Phi^{(2)}_{low} C^{(2)}_{low} \tilde{\Psi}^{(2)\top} + \Phi^{(2)}_{high} C^{(2)}_{high} \tilde{\Psi}^{(2)\top},$$

where $p_{(2)} = d_{(1)}$ denotes the number of Hankel blocks in (10), $d_{(2)}$ is the second layer convolution filter length, and

$$C^{(2)}_{low} := \Phi^{(2)\top}_{low} \mathbb{H}_{d_{(2)}|p_{(2)}}(C^{(1)}_{low}) \Psi^{(2)} = \Phi^{(2)\top}_{low} (C^{(1)}_{low} \circledast \overline{\Psi}^{(2)})$$
$$C^{(2)}_{high} := \Phi^{(2)\top}_{high} \mathbb{H}_{d_{(2)}|p_{(2)}}(C^{(1)}_{low}) \Psi^{(2)} = \Phi^{(2)\top}_{high} (C^{(1)}_{low} \circledast \overline{\Psi}^{(2)}) \tag{101}$$

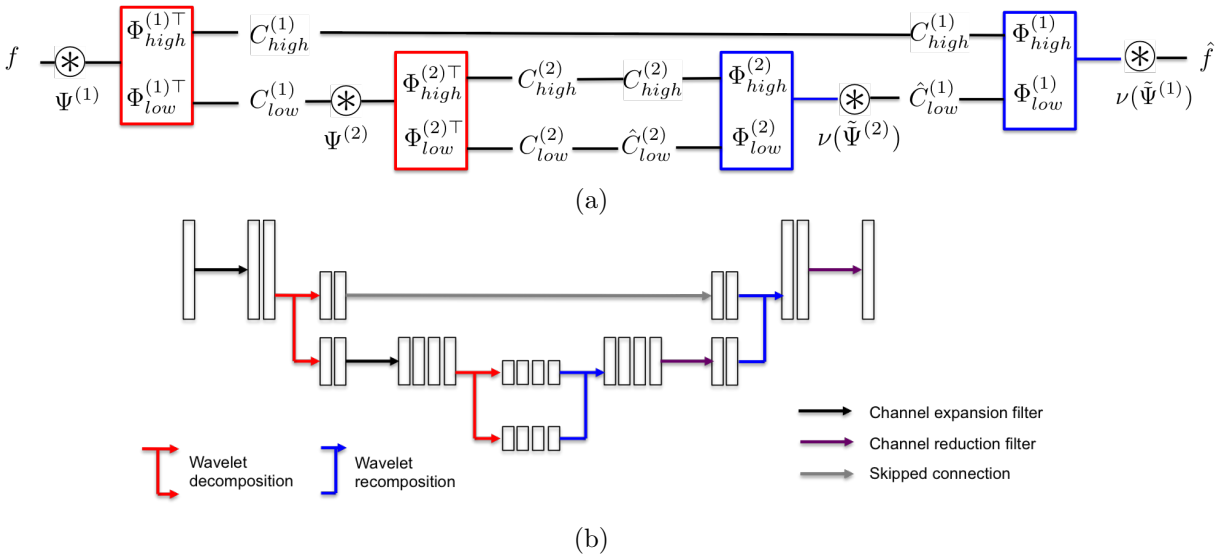


FIG. 9. *(a) Proposed multi-resolution analysis of deep convolutional framelets. Here, ⊛ corresponds to the convolution operation; the red and blue blocks correponds to the encoder and decoder blocks, respectively. (b) An example of multi-resolution deep convolutional framelet decomposition with a length-2 local filters.*

Again, $\Phi_{low}^{(2)}$ corresponds to the standard average pooling operation. Note that we need a lifting operation to an extended Hankel matrix with $p_{(2)} = d_{(1)}$ Hankel blocks in (101), because the first layers generates $p_{(2)}$ filtered output which needs to be convolved with $d_{(2)}$-length filters in the second layer.

Similarly, the approximate signal needs further processing from the following layers. In general, for $l = 1, \cdots, L$, we have

$$\mathbb{H}_{d_{(l)}|p_{(l)}}(C_{low}^{(l-1)}) = \Phi_{low}^{(l)} C_{low}^{(l)} \tilde{\Psi}^{(l)\top} + \Phi_{high}^{(l)} C_{high}^{(l)} \tilde{\Psi}^{(l)\top},$$

where

$$\begin{aligned} C_{low}^{(l)} &:= \Phi_{low}^{(l)\top} \mathbb{H}_{d_{(l)}|p_{(l)}}(C_{low}^{(l-1)}) \Psi^{(l)} = \Phi_{low}^{(l)\top} (C_{low}^{(l-1)} \circledast \overline{\Psi}^{(l)}) \\ C_{high}^{(l)} &:= \Phi_{high}^{(l)\top} \mathbb{H}_{d_{(l)}|p_{(l)}}(C_{low}^{(l-1)}) \Psi^{(l)} = \Phi_{high}^{(l)\top} (C_{low}^{(l-1)} \circledast \overline{\Psi}^{(l)}) \end{aligned}$$

where $p_{(l)}$ denotes the dimension of local basis at l-th layer. This results in L-layer deep convolutional framelets using Haar wavelet.

The multilayer implementation of convolution framelets now results in an interesting encoder-decoder deep network structure as shown in Fig. 9(a), where the red and blue blocks represent encoder and decoder blocks, respectively. In addition, Table 2 summarizes the dimension of the l-th layer matrices. More specifically, with the ReLU, the encoder parts are given as follows:

$$\begin{cases} C_{low}^{(1)} = \rho\left(\Phi_{low}^{(1)\top}\left(f \circledast \overline{\Psi}^{(1)}\right)\right), & C_{high}^{(1)} = \Phi_{high}^{(1)\top}\left(f \circledast \overline{\Psi}^{(1)}\right) \\ C_{low}^{(2)} = \rho\left(\Phi_{low}^{(2)\top}\left(C_{low}^{(1)} \circledast \overline{\Psi}^{(2)}\right)\right), & C_{high}^{(2)} = \Phi_{high}^{(2)\top}\left(C_{low}^{(1)} \circledast \overline{\Psi}^{(2)}\right) \\ & \vdots \\ C_{low}^{(L)} = \rho\left(\Phi_{low}^{(L)\top}\left(C_{low}^{(L-1)} \circledast \overline{\Psi}^{(L)}\right)\right), & C_{high}^{(L)} = \Phi_{high}^{(L)\top}\left(C_{low}^{(L-1)} \circledast \overline{\Psi}^{(L)}\right) \end{cases}$$

On the other hand, the decoder part is given by

$$\begin{cases} \hat{C}_{low}^{(L-1)} & = \rho\left(\mathbb{H}^{\dagger}_{d_{(L)}|p_{(L)}}\left(\Phi^{(L)}\hat{C}^{(L)}\tilde{\Psi}^{(L)\top}\right)\right) = \rho\left(\left(\Phi^{(L)}\hat{C}^{(L)}\right)\circledast\nu(\tilde{\Psi}^{(L)\top})\right) \\ & \vdots \\ \hat{C}_{low}^{(1)} & = \rho\left(\mathbb{H}^{\dagger}_{d_{(2)}|p_{(2)}}\left(\Phi^{(2)}\hat{C}^{(2)}\tilde{\Psi}^{(2)\top}\right)\right) = \rho\left(\left(\Phi^{(2)}\hat{C}^{(2)}\right)\circledast\nu(\tilde{\Psi}^{(2)\top})\right) \\ \hat{f} & = \mathbb{H}^{\dagger}_{d_{(1)}}\left(\Phi^{(1)}\hat{C}^{(1)}\tilde{\Psi}^{(1)\top}\right) = \rho\left(\left(\Phi^{(1)}\hat{C}^{(1)}\right)\circledast\nu(\tilde{\Psi}^{(1)\top})\right) \end{cases} \tag{102}$$

where $\nu(\Psi)$ is defined in (54) and we use

$$\Phi^{(l)}\hat{C}^{(l)}\tilde{\Psi}^{(l)\top} = \Phi^{(l)}_{low}\hat{C}^{(l)}_{low}\tilde{\Psi}^{(l)\top} + \Phi^{(l)}_{high}\hat{C}^{(l)}_{high}\tilde{\Psi}^{(l)\top} \ .$$

where we could further process high frequency components as

$$\hat{C}^{(L)}_{high} = C^{(L)}_{high}\circledast H^{(L)} \tag{103}$$

for some filter $H^{(L)}$, and $\hat{C}^{(L)}_{low}$ is the decoded low frequency band from $(L-1)$-th resolution layer, which can be further processed with additional filters.

TABLE 2
The nomenclature and dimensions of the matrices at the l-th layer MRA using deep convolutional framelet. Here, $d_{(l)}$ denotes the filter length, and $p_{(l)} = p_{(l-1)}d_{(l-1)}$ with $p_{(0)} = d_{(0)} = 1$ refers to the number of Hankel block.

Name	Symbol	Dimension
Non-local basis	$\Phi^{(l)}$	$\frac{n}{2^{l-1}} \times \frac{n}{2^{l-1}}$
Low-band non-local basis	$\Phi^{(l)}_{low}$	$\frac{n}{2^{l-1}} \times \frac{n}{2^{l}}$
High-band non-local basis	$\Phi^{(l)}_{high}$	$\frac{n}{2^{l-1}} \times \frac{n}{2^{l}}$
Local basis	$\Psi^{(l)}$	$p_{(l)}d_{(l)} \times p_{(l)}d_{(l)}$
Dual local basis	$\tilde{\Psi}^{(l)}$	$p_{(l)}d_{(l)} \times p_{(l)}d_{(l)}$
Signal and its estimate	$C^{(l)}, \hat{C}^{(l)}$	$\frac{n}{2^{l-1}} \times p_{(l)}d_{(l)}$
Approximate signal and its estimate	$C^{(l)}_{low}, \hat{C}^{(l)}_{low}$	$\frac{n}{2^{l}} \times p_{(l)}d_{(l)}$
Detail signal	$C^{(l)}_{high}$	$\frac{n}{2^{l}} \times p_{(l)}d_{(l)}$
Hankel lifting of low-band signals	$\mathbb{H}_{d_{(l)}\|p_{(l)}}(C^{(l-1)}_{low})$	$\frac{n}{2^{l-1}} \times p_{(l)}d_{(l)}$

Fig. 9(b) shows the overall structure of multi-resolution analysis with convolutional framelets when length-2 local filters are used. Note that the structure is quite similar to U-net structure [59], except for the high pass filter pass. This again confirms a close relationship between the deep convolutional framelets and deep neural networks.

5. Experimental Results. In this section, we investigate various inverse problem applications of deep convolutional framelets, including image denoising, sparse view CT reconstruction, and inpainting. In particular, we will focus on our novel multi-resolution deep convolutional framelets using Haar wavelets. For these applications, our multi-resolution deep convolutional framelets should be extended to 2-D structure, so the architecture in Fig. 9(b) should be modified. The resulting architectures are illustrated in Figs. 10(b)(c). The 2-D U-Net, which is used as one of our reference networks, is shown in Fig. 10(a). Note that the U-Net in Fig. 10(a) is exactly the same as the reconstruction network for inverse problems in Jin et al [35] and Han et al [29].

More specifically, the networks are composed of convolution layer, ReLU, and skip connection with concatenation. Each stage consists of four 3×3 convolution layers followed by ReLU, except for the final stage and the last layer. The final stage is composed of two 3×3 convolution layers for each low-pass and high-pass branch, and the last layer is 1×1 convolution layer. In Figs. 10(b)(c), we use the 2-D Haar wavelet decomposition and recomposition instead of the standard pooling and

unpooling. Thus, at each pooling layer, the wavelet transform generates four subbands: HH, HL, LH, and LL bands. Then, the LL band is processed using convolutional layers followed by another wavelet-based pooling layer. As shown in Figs. 10(b)(c), the channels are doubled after wavelet decomposition. Therefore, the number of convolution kernels increases from 64 in the first layer to 1024 in the final stage. In Fig. 10(b) we have additional filters for the high-pass branches of the highest layer, whereas Fig. 10(c) only has skipped connection. The reason why we do not include an additional filter in Fig. 10(c) is to verify that the improvement over U-net is not from the additional filters in the high-pass bands but rather comes from wavelet-based non-local basis. For a fair comparison with U-net structure in Fig. 10(a), our proposed network in Figs. 10(b)(c) also have concatenation layers that stack all subband signals before applying filtering.

Although Figs. 10(b)(c) and Fig. 10(a) appear similar, there exists fundamental differences due to the additional high-pass connections. In particular, in Figs. 10(b)(c), there exist skipped connections at the HH, HL, and LH subbands, whereas U-Net structure in Fig. 10(a) does not have high pass filtering before the bypass connection. Accordingly, as explained in Section 4.1, the U-Net does not satisfy the frame condition, emphasizing the low-pass components. On the hand, our networks in Figs. 10(b)(c) do satisfy the frame condition so we conjecture that high pass signals can be better recovered by the proposed network. Our numerical results in the following indeed provide empirical evidence of our claim.

5.1. Image denoising. Nowadays, deep CNN-based algorithms have achieved great performance in image denoising [4, 77]. In this section, we will therefore show that the proposed multi-resolution deep convolutional framelet outperforms the standard U-Net in denoising task. Specifically, the proposed network and other networks were trained to learn the noise pattern similar to the existing work [77]. Then, the noise-free image can be obtained by subtracting the estimated noises.

For training and validation, DIVerse 2K resolution images (DIV2K) dataset [2] was used to train the proposed network in Fig. 10(b). Specifically, 800 and 200 images from the dataset were used for training and validation, respectively. The noisy input images were generated by adding Gaussian noise of $\sigma = 30$. To train the network with various noise patterns, the Gaussian noise was re-generated in every epoch during training.

The proposed network was trained by Adam optimization [43] with the momentum $\beta_1 = 0.5$. The initial learning rate was set to 0.0001, and it was divided in half at every 25 iterations, until it reached around 0.00001. The size of patch was 256×256, and 8 mini-batch size was used. The network was trained using 249 epochs. The proposed network was implemented in Python using TensorFlow library [1] and trained using a GeForce GTX 1080. The Gaussian denoising network took about two days for training.

The standard U-net structure in Fig. 10(a) was used for the baseline network for comparison. In addition, RED-Net [52] was used as another baseline network for comparison. For a fair comparison, RED-Net was implemented using the identical hyperparameters. More specifically, the number of filter channels at the finest scale was 64 and we use 3×3 filters. Furthermore, we used 8 mini-batsh size. These networks were trained under the same conditions. To evaluate the trained network, we used Set12, Set14, and BSD68, and the peak signal-to-noise ratio (PSNR) and structural similarity (SSIM) index [68] were calculated for a quantitative evaluation. The PSNR is used to measure the quality of the reconstructed image, which is defined as

$$PSNR = 20 \cdot \log_{10} \left(\frac{MAX_Y}{\sqrt{MSE(\widehat{X}), Y)}} \right), \tag{104}$$

where $\widehat{X}$ and Y denote the reconstructed image and noise-free image (ground truth), respectively. MAX_Y is the maximum value of noise-free image. SSIM is used to measure the similarity between original image and distorted image due to deformation, and it is defined as

$$SSIM = \frac{(2\mu_{\widehat{X}}\mu_Y + c_1)(2\sigma_{\widehat{X}Y} + c_2)}{(\mu_{\widehat{X}}^2 + \mu_Y^2 + c_1)(\sigma_{\widehat{X}}^2 + \sigma_Y^2 + c_2)}, \tag{105}$$

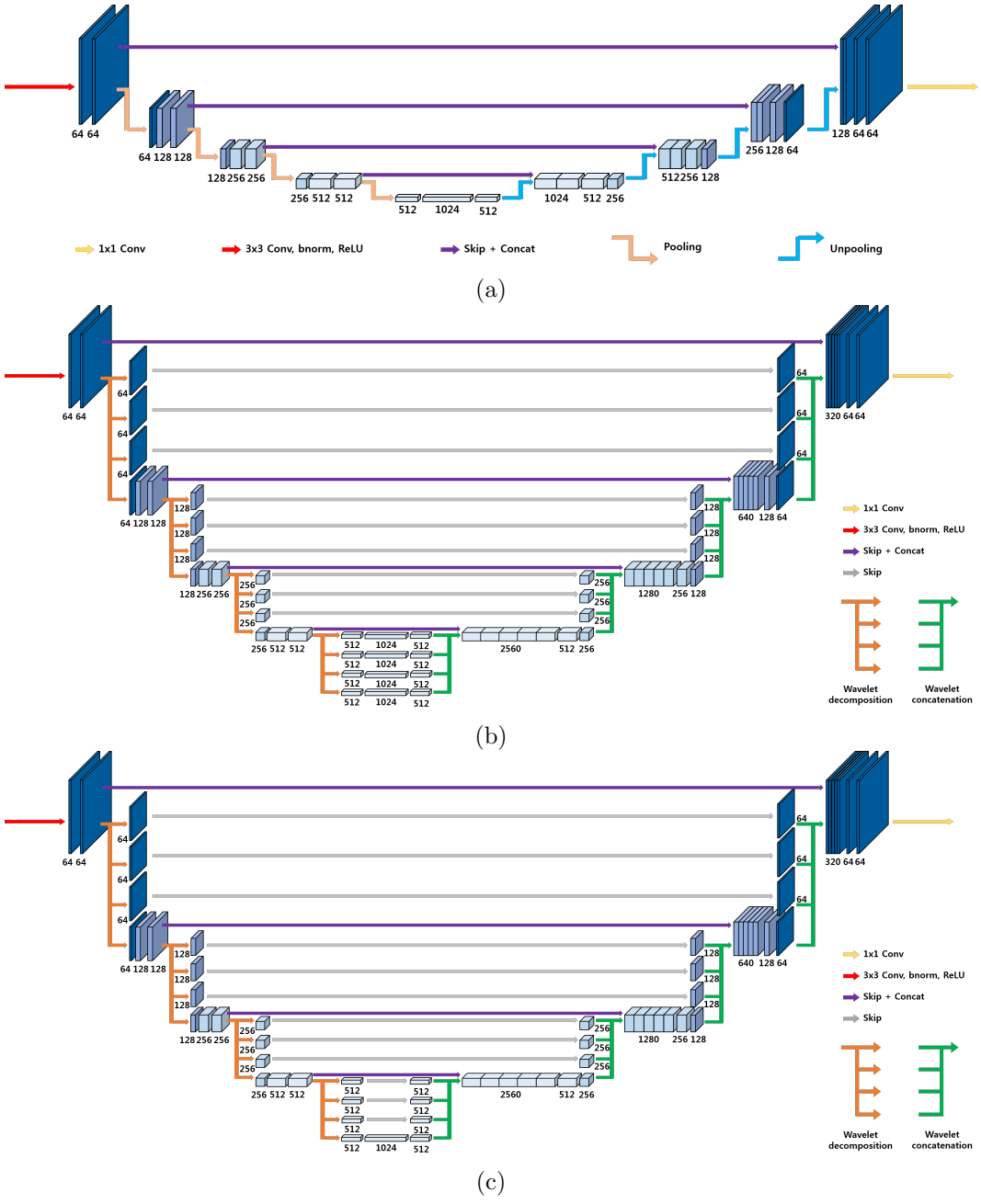


FIG. 10. *(a) U-Net structure used in [35], which is used for our comparative studies. Proposed multi-resolution deep convolutional framelets structures for (b) our denoising, and in-painting experiments, and for (c) sparse-view CT reconstruction, respectively.*

where μ_M is a average of M, σ_M^2 is a variance of M and σ_{MN} is a covariance of M and N. To stabilize the division, $c_1 = (k_1 R)^2$ and $c_2 = (k_2 R)^2$ are defined in terms of R, which is the dynamic range of the pixel values. We followed the default values of $k_1 = 0.01$ and $k_2 = 0.03$.

Table 3 shows the quantitative comparison of denoising performance. The proposed network was superior to U-Net and RED-Net in terms of PSNR for all test datasets with Gaussian noise $\sigma = 30$. Specifically, edge structures were smoothed out by the standard U-Net and RED-Net, whereas edge

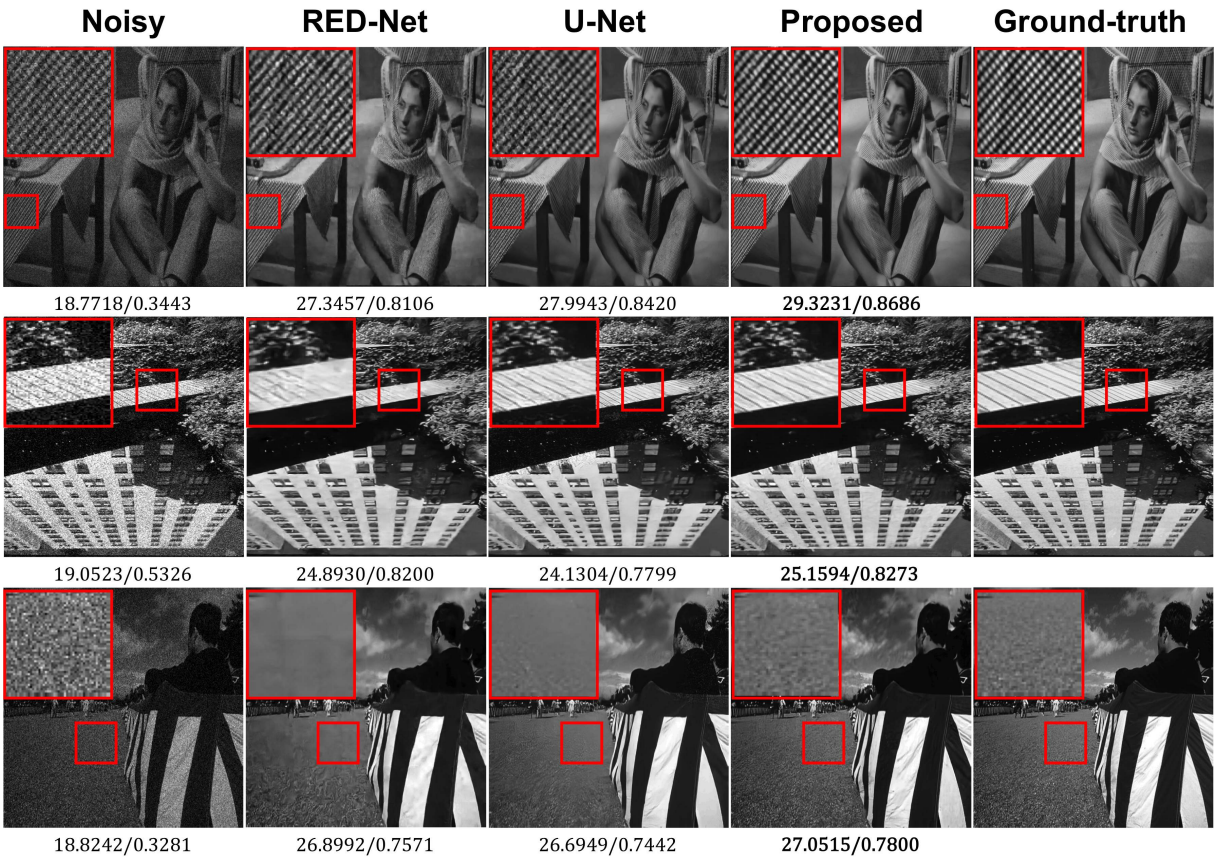


FIG. 11. *Denoising results for U-Net, RED-Net [52], and the proposed deep convolutional framelets from Gaussian noise with* $\sigma = 30$.

structures were quite accurately recovered by the proposed network, as shown in Fig. 11. This is because of the additional high-pass branches in the proposed network, which make the image detail well recovered. These results confirm that imposing the frame condition for the non-local basis is useful in recovering high resolution image as predicted by our theory.

TABLE 3
Performance comparison in the PSNR/SSIM index for different data sets in the noise removal tasks from Gaussian noise with $\sigma = 30$.

Dataset (σ)	Input	RED-Net [52]	U-Net	Proposed
Set12 (30)	18.7805/0.2942	28.7188/0.8194	28.9395/0.8118	**29.5126**/**0.8280**
Set14 (30)	18.8264/0.3299	28.4994/**0.7966**	27.9911/0.7764	**28.5978**/0.7866
BSD68 (30)	18.8082/0.3267	27.8420/**0.7787**	27.7314/0.7749	**27.8836**/0.7761

5.2. Sparse-view CT Reconstruction. In X-ray CT, due to the potential risk of radiation exposure, the main research thrust is to reduce the radiation dose. Among various approaches for low-dose CT, sparse-view CT is a recent proposal that reduces the radiation dose by reducing the number of projection views [62]. However, due to the insufficient projection views, standard reconstruction using the filtered back-projection (FBP) algorithm exhibits severe streaking artifacts that are globally distributed. Accordingly, researchers have extensively employed compressed sensing approaches [20] that minimize the total variation (TV) or other sparsity-inducing penalties under the data fidelity

[62]. These approaches are, however, computationally very expensive due to the repeated applications of projection and back-projection during iterative update steps.

Therefore, the main goal of this experiment is to apply the proposed network for sparse view CT reconstruction such that it outperforms the existing approaches in its computational speed as well as reconstruction quality. To address this, our network is trained to learn streaking artifacts as suggested in [29, 28, 35], using the new network architecture in Fig. 10(c). As a training data, we used the ten patient data provided by AAPM Low Dose CT Grand Challenge (http://www.aapm.org/GrandChallenge/LowDoseCT/). The initial images were reconstructed by 3-D CT 2304 projection data. To generate several sparse view images, the measurements were re-generated by *radon* operator in MATLAB. The data is composed of 2-D CT projection data from 720 views. Artifact-free original images were generated by *iradon* operator in MATLAB using all 720 projection views. The input images with streaking artifacts were generated using *iradon* operator from 60, 120, 240, and 360 projection views, respectively. These sparse view images correspond to each donwsampling factor x12, x6, x3, and x2. Then, the network was trained to remove the artifacts.

Among the ten patient data, eight patient data were used for training, one patient data was used for validation, and a test was conducted using the remaining another patient data. This corresponds to 3720 and 254 slices of 512×512 images for the training and validation data, respectively, and 486 slices of 512×512 images for the test data. The training data was augmented by conducting horizontal and vertical flipping.

As for the baseline network for comparison, we use the U-net structure in Fig. 10(a) and a single resolution CNN similar to the experimental set-up in Jin et al [35] and Han et al [29]. The single resolution CNN has the same architecture with U-net in Fig. 10(a), except that pooling and unpooling were not used. All these networks were trained similarly using the same data set. For quantitative evaluation, we use the normalized mean square error (NMSE) and the peak signal-to-noise ratio (PSNR).

The proposed network was trained by stochastic gradient descent (SGD). The regularization parameter was $\lambda = 10^{-4}$. The learning rate was set from 10^{-3} to 10^{-5} which was gradually reduced at each epoch. The number of epoch was 150. A mini-batch data using image patch was used, and the size of image patch was 256×256. The network was implemented using MatConvNet toolbox (ver.24) [65] in MATLAB 2015a environment (Mathwork, Natick). We used a GTX 1080 Ti graphic processor and i7-7770 CPU (3.60GHz). The network takes about 4 days for training. Baseline networks were trained similarly.

Table 4 illustrates the average PSNR values for reconstruction results from various number of projection views. Due to the high-pass branch of the network, the deep convolutional framelets produced consistently improved images quantitatively across all view downsampling factors. Moreover, visual improvements from the proposed network are more remarkable. For example, Fig. 12(a)-(e) shows reconstruction results from 60 projection views. Due to the severe view downsampling, the FBP reconstruction result in Fig. 12(b) provides severely corrupted images with significant streaking artifacts. Accordingly, all the reconstruction results in Fig. 12(c)-(e) were not compatible to the full view reconstruction results in Fig. 12(a). In particular, there are significant remaining streaking artifacts for the conventional CNN architecture (Fig. 12(c)), which were reduced using U-net as shown

TABLE 4
Average PSNR results comparison for reconstruction results from various projection views and algorithms. Here, CNN refers to the single resolution network.

PSNR [dB]	60 views (x12)	90 views (x8)	120 views (x6)	180 views (x4)	240 views (x3)	360 views (x2)
FBP	22.2787	25.3070	27.4840	31.8291	35.0178	40.6892
CNN	36.7422	38.5736	40.8814	42.1607	43.7930	44.8450
U-net	38.8122	40.4124	41.9699	43.0939	44.3413	45.2366
Proposed	**38.9218**	**40.5091**	**42.0457**	**43.1800**	**44.3952**	**45.2552**

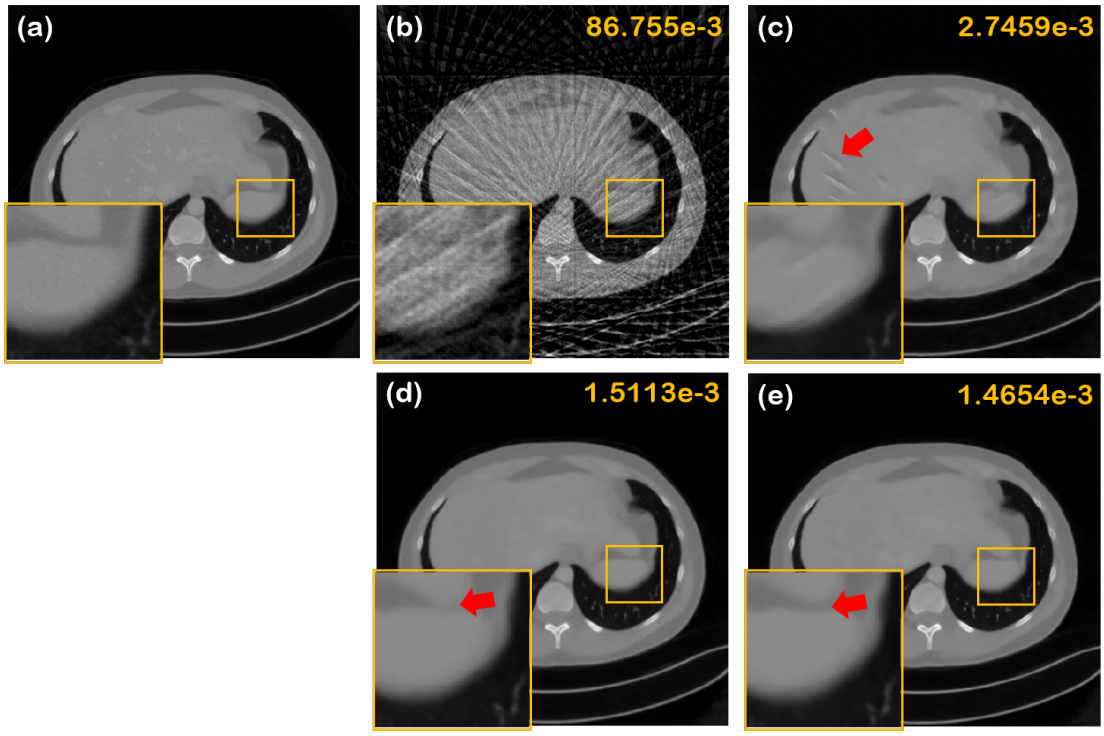


FIG. 12. *CT reconstruction result comparison from 60 views. The number on the top right corner represents the NMSE values, and the red arrow refers to the area of noticeable differences. The yellow boxes denote the zoomed area. FBP reconstruction results from (a) full projection views, and (b) 60 views. Reconstruction results by (c) CNN, (d) U-net, and (e) the proposed multi-resolution deep convolutional framelets.*

in Fig. 12(d). However, as indicated by the arrow, some blurring artifacts were visible in Fig. 12(d). On the other hand, the proposed network removes the streaking and blurring artifact as shown in Fig. 12(e). Quantitative evaluation also showed that the proposed deep convolutional framelets has the minimum NMSE values.

As for reconstruction results from larger number of projection views, Fig. 13(a)-(e) show reconstruction results from 90 projection views. All the algorithms significantly improved compared to the 60 view reconstruction. However, in the reconstruction results by single resolution CNN in Fig. 13(b) and U-net in Fig. 13(c), the details have disappeared. On the other hand, most of the detailed structures were well reconstructed by the proposed deep convolutional framelets as shown in Fig. 13(e). Quantitative evaluation also showed that the proposed deep convolutional framelets has the minimum NMSE values. The zoomed area in Fig. 13(a)-(e) also confirmed the findings. The reconstruction result by the deep convolutional framelets provided very realistic image, whereas the other results are somewhat blurry.

These experimental results clearly confirmed that the proposed network is quite universal in the sense it can be used for various artifact patterns. This is due to the network structure retaining the high-pass subbands, which automatically adapts the resolutions even though various scale of image artifacts are present.

5.3. Image inpainting. Image inpainting is a classical image processing problem whose goal is to estimate the missing pixels in an image. Image inpainting has many scientific and engineering applications. Recently, the field of image inpainting has been dramatically changed due to the advances of CNN-based inpainting algorithms [70, 57, 73]. One of the remarkable aspects of these approaches is the superior performance improvement over the existing methods in spite of its ultra-fast run time speed. Despite this stellar performance, the link between deep learning and classical inpainting

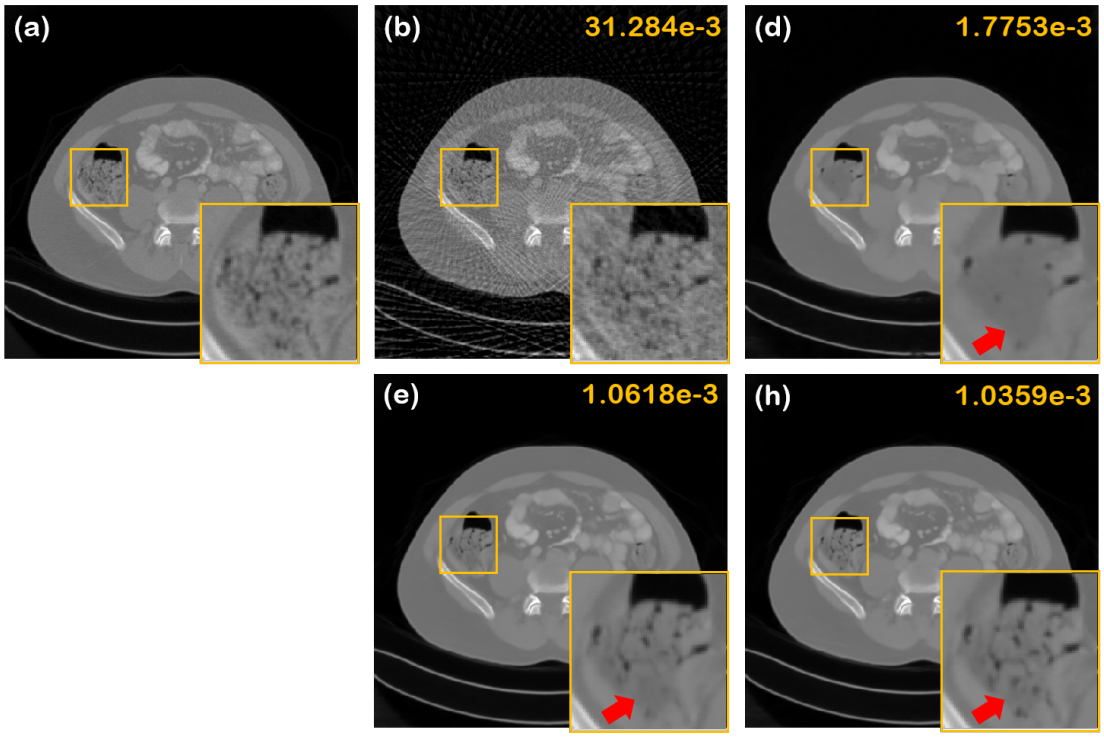


FIG. 13. *CT reconstruction result comparison from 90 views. The number on the top right corner represents the NMSE values, and the red arrow refers to the area of noticeable differences. The yellow boxes denote the zoomed area. FBP reconstruction results from (a) full projection views, and (b) 90 views. Reconstruction results by (c) CNN, (d) U-net, and (e) the proposed multi-resolution deep convolutional framelets.*

approaches remains poorly understood. In this section, inspired by the classical frame-based inpainting algorithms [11, 12, 10], we will show that the CNN-based image inpainting algorithm is indeed the first iteration of deep convolutional framelet inpainting, so the inpainting performance can be improved with multiple iterations of inpainting and image update steps using CNN.

More specifically, similar to the classical frame-based inpainting algorithms [11, 12, 10], we use the update algorithm in Eq. (92) derived from PR condition, which is written again as follows:

$$f_{n+1} = \mu P_\Lambda g + (I - \mu P_\Lambda)\mathcal{Q}(f_n) \ , \tag{106}$$

where $\mathcal{Q}$ is our deep convolutional framelet output. However, unlike the existing works using tight frames [11, 10], our deep convolutional framelet does not satisfy the tight frame condition; so we relax the iteration using Krasnoselskii-Mann (KM) method [6] as summarized in Algorithm 1.

Algorithm 1 Pseudocode implementation.

Train a deep network $\mathcal{Q}$ using training data set.
Set $0 \leq \mu < 1$ and $0 < \lambda_n < 1, \forall n$.
Set initial guess of f_0 and f_1.
for $n = 1, 2, \ldots,$ until convergence **do**
    $q_n := \mathcal{Q}(f_n)$.
    $\bar{f}_{n+1} := \mu P_\Lambda g + (I - \mu P_\Lambda) q_n$
    $f_{n+1} := f_n + \lambda_n (\bar{f}_{n+1} - f_n)$
end for

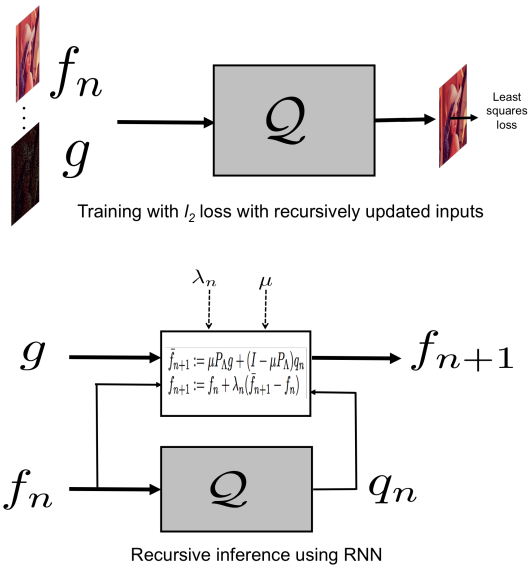


FIG. 14. *Proposed RNN architecture using deep convolutional framelets for training and inference steps.*



FIG. 15. *The proposed RNN results along iteration.*

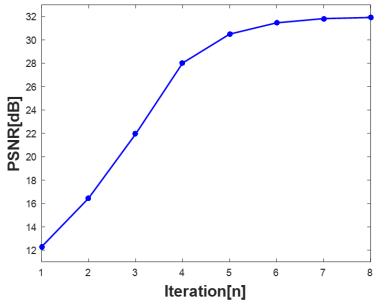


FIG. 16. *PSNR versus iteration for the results in Fig. 15.*

Note that the resulting inpainting algorithm assumes the form of the recursive neural network (RNN), because the CNN output is used as the input for the CNN for another iteration. The corresponding inference step based on Algorithm 1 is illustrated in Fig. 14. As for the CNN building block of the proposed RNN, the multi-resolution deep convolution framelets in Fig. 10(b) is used.

We performed inpainting experiments using randomly sub-sampled images. We used DIV2K dataset [2] for our experiments. Specifically, 800 images from the database were used for training, and 200 images was used for the validation. In addition, the training data was augmented by conducting



FIG. 17. *Image inpainting results for input images with %80 missing pixels in random locations.*

horizontal and vertical flipping and rotation. For the inpainting task of random sub-sampled images, 75%, 80%, and 85% of pixels in images were randomly removed from the images for every other epoch during the training. All images were rescaled to have values between 0 and 1. For training, Adam optimization [43] with the momentum $\beta_1 = 0.5$ was used. The learning rate for the generators was set to 0.0001, and it was divided in half every 50 iterations, until it reached around 0.00001. The size of patch was 128×128. We used 32 mini-batch size for training of the random missing images.

Since our network should perform inferences from intermediate reconstruction images, the network should be trained with respect to the intermediate results. Therefore, this training procedure is implemented using multiple intermediate results as inputs as shown in Fig. 14. In particular, we trained the network according to multiple stages. In the stage 1, we trained the network using the initial dataset, D_{init}, which is composed of missing images and corresponding label images. After the training of network using D_{init} converged, the input data for network training was replaced with the first inference result $f_1 = \mathcal{Q}_k(f_0)$ and the label images, where $\mathcal{Q}_k$ is k-th trained network and f_k denotes the k-th inference result. That is, at the k-th stage, the network was trained to fit the k-th inference result $f_k = \mathcal{Q}_l(f_{k-1})$ to the corresponding label data.

The proposed network was implemented in Python using TensorFlow library [1] and trained using a GeForce GTX 1080ti. The training time of inpainting network for randomly missing data was about six days.

To evaluate the trained network, we used Set5, Set14 and BSD100 dataset for testing. Fig. 15

TABLE 5
Performance comparison in terms of PSNR/SSIM index for various dataset in the inpainting task for 80% missing images.

Dataset	Input	RED-Net	Proposed
Set5	7.3861/0.0992	28.0853/0.9329	**28.4792/0.9368**
Set14	6.7930/0.0701	24.4556/0.8545	**25.7447/0.8649**
BSD100	7.8462/0.0643	**25.5847**/0.8510	25.4588/**0.8530**

shows typical image update from the proposed RNN structure. As iteration goes on, the images are gradually improved, as the CNN works as a image restoration network during the RNN update. The associated PSNR graph in Fig. 16 confirms that the algorithm converges after six RNN update steps. As a reference network for comparison, we compared our algorithm with RED-Net [52]. For a fair comparison, we trained RED-Net using the same 3×3 filter and the same number of channels of 64, which were also used for our proposed method. As shown in Fig. 17, the proposed method can restore the details and edges of images much better than RED-Net. In addition, the PSNR results in Table 5 for 80% missing pixel images indicated that the proposed method outperformed RED-Net in Set5 and Set14 data and was comparable for BSD100 datasets.

While most of the existing inpainting networks are based on feed-forward network [70, 57, 73], our theory of the deep convolutional framelets leads to a recursive neural network (RNN) that gradually improved the image with CNN-based image restoration, making the algorithm more accurate for various missing patterns. These results confirmed that the theoretical framework of deep convolutional framelets is promising in designing new deep learning algorithms for inverse problems.

6. Discussions. We also investigate whether our theory can answer current theoretical issues and intriguing empirical findings from machine learning community. Amazingly, our theoretical framework gives us many useful insights.

6.1. Low rankness of the extended Hankel matrix. In our theory, we showed that deep convolutional framelet is closely related to the Hankel matrix decomposition, so the multi-layer implementation of the convolutional framelet refines the bases such that maximal energy compaction can be achieved using a deep convolutional framelet expansion. In addition, we have previously shown that with insufficient filter channels, the rank structure of the extended Hankel matrix in successive layers is bounded by that of the previous layers. This perspective suggests that the energy compaction happens across layers, and this can be investigated by the singular value spectrum of the extended Hankel matrix.

Here, we provide empirical evidence that the singular value spectrum of the extended Hankel matrix is compressed by going through more convolutional layers. For this experiment, we used the single-resolution CNN with encoder-decoder architecture as shown in Fig. 18 for the sake of simplicity. Hyperparameters and dataset for the training were same as those introduced in our denoising experiments. Since energy compaction occurs at the convolutional framelet coefficients, we have considered only the encoder part corresponding to the network from the first module to the fifth module. As shown in Fig. 19, the singular value spectrum of the extended Hankel matrix is compressed by going through the layer. This confirms our conjecture that CNN is closely related to the low-rank Hankel matrix approximation.

6.2. Insights on classification networks. While our mathematical theory of deep convolutional framelet was derived for inverse problems, there are many important implications of our finding to general deep learning networks. For example, we conjecture that the classification network corresponds to the encoder part of our deep convolutional framelets. More specifically, the encoder part of the deep convolutional framelets works for the energy compaction, so the classifier attached to the encoder can discriminate the input signals based on the compressed energy distributions. This is sim-

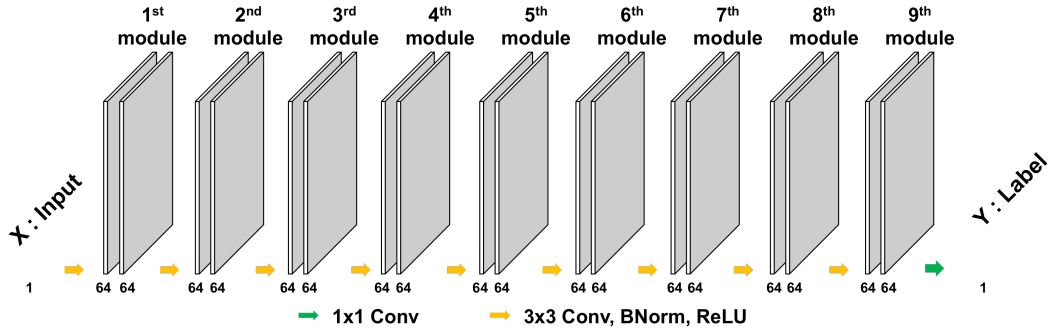


FIG. 18. *Single-resolution CNN architecture for image denoising.*

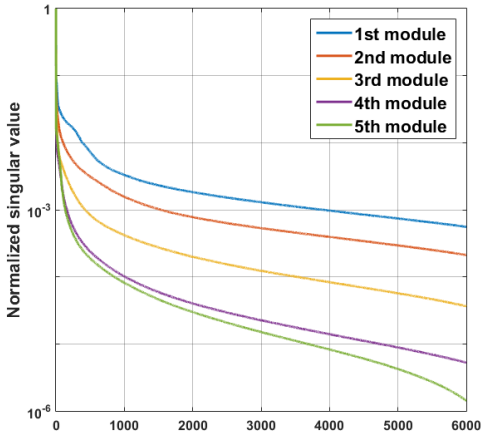


FIG. 19. *Normalized singular value plot of Hankel matrix constructed using the feature map from the* 1*st module to the* 5*th module.*

ilar with the classical classifier design, where the feature vector is first obtained by a dimensionality reduction algorithm, after which support vector machine (SVM) type classifier is used. Accordingly, the role of residual net, redundant channels, etc. are believed to hold for classifier networks as well. It is also important to note that the rank structure of Hankel matrix, which determines the energy distribution of convolutional framelets coefficients, is translation and rotation invariant as shown in [37]. The invariance property was considered the most important property which gives the theoretical motivation for Mallat's wavelet scattering network [51, 7]. Therefore, there may be an important connection between the deep convolutional framelets and wavelet scattering. However, this is beyond scope of current paper and will be left for future research.

6.3. Finite sample expressivity. Another interesting observation is that the perfect reconstruction is directly related to finite sample expressivity of a neural network [75]. Recently, there appeared a very intriguing article providing empirical evidences that the traditional statistical learning theoretical approaches fail to explain why large neural networks generalize well in practice [75]. To explain this, the authors showed that simple depth-two neural networks already have perfect finite sample expressivity as soon as the number of parameters exceeds the number of data points [75]. We conjecture that the perfect finite sample expressivity is closely related to the perfect reconstruction condition, saying that any finite sample size input can be reproduced perfectly using a neural network. The intriguing link between the PR condition and finite sample expressivity needs further investigation.

6.4. Relationship to pyramidal residual network. Another interesting aspect of our convolutional framelet analysis is the increases of filter channels as shown in (67). While this does not appear to follow the conventional implementation of the convolutional filter channels, there is a very interesting article that provides a strong empirical evidence supporting our theoretical prediction. In the recent paper on pyramidal residual network [26], the authors gradually increase the feature channels across layers. This design was proven to be an effective means of improving generalization ability. This coincides with our prediction in (67); that is, in order to guarantee the PR condition, the filter channel should increase. This again suggests the theoretical potential of the proposed deep convolutional framelets.

6.5. Revisit to the existing deep networks for inverse problems. Based on our theory for deep convolutional framelets, we now revisit the existing deep learning algorithms for inverse problems and discuss their pros and cons.

By extending the work in [39], Kang et al [41, 40] proposed a *wavelet domain residual learning (WavResNet)* for low-dose CT reconstruction as shown in Fig. 20. The key idea of WavResNet is to apply the directional wavelet transform first, after which a neural network is trained such that it can learn the mapping between noisy input wavelet coefficients and noiseless ones [41, 40]. In essence, this can be interpreted as a deep convolutional framelets with the nonlocal transform being performed first. The remaining layers are then composed of CNN with local filters and residual blocks. Thanks to the global transform using directional wavelets, the signal becomes more compressed, which is the main source of the advantages compared to the simple CNN. Another uniqueness of the WavResNet is the concatenation layer at the ends that performs additional filters by using all the intermediate results. This layer performs a signal *boosting* [41]. However, due to the lack of pooling layers, the receptive field size is smaller than that of multi-scale network as shown in Fig. 8. Accordingly, the architecture was better suited for localized artifacts from low-dose CT noise, but it is not effective for removing globalized artifact patterns from sparse view CT.

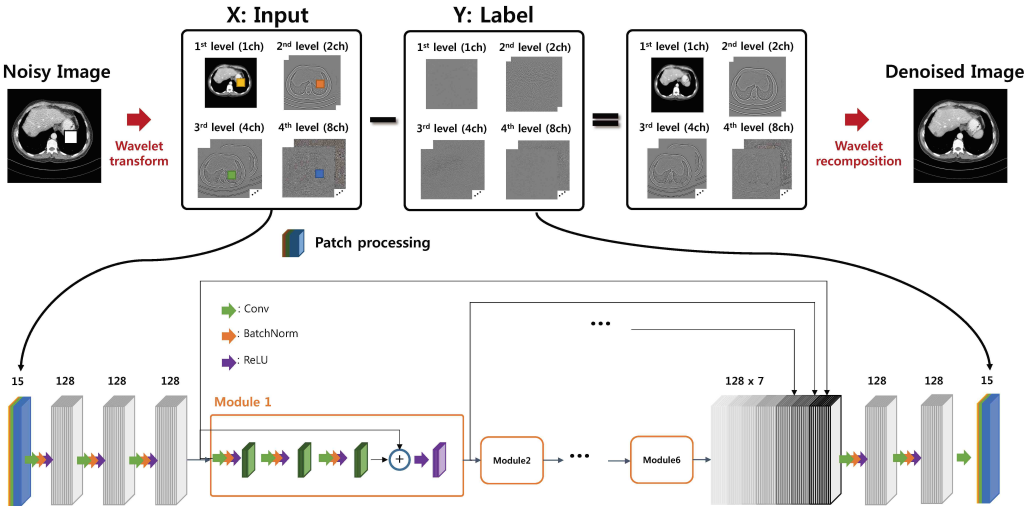


FIG. 20. *WavResNet architecture for low-dose CT reconstruction [41, 40].*

AUtomated TransfOrm by Manifold APproximation (AUTOMAP) [78] is a recently proposed neural network approach for image reconstruction, which is claimed to be general for various imaging modalities such as MRI, CT, etc. A typical architecture is given in Fig. 21. This architecture is similar to a standard CNN, except that at the first layer nonlocal basis matrix is learned as a fully connected layer. Moreover, the original signal domain is the measurement domain, so only local filters are followed in successive layer without additional fully connected layer for inversion. In theory, learning based non-local transform can be optimally adapted to the signals, so it is believed to be the advantageous over standard CNNs. However, in order to use the fully connected layer as nonlocal

bases, a huge size network is required. For example, in order to recover $N \times N$ image, the number of parameters for the fully connected layer is $2N^2 \times N^2$ as shown in Fig. 21 (see [78] for more calculation of required parameter numbers). Thus, if one attempts to learn the CT image of size 512×512 (i.e. $N = 2^9$) using AUTOMAP, the required memory becomes $2N^4 = 2^{37}$, which is neither possible to store nor to avoid any overfitting during the learning. This is another reason we prefer to use analytic non-local bases. However, if the measurement size is sufficiently small, the approach by AUTOMAP may be an interesting direction to investigate.

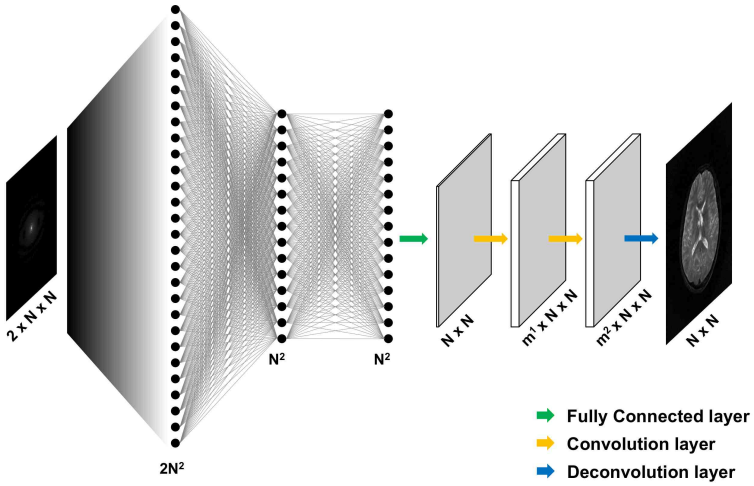


FIG. 21. *AUTOMAP architecture [78].*

7. Conclusions. In this paper, we propose a general deep learning framework called deep convolutional framelets for inverse problems. The proposed network architectures were obtained based on key fundamental theoretical advances we have achieved. First, we show that the deep learning is closely related to the existing theory of annihilating filter-based low-rank Hankel matrix approaches and convolution framelets. In particular, our theory was motivated by the observation that when a signal is lifted to a high dimensional Hankel matrix, it usually results in a low-rank structure. Furthermore, the lifted Hankel matrix can be decomposed using non-local and local bases. We further showed that the convolution framelet expansion can be equivalently represented as encoder-decoder convolutional layer structure. By extending this idea furthermore, we also derived the multi-layer convolution framelet expansion and associated encoder-decoder network. Furthermore, we investigated the perfect reconstruction condition for the deep convolutional framelets. In particular, we showed that the perfect reconstruction is still possible when the framelet coefficients are processed with ReLU. We also proposed a novel class of deep network using multi-resolution convolutional framelets.

Our discovery provided a theoretical rationale for many existing deep learning architectures and components. In addition, our theoretical framework can address some of the fundamental questions that we raised at Introduction. More specifically, we showed that the convolutional filters work as local bases and the number of channels can be determined based on the perfect reconstruction condition. Interestingly, by controlling the number of filter channels we can achieve a low-rank based shrinkage behavior. We further showed that ReLU can disappear when paired filer channels with opposite polarity are available. Another important and novel theoretical contribution is that, thanks to the lifting to the Hankel structured matrix, we can show that the pooling and un-pooling layers actually come from non-local bases, so they should be augmented with high-pass branches to meet the frame condition. Our deep convolutional framelets can also explain the role of the by-pass connection. Finally, we have shown that the depth of the network is determined considering the intrinsic rank of the signal and the convolution filter length. Our numerical results also showed that the proposed deep convolutional framelets can provide improved reconstruction performance under various conditions.

One of the limitations of the current work is that our analysis, such as PR, is based on a deterministic framework, while most of the mysteries of deep learning are probabilistic in nature, which apply in expectation over complex high-dimensional image distributions. To understand the link between the deterministic and probabilistic views of deep learning is very important, which need to be further explored in the future.

Appendix A. Basic properties of Hankel Matrices.

The following basic properties of Hankel matrix, which are mostly novel, will be useful in proving main theoretical results.

LEMMA 14. *For a given $f \in \mathbb{R}^n$, let $\mathbb{H}_d(f) \in \mathcal{H}(n,d)$ denote the associated Hankel matrix. Let $\Phi \in \mathbb{R}^{n\times m}$ and $\Psi \in \mathbb{R}^{d\times q}$ be matrices whose dimensions are chosen such that Φ and $\Psi^\top$ can be multiplied to the left and right to $\mathbb{H}_d(f)$. Suppose, furthermore, that $\tilde{\Phi} \in \mathbb{R}^{n\times m}$ and $\tilde{\Psi} \in \mathbb{R}^{d\times q}$ are another set of matrices that match the dimension of Φ and Ψ, respectively. Then, the following statements are true.*

1. *Let*

$$E_k = \frac{1}{\sqrt{d}}\mathbb{H}_d(e_k) \quad \in \mathcal{H}(n,d), \quad k = 1, \cdots, n \tag{A.1}$$

where e_k denotes the standard coordinate vector in $\mathbb{R}^n$, where only the k-th element is one. Then, the set $\{E_k\}_{k=1}^n$ is the orthonormal basis for the space of $\mathcal{H}(n,d)$.

2. *For a given E_k in (A.1), we have*

$$F := \mathbb{H}_d(f) = \sum_{k=1}^{n} \langle E_k, F\rangle E_k, \quad \text{where} \quad \langle E_k, \mathbb{H}_d(f)\rangle = \sqrt{d} f[k]. \tag{A.2}$$

3. *For any vectors $u, v \in \mathbb{R}^n$ and any Hankel matrix $F = \mathbb{H}_d(f) \in \mathcal{H}(n,d)$, we have*

$$\langle F, uv^\top\rangle = u^\top F v = u^\top (f \circledast \overline{v}) = f^\top (u \circledast v) = \langle f, u \circledast v\rangle \tag{A.3}$$

where $\overline{v}$ denotes the flipped version of the vector v.

4. *For a given E_k in (A.1), $u \in \mathbb{R}^n$, and $v \in \mathbb{R}^d$, we have*

$$\langle E_k, uv^\top\rangle = \frac{1}{\sqrt{d}}(u \circledast v)[k]. \tag{A.4}$$

5. *A generalized inverse of the lifting to the Hankel structure in (A.2) is given by*

$$\mathbb{H}_d^\dagger(B) = \frac{1}{\sqrt{d}} \begin{bmatrix} \langle E_1, B\rangle \\ \langle E_2, B\rangle \\ \vdots \\ \langle E_n, B\rangle \end{bmatrix} \tag{A.5}$$

where B is any matrix in $\mathbb{R}^{n\times d}$ and E_k's are defined in (A.1).

6. *For a given $C \in \mathbb{R}^{m\times q}$,*

$$\mathbb{H}_d^\dagger(\tilde{\Phi} C \tilde{\Psi}^\top) = \sum_{j=1}^{q} \mathbb{H}_d^\dagger(\tilde{\Phi} c_j \tilde{\psi}_j^\top) = \frac{1}{d}\sum_{j=1}^{q} ((\tilde{\Phi} c_j) \circledast \tilde{\psi}_j) \ , \tag{A.6}$$

$$= \frac{1}{d}\sum_{i=1}^{m}\sum_{j=1}^{q} c_{ij} (\tilde{\phi}_i \circledast \tilde{\psi}_j), \tag{A.7}$$

where $\tilde{\phi}_j, \tilde{\psi}_j$ and c_j denotes the j-th column of $\tilde{\Phi}, \tilde{\Psi}$ and C, respectively; and c_{ij} is the (i,j) elements of C.

7. *For any* $Y = \begin{bmatrix} Y_1 & \cdots & Y_p \end{bmatrix} \in \mathbb{R}^{n\times dp}$ *with* $Y_i \in \mathbb{R}^{n\times d}, i = 1, \cdots, p$, *suppose that an operator* L *satisfies*

$$L(Y) = \begin{bmatrix} \mathbb{H}_d^\dagger(Y_1) & \cdots & \mathbb{H}_d^\dagger(Y_p) \end{bmatrix} \in \mathbb{R}^{n\times p} \tag{A.8}$$

Then, L *is a generalized left-inverse of an extended Hankel operator* $\mathbb{H}_{d|p}$, *i.e.* $L = \mathbb{H}_{d|p}^\dagger$

8. *We have*

$$\mathbb{H}_d^\dagger(\mathbb{H}_d(f)\Psi\tilde{\Psi}^\top) = \frac{1}{d}\sum_{i=1}^{q}(f \circledast \overline{\psi}_i \circledast \tilde{\psi}_i) \quad \in \mathbb{R}^n \ . \tag{A.9}$$

9. *Let* $\Xi,\ \tilde{\Xi} \in \mathbb{R}^{pd\times pq}$ *denote any matrix with block structure:*

$$\tilde{\Xi}^\top = \begin{bmatrix} \tilde{\Xi}_1^\top & \cdots & \tilde{\Xi}_p^\top \end{bmatrix} \quad \textit{where} \quad \tilde{\Xi}_j^\top \in \mathbb{R}^{pq\times d}$$

Then, we have

$$\mathbb{H}_{d|p}^\dagger(\mathbb{H}_{d|p}([f_1, \cdots, f_p])\Xi\tilde{\Xi}^\top) = \frac{1}{d}\sum_{i=1}^{q}\sum_{j=1}^{p}\left[f_j \circledast \overline{\xi}_i^j \circledast \tilde{\xi}_i^1, \quad \cdots, \quad f_j \circledast \overline{\xi}_i^j \circledast \tilde{\xi}_i^p\right] \ . \tag{A.10}$$

where ξ_i^j *(resp.* $\tilde{\xi}_i^j$*) denotes the* i*-th column of* Ξ_j *(resp.* $\tilde{\Xi}_j$*).*

Proof. The proof is a simple application of the definition of Hankel matrix and convolutional framelet. We prove claims one by one:

(1) The proof can be found in [72].

(2) Because $\{E_k\}_{k=1}^n$ constitutes a orthonormal basis, for any $F \in \mathcal{H}(n, d)$, we have

$$F = \sum_{k=1}^{n}\langle E_k, F\rangle E_k.$$

Furthermore, the operator $\mathbb{H}_d : f \mapsto \mathcal{H}(n, d)$ is linear, so we have

$$\mathbb{H}_d(f) = \mathbb{H}_d\left(\sum_{k=1}^{n} f[k]e_k\right) = \sum_{k=1} f[k]\mathbb{H}_d(e_k) = \sqrt{d}\sum_{k=1}^{n} f[k]E_k$$

where the last equality comes from (A.1). Thus, $\langle E_k, \mathbb{H}_d(f)\rangle = \sqrt{d}f[k]$.

(3) The proof can be found in [74].

(4) Using (A.3) and $E_k = \mathbb{H}_d(e_k)/\sqrt{d}$, we have

$$\langle E_k, uv^\top\rangle = \frac{1}{\sqrt{d}}e_k^\top(u \circledast v) = \frac{1}{\sqrt{d}}(u \circledast v)[k] \ .$$

(5) We need to show that $\mathbb{H}_d^\dagger(\mathbb{H}_d(f)) = f$ for any $f = [f[1]\cdots f[n]]^T \in \mathbb{R}^n$.

$$\mathbb{H}_d^\dagger(\mathbb{H}_d(f)) = \frac{1}{\sqrt{d}}\begin{bmatrix}\langle E_1, \mathbb{H}_d(f)\rangle \\ \langle E_2, \mathbb{H}_d(f)\rangle \\ \vdots \\ \langle E_n, \mathbb{H}_d(f)\rangle\end{bmatrix} = \frac{1}{\sqrt{d}}\begin{bmatrix}\sqrt{d}f[1] \\ \sqrt{d}f[2] \\ \vdots \\ \sqrt{d}f[n]\end{bmatrix} = f$$

where we use $\langle E_k, \mathbb{H}_d(f)\rangle = \sqrt{d}f[k]$.

(6) For $\tilde{\Phi} \in \mathbb{R}^{n\times m}$ and $C \in \mathbb{R}^{m\times q}$ and $\tilde{\Psi} \in \mathbb{R}^{d\times q}$,

$$\mathbb{H}_d^\dagger(\tilde{\Phi}C\tilde{\Psi}^\top) = \mathbb{H}_d^\dagger\left(\tilde{\Phi}\begin{bmatrix} c_1 & \cdots & c_q\end{bmatrix}\begin{bmatrix}\tilde{\psi}_1^\top \\ \vdots \\ \tilde{\psi}_q^\top\end{bmatrix}\right)$$

$$= \sum_{j=1}^q \mathbb{H}_d^\dagger(\tilde{\Phi}c_j\tilde{\psi}_j^\top) \ . \tag{A.11}$$

Furthermore, using (A.4) and (A.5), we have

$$\mathbb{H}_d^\dagger(\tilde{\Phi}c_j\tilde{\psi}_j^\top) = \frac{1}{\sqrt{d}}\begin{bmatrix}\langle E_1, \tilde{\Phi}c_j\tilde{\psi}_j^\top\rangle \\ \langle E_2, \tilde{\Phi}c_j\tilde{\psi}_j^\top\rangle \\ \vdots \\ \langle E_n, \tilde{\Phi}c_j\tilde{\psi}_j^\top\rangle\end{bmatrix} = \frac{1}{d}\begin{bmatrix}\left(\tilde{\Phi}c_j \circledast \tilde{\psi}_j\right)[1] \\ \left(\tilde{\Phi}c_j \circledast \tilde{\psi}_j\right)[2] \\ \vdots \\ \left(\tilde{\Phi}c_j \circledast \tilde{\psi}_j\right)[n]\end{bmatrix} = \frac{1}{d}\left(\tilde{\Phi}c_j \circledast \tilde{\psi}_j\right)$$

Thus, we have

$$\mathbb{H}_d^\dagger(\tilde{\Phi}C\tilde{\Psi}^\top) = \frac{1}{d}\sum_{j=1}^q \left(\tilde{\Phi}c_j \circledast \tilde{\psi}_j\right) \ .$$

Finally, (A.7) can be readily obtained by noting that

$$\tilde{\Phi}c_j = \sum_{i=1}^m \tilde{\phi}_i c_{ij} \quad .$$

(7) We need to show that the operator L defined by (A.8) satisfies the left inverse condition, i.e. we should show that $L\left(\mathbb{H}_{d|p}(X)\right) = X$ for any $X = [x_1, \cdots, x_p] \in \mathbb{R}^{n\times p}$. This can be shown because we have

$$\begin{aligned} L(\mathbb{H}_{d|p}(X)) &= L\left(\begin{bmatrix}\mathbb{H}_d(x_1) & \cdots & \mathbb{H}_d(x_p)\end{bmatrix}\right) \\ &= \begin{bmatrix}\mathbb{H}_d^\dagger(\mathbb{H}(x_1)) & \cdots & \mathbb{H}_d^\dagger(\mathbb{H}(x_p))\end{bmatrix} \\ &= \begin{bmatrix}x_1 & \cdots & x_p\end{bmatrix} = X \ , \end{aligned}$$

where the first equality uses the definition of $\mathbb{H}_{d|p}(X)$ and the second equality comes from the definition of L and the last equality is from $\mathbb{H}_d^\dagger$ being the generalized inverse of $\mathbb{H}_d$.

(8) Since $f \in \mathbb{R}^n$ and $\Psi, \tilde{\Psi} \in \mathbb{R}^{d\times q}$, we have

$$\mathbb{H}_d^\dagger(\mathbb{H}_d(f)\Psi\tilde{\Psi}^\top) = \frac{1}{d}\sum_{i=1}^q \left(\mathbb{H}_d(f)\psi_i \circledast \tilde{\psi}_i\right) = \frac{1}{d}\sum_{i=1}^q (f \circledast \overline{\psi}_i \circledast \tilde{\psi}_i) \quad \in \mathbb{R}^n \ .$$

where the first equality comes from (A.6) and the last equality comes from (2).

(9) Since $\tilde{\Xi}^\top = \begin{bmatrix}\tilde{\Xi}_1^\top & \cdots & \tilde{\Xi}_p^\top\end{bmatrix} \in \mathbb{R}^{pq\times pd}$ with $\tilde{\Xi}_i^\top \in \mathbb{R}^{pq\times d}$, we have

$$\mathbb{H}_{d|p}\left([f_1, \cdots, f_p]\right)\Xi\tilde{\Xi}^\top = \begin{bmatrix}\mathbb{H}_{d|p}\left([f_1, \cdots, f_p]\right)\Xi\tilde{\Xi}_1^\top & \cdots & \mathbb{H}_{d|p}\left([f_1, \cdots, f_p]\right)\Xi\tilde{\Xi}_p^\top\end{bmatrix},$$

where $\mathbb{H}_{d|p}\left([f_1, \cdots, f_p]\right)\Xi\tilde{\Xi}_i^\top \in \mathbb{R}^{n\times d}$ for $i = 1, \cdots, p$. Thus, we have

$$\begin{aligned} \mathbb{H}_{d|p}^\dagger(\mathbb{H}_{d|p}([f_1, \cdots, f_p])\Xi\tilde{\Xi}^\top) &= \left[\mathbb{H}_d^\dagger\left(\mathbb{H}_{d|p}\left([f_1, \cdots, f_p]\right)\Xi\tilde{\Xi}_1^\top\right) \quad \cdots \quad \mathbb{H}_d^\dagger\left(\mathbb{H}_{d|p}\left([f_1, \cdots, f_p]\right)\Xi\tilde{\Xi}_p^\top\right)\right] \\ &= \frac{1}{d}\sum_{i=1}^q \left[\mathbb{H}_{d|p}\left([f_1, \cdots, f_p]\right)\bar{\xi}_i \circledast \tilde{\xi}_i^1 \quad \cdots \quad \mathbb{H}_{d|p}\left([f_1, \cdots, f_p]\right)\xi_i \circledast \tilde{\xi}_i^p\right] \\ &= \frac{1}{d}\sum_{i=1}^q \sum_{j=1}^p \left[f_j \circledast \overline{\xi}_i^j \circledast \tilde{\xi}_i^1, \quad \cdots \quad f_j \circledast \overline{\xi}_i^j \circledast \tilde{\xi}_i^p\right] \ . \end{aligned}$$

where the first equality comes from (A.8) and the second equality is from (A.6), and the last equality is due to (5). Q.E.D. ∎

Appendix B. Proof of Theorem 6.

By converting (58) and (59) to Hankel operator forms, we have

$$\begin{aligned}\hat{Z} &= \mathbb{H}^{\dagger}_{d|p}(\tilde{\Phi}C\tilde{\Psi}^{\top}) + 1_n b_{dec}^{\top} \\ &= \mathbb{H}^{\dagger}_{d|p}\left(\tilde{\Phi}(\Phi^{\top}\mathbb{H}_{d|p}(Z)\Psi + \Phi^{\top}1_n b_{enc}^{\top})\tilde{\Psi}^{\top}\right) + 1_n b_{dec}^{\top} \\ &= \mathbb{H}^{\dagger}_{d|p}\left(\mathbb{H}_{d|p}(Z)\right) + \mathbb{H}^{\dagger}_{d|p}\left(1_n b_{enc}^{\top}\tilde{\Psi}^{\top}\right) + 1_n b_{dec}^{\top} \\ &= Z + \mathbb{H}^{\dagger}_{d|p}\left(1_n b_{enc}^{\top}\tilde{\Psi}^{\top}\right) + 1_n b_{dec}^{\top} \qquad \text{(B.1)}\end{aligned}$$

where we use the frame condition (38) for the third quality. Thus, to satisfy PR, i.e. $\hat{Z} = Z$,we have

$$1_n b_{dec}^{\top} = -\mathbb{H}^{\dagger}_{d|p}\left(1_n b_{enc}^{\top}\tilde{\Psi}^{\top}\right),$$

which concludes the first part. Next, due to the block structure of $\tilde{\Psi}$ in (48), we have

$$b_{enc}^{\top}\tilde{\Psi}^{\top} = \begin{bmatrix} a_1^{\top} & \cdots & a_p^{\top}\end{bmatrix}, \quad \text{where} \quad a_i = \tilde{\Psi}_i b_{enc},\ i = 1, \cdots, p$$

Accordingly, using (A.8) and (A.6) we have

$$\begin{aligned}\mathbb{H}^{\dagger}_{d|p}\left(1_n \begin{bmatrix} a_1^{\top} & \cdots & a_p^{\top}\end{bmatrix}\right) &= \begin{bmatrix}\mathbb{H}_d(1_n a_1^{\top}) & \cdots & \mathbb{H}_d(1_n a_p^{\top})\end{bmatrix} \\ &= \begin{bmatrix} 1_n \circledast a_1 & \cdots & 1_n \circledast a_p\end{bmatrix} \\ &= 1_n \begin{bmatrix} 1_d^{\top} a_1 & \cdots & 1_d^{\top} a_p\end{bmatrix}\end{aligned}$$

where the last equality comes from

$$1_n \circledast a_i = \mathbb{H}_d(1_n)a_i = 1_n(1_d^{\top} a_i).$$

From (B.1), we therefore have

$$\hat{Z} = Z + 1_n \begin{bmatrix} 1_d^{\top} a_1 & \cdots & 1_d^{\top} a_p\end{bmatrix} + 1_n b_{dec}^{\top}.$$

Thus, to satisfy PR, i.e. $\hat{Z} = Z$, the decoder bias should be

$$b_{dec}^{\top} = -\begin{bmatrix} 1_d^{\top} a_1 & \cdots & 1_d^{\top} a_p\end{bmatrix} = -\begin{bmatrix} 1_d^{\top}\tilde{\Psi}_1 b_{enc} & \cdots & 1_d^{\top}\tilde{\Psi}_p b_{enc}\end{bmatrix}.$$

This concludes the proof.

Appendix C. Proof of Proposition 7.

From (53) and (52), we have

$$\begin{aligned} Z &= \left(\tilde{\Phi}C\right) \circledast \nu(\tilde{\Psi}) \\ &= \left(\tilde{\Phi}\Phi^{\top}\left(Z \circledast \overline{\Psi}\right)\right) \circledast \nu(\tilde{\Psi}) \\ &= \left(Z \circledast \overline{\Psi}\right) \circledast \nu(\tilde{\Psi}) \\ &= \mathbb{H}^{\dagger}_{d|p}\left(\mathbb{H}_{d|p}(Z)\Psi\tilde{\Psi}^{\top}\right)\end{aligned}$$

Thus, (A.10) informs that

$$\begin{aligned} Z := [z_1, \cdots, z_p] &= \mathbb{H}^{\dagger}_{d|p}(\mathbb{H}_{d|p}([z_1, \cdots, z_p])\Psi\tilde{\Psi}^{\top}) \\ &= \frac{1}{d}\sum_{i=1}^{q}\sum_{j=1}^{p}\left[z_j \circledast \overline{\psi}_i^j \circledast \tilde{\psi}_i^1, \quad \cdots, \quad z_j \circledast \overline{\psi}_i^j \circledast \tilde{\psi}_i^p\right].\end{aligned}$$

By taking the Fourier transform, we have

$$\hat{z}_k = \frac{1}{d}\sum_{i=1}^{q}\sum_{j=1}^{p} \hat{z}_j \widehat{\psi_i^j}^* \widehat{\tilde{\psi}_i^k}, \qquad k = 1, \cdots, p \tag{C.1}$$

because the Fourier transform of the flipped signal is equal to the complex conjugate of the original signal. Finally, (C.1) can be represented by a matrix representation form:

$$Z = Z\frac{1}{d}\begin{bmatrix} \widehat{\psi_1^1}^* & \cdots & \widehat{\psi_q^1}^* \\ \vdots & \ddots & \vdots \\ \widehat{\psi_1^p}^* & \cdots & \widehat{\psi_q^p}^* \end{bmatrix}\begin{bmatrix} \widehat{\tilde{\psi}_1^1} & \cdots & \widehat{\tilde{\psi}_1^p} \\ \vdots & \ddots & \vdots \\ \widehat{\tilde{\psi}_q^1} & \cdots & \widehat{\tilde{\psi}_q^p} \end{bmatrix}$$

which is equivalent to the condition Eq. (64). For the proof of (65), note that the PR condition (56) and (55) is for $p = 1$. Thus, Eq. (64) is reduced to

$$1 = \frac{1}{d}\begin{bmatrix} \widehat{\psi_1^1}^* & \cdots & \widehat{\psi_q^1}^* \end{bmatrix}\begin{bmatrix} \widehat{\tilde{\psi}_1^1} \\ \vdots \\ \widehat{\tilde{\psi}_q^1} \end{bmatrix} = \frac{1}{d}\sum_{i=1}^{q} \widehat{\psi_i^1}^* \widehat{\tilde{\psi}_i^1},$$

which proves (65). Finally, for (66), note that $\tilde{\psi}_i = \psi_i$ for the orthonormal basis. Thus, (65) is reduced to (66). This concludes the proof.

Appendix D. Proof of Proposition 8.

We prove this by mathematical induction. At $l = 1$, the input signal is $f \in \mathbb{R}^n$, so we need $\Phi^{(1)\top}\mathbb{H}_{d_{(1)}}(f)\Psi^{(1)}$ to obtain the filtered signal $C^{(1)}$. Since $\mathbb{H}_{d_{(1)}}(f) \in \mathbb{R}^{n\times d_{(1)}}$, the dimension of the local basis matrix should be $\Psi^{(1)} \in \mathbb{R}^{d_{(1)}\times q_{(1)}}$ with $q_{(1)} \geq d_{(1)}$ to satisfy the frame condition (39). Next, we assume that (67) is true at the $(l-1)$-th layer. Then, the number of input channel at the l-layer is $p_{(l)} = q_{(l-1)}$ and the filtering operation can be represented by (9) or $\Phi^{(l)\top}\mathbb{H}_{d_{(l)}|p_{(l)}}(C^{(l-1)})\Psi^{(l)}$, where $\mathbb{H}_{d_{(l)}|p_{(l)}}(C^{(l-1)}) \in \mathbb{R}^{n\times p_{(l)}d_{(l)}}$. Thus, to guarantee the PR, the number of columns for the local basis $\Psi^{(l)}$ should be at least $p_{(l)}d_{(l)}$ to satisfy the frame condition (39). This implies that the output channel number at the l-th layer should be $q_{(l)} \geq p_{(l)}d_{(l)} = q_{(l-1)}d_{(l)}$. This concludes the proof.

Appendix E. Proof of Proposition 9.

Note that the extended Hankel matrix $\mathbb{H}_{d_{(l)}|p_{(l)}}(C^{(l-1)})$ in (63) has the following decomposition:

$$\mathbb{H}_{d_{(l)}|p_{(l)}}(C^{(l-1)}) = \mathbb{H}_{n|p_{(l-1)}}(C^{(l-2)})\mathfrak{C}_{d_{(l)}}\left(\Psi^{(l-1)}\right) .$$

Here,

$$\mathfrak{C}_{d_{(l)}}\left(\Psi^{(l-1)}\right) := \overbrace{\begin{bmatrix} \mathfrak{C}_{d_{(l)}}(\overline{\psi}_1^1) & \cdots & \mathfrak{C}_{d_{(l)}}(\overline{\psi}_{q_{(l-1)}}^1) \\ \vdots & \ddots & \vdots \\ \mathfrak{C}_{d_{(l)}}(\overline{\psi}_1^{p_{(l-1)}}) & \cdots & \mathfrak{C}_{d_{(l)}}(\overline{\psi}_{q_{(l-1)}}^{p_{(l-1)}}) \end{bmatrix}}^{d_{(l)}q_{(l-1)}=d_{(l)}p_{(l)}} \tag{E.1}$$

where $\mathfrak{C}_d(h) \in \mathbb{R}^{n\times d}$ is defined in (30). Due to the rank inequality $\text{RANK}(AB) \leq \min\{\text{RANK}(A), \text{RANK}(B)\}$, we have

$$\begin{aligned} \text{RANK}\mathbb{H}_{d_{(l)}|p_{(l)}}(C^{(l-1)}) &\leq \min\left\{\text{RANK}\mathbb{H}_{n|p_{(l-1)}}(C^{(l-2)}), \text{RANK}(\mathfrak{C}_{d_{(l)}}\left(\Psi^{(l-1)}\right))\right\} \\ &\leq \min\left\{\text{RANK}\mathbb{H}_{n|p_{(l-1)}}(C^{(l-2)}), d_{(l)}p_{(l)}\right\} \end{aligned} \tag{E.2}$$

Similarly, we have

$$\mathbb{H}_{n|p_{(l)}}(C^{(l-1)}) = \mathbb{H}_{n|p_{(l-1)}}(C^{(l-2)})\mathfrak{C}_n\left(\Psi^{(l-1)}\right)$$

where $\mathfrak{C}_n\left(\Psi^{(l-1)}\right)$ can be constructed using the definition in (E.1). Thus, we have

$$\text{RANK}\mathbb{H}_{n|p_{(l)}}(C^{(l-1)}) \leq \min\left\{\text{RANK}\mathbb{H}_{n|p_{(l-1)}}(C^{(l-2)}), np_{(l)}\right\} \leq \text{RANK}\mathbb{H}_{n|p_{(l-1)}}(C^{(l-2)}) \tag{E.3}$$

since $np_{(l-1)} \leq np_{(l)}$. By recursively applying the inequality (E.3) with (E.2), we have

$$\text{RANK}\mathbb{H}_{d_{(l)}|p_{(l)}}(C^{(l-1)}) \leq \min\{\mathbb{H}_n(f), d_{(l)}p_{(l)}\}.$$

This concludes the proof.

Appendix F. Proof of Proposition 10.

We will prove by construction. Let $F^{(l)} := \mathbb{H}_{d_{(l)}|p_{(l)}}(C^{(l)})$. Because $\Phi^{(l)\top}\left(F^{(l)}(-\Psi_+^{(l)}) - 1_n b_{enc,+}^{(l)\top}\right) = -\Phi^{(l)\top}\left(F^{(l)}\Psi_+^{(l)} + 1_n b_{enc,+}^{(l)\top}\right)$, the negative part can be retrieved from $-\rho\left(\Phi^{(l)\top}\left(F^{(l)}(-\Psi_+^{(l)}) - 1_n b_{enc,+}^{(l)\top}\right)\right)$, while the positive part of $\Phi^{(l)\top}\left(F^{(l)}\Psi_+^{(l)} + 1_n b_{enc,+}^{(l)\top}\right)$ can be retained from $\rho\left(\Phi^{(l)\top}\left(F^{(l)}\Psi_+^{(l)} + 1_n b_{enc,+}^{(l)\top}\right)\right)$. Furthermore, their non-zero parts do not overlap. Thus,

$$\Phi^{(l)\top}\left(F^{(l)}\Psi_+^{(l)} + 1_n b_{enc,+}^{(l)\top}\right) = \rho\left(\Phi^{(l)\top}\left(F^{(l)}\Psi_+^{(l)} + 1_n b_{enc,+}^{(l)\top}\right)\right) - \rho\left(\Phi^{(l)\top}\left(F^{(l)}(-\Psi_+^{(l)}) - 1_n b_{enc,+}^{(l)\top}\right)\right) . \tag{F.1}$$

Accordingly, by choosing (73) and (75), we have

$$\begin{aligned}
&\tilde{\Phi}^{(l)}\rho\left(\Phi^{(l)\top}F^{(l)}\Psi^{(l)} + 1_n b_{enc,+}^{(l)\top}\right)\tilde{\Psi}^{(l)\top} \\
&= \tilde{\Phi}^{(l)}\left[\rho\left(\Phi^{(l)\top}\left(F^{(l)}\Psi_+^{(l)} + 1_n b_{enc,+}^{(l)\top}\right)\right) \quad \rho\left(\Phi^{(l)\top}\left(F^{(l)}(-\Psi_+^{(l)}) - 1_n b_{enc,+}^{(l)\top}\right)\right)\right]\begin{bmatrix}\tilde{\Psi}_+^{(l)\top} \\ -\tilde{\Psi}_+^{(l)\top}\end{bmatrix} \\
&= \tilde{\Phi}^{(l)}\left(\rho\left(\Phi^{(l)\top}\left(F^{(l)}\Psi_+^{(l)} + 1_n b_{enc,+}^{(l)\top}\right)\right) - \rho\left(\Phi^{(l)\top}\left(F^{(l)}(-\Psi_+^{(l)}) - 1_n b_{enc,+}^{(l)\top}\right)\right)\right)\tilde{\Psi}_+^{(l)\top} \\
&= \tilde{\Phi}^{(l)}\Phi^{(l)\top}\left(F^{(l)}\Psi_+^{(l)}\tilde{\Psi}_+^{(l)\top} + 1_n b_{enc,+}^{(l)\top}\tilde{\Psi}_+^{(l)\top}\right) \\
&= F^{(l)} + 1_n b_{enc,+}^{(l)\top}\tilde{\Psi}_+^{(l)\top}
\end{aligned}$$

where we use (F.1) for the third inequality and the last equality comes from (74). Finally, we have

$$\begin{aligned}
\hat{C}^{(l)} &= \mathbb{H}^{\dagger}_{d_{(l)}|p_{(l)}}\left(F^{(l)} + 1_n b_{enc,+}^{(l)\top}\tilde{\Psi}_+^{(l)\top}\right) + 1_n b_{dec}^{(l)\top} \\
&= C^{(l)} + \mathbb{H}^{\dagger}_{d_{(l)}|p_{(l)}}\left(1_n b_{enc,+}^{(l)\top}\tilde{\Psi}_+^{(l)\top}\right) + 1_n b_{dec}^{(l)\top} \\
&= C^{(l)}
\end{aligned}$$

where the last equality comes from (75). By applying this from $l = L$ to 1 in (70), we can see that $f = \mathcal{Q}\left(f; \{\Phi^{(j)}, \tilde{\Phi}^{(j)}\}_{j=1}^{L}\right)$. Q.E.D.

Appendix G. Proof of Proposition 11.

We will prove by construction. From the proof of Proposition 10, we know that

$$\Phi\rho\left(\Phi^{\top}\mathbb{H}_{d|p}(X)[\Psi_+ \ -\Psi_+]\right)\begin{bmatrix}\tilde{\Psi}_+^{\top} \\ -\tilde{\Psi}_+^{\top}\end{bmatrix} = \Phi\Phi^{\top}\mathbb{H}_{d|p}(X)\Psi_+\tilde{\Psi}_+^{\top} = \mathbb{H}_{d|p}(X)\Psi_+\tilde{\Psi}_+^{\top} \quad ,$$

where the last equality comes from the orthonormality of Φ. Since $m \geq r$, there always exist $\Psi_+, \tilde{\Psi}_+ \in \mathbb{R}^{pd\times m}$ such that $\Psi_+\tilde{\Psi}_+ = P_{R(V)}$ where $V \in \mathbb{R}^{pd\times r}$ denotes the right singular vectors of $\mathbb{H}_{d|p}(X)$. Thus,

$$\Phi\rho\left(\Phi^\top \mathbb{H}_{d|p}(X)\Psi\right)\tilde{\Psi}^\top = \mathbb{H}_{d|p}(X)P_{R(V)} = \mathbb{H}_{d|p}(X).$$

By applying $\mathbb{H}^\dagger_{d|p}$ to both side, we conclude the proof.

Appendix H. Proof of Proposition 12. Again the proof can be done by construction. Specifically, from the proof of Proposition 10, we know that

$$\rho\left(\mathbb{H}_{d|p}(X)[\Psi_+ \ -\Psi_+]\right)\begin{bmatrix}\tilde{\Psi}_+^\top \\ -\tilde{\Psi}_+^\top\end{bmatrix} = \mathbb{H}_{d|p}(X)\Psi_+\tilde{\Psi}_+^\top = \mathbb{H}_{d|p}(X)\Psi_+\tilde{\Psi}_+^\top \quad .$$

Thus,

$$\mathbb{H}_{d|p}(X) - R(F;\Phi,\Psi_+,\tilde{\Psi}_+) = \mathbb{H}_{d|p}(X) - \rho\left(\ \mathbb{H}_{d|p}(X) - \mathbb{H}_{d|p}(X)(\Psi_+\tilde{\Psi}_+^\top)\right)$$

Thus, if we choose Ψ_+ such that $V^\top\Psi_+ = 0$, we have

$$\mathbb{H}_{d|p}(X) - R(F;\Phi,\Psi_+,\tilde{\Psi}_+) = \mathbb{H}_{d|p}(X) - \rho\left(\mathbb{H}_{d|p}(X)\right) = 0$$

where the last equality comes from the non-negativity of X. Thus, we can guarantee (78). Now, the remaining issue to prove is the existence of Ψ_+ such that $V^\top\Psi_+ = 0$. This is always possible if $r < pd$. This concludes the proof.

REFERENCES

[1] Martín Abadi, Ashish Agarwal, Paul Barham, Eugene Brevdo, Zhifeng Chen, Craig Citro, Greg S Corrado, Andy Davis, Jeffrey Dean, Matthieu Devin, et al., *Tensorflow: Large-scale machine learning on heterogeneous distributed systems*, arXiv preprint arXiv:1603.04467, (2016).

[2] Eirikur Agustsson and Radu Timofte, *NTIRE 2017 Challenge on Single Image Super-Resolution: Dataset and Study*, in The IEEE Conference on Computer Vision and Pattern Recognition (CVPR) Workshops, July 2017.

[3] Martin Anthony and Peter L Bartlett, *Neural network learning: Theoretical foundations*, cambridge university press, 2009.

[4] Woong Bae, Jaejoon Yoo, and Jong Chul Ye, *Beyond deep residual learning for image restoration: Persistent homology-guided manifold simplification*, (2017).

[5] Peter L Bartlett and Shahar Mendelson, *Rademacher and Gaussian complexities: Risk bounds and structural results*, Journal of Machine Learning Research, 3 (2002), pp. 463–482.

[6] Heinz H Bauschke and Patrick L Combettes, *Convex analysis and monotone operator theory in Hilbert spaces*, Springer, 2011.

[7] Joan Bruna and Stéphane Mallat, *Invariant scattering convolution networks*, IEEE transactions on Pattern Analysis and Machine Intelligence, 35 (2013), pp. 1872–1886.

[8] Antoni Buades, Bartomeu Coll, and J-M Morel, *A non-local algorithm for image denoising*, in Computer Vision and Pattern Recognition, 2005. CVPR 2005. IEEE Computer Society Conference on, vol. 2, IEEE, 2005, pp. 60–65.

[9] Harold C Burger, Christian J Schuler, and Stefan Harmeling, *Image denoising: Can plain neural networks compete with BM3D?*, in 2012 IEEE Conference on Computer Vision and Pattern Recognition (CVPR), IEEE, 2012, pp. 2392–2399.

[10] Jian-Feng Cai, Raymond H Chan, Lixin Shen, and Zuowei Shen, *Convergence analysis of tight framelet approach for missing data recovery*, Advances in Computational Mathematics, 31 (2009), pp. 87–113.

[11] Jian-Feng Cai, Raymond H Chan, and Zuowei Shen, *A framelet-based image inpainting algorithm*, Applied and Computational Harmonic Analysis, 24 (2008), pp. 131–149.

[12] Jian-Feng Cai, Bin Dong, Stanley Osher, and Zuowei Shen, *Image restoration: Total variation, wavelet frames, and beyond*, Journal of the American Mathematical Society, 25 (2012), pp. 1033–1089.

[13] Jian-Feng Cai, Stanley Osher, and Zuowei Shen, *Split Bregman methods and frame based image restoration*, Multiscale Modeling & Simulation, 8 (2009), pp. 337–369.

[14] E. Candes, J. Romberg, and T. Tao, *Robust uncertainty principles: Exact signal reconstruction from highly incomplete frequency information*, IEEE Trans. on Information Theory, 52 (2006), pp. 489–509.

[15] Yunjin Chen, Wei Yu, and Thomas Pock, *On learning optimized reaction diffusion processes for effective image restoration*, in Proceedings of the IEEE Conference on Computer Vision and Pattern Recognition, 2015, pp. 5261–5269.

[16] Kostadin Dabov, Alessandro Foi, Vladimir Katkovnik, and Karen Egiazarian, *Image denoising by sparse 3-D transform-domain collaborative filtering*, IEEE Transactions on image processing, 16 (2007), pp. 2080–2095.
[17] Ingrid Daubechies, *Ten lectures on wavelets*, SIAM, 1992.
[18] Ingrid Daubechies, Bin Han, Amos Ron, and Zuowei Shen, *Framelets: MRA-based constructions of wavelet frames*, Applied and omputational Harmonic Analysis, 14 (2003), pp. 1–46.
[19] D. L. Donoho, *Compressed sensing*, IEEE Trans. on Information Theory, 52 (2006), pp. 1289–1306.
[20] David L Donoho, *Compressed sensing*, IEEE Transactions on information theory, 52 (2006), pp. 1289–1306.
[21] Maryam Fazel, Ting Kei Pong, Defeng Sun, and Paul Tseng, *Hankel matrix rank minimization with applications to system identification and realization*, SIAM Journal on Matrix Analysis and Applications, 34 (2013), pp. 946–977.
[22] Xavier Glorot, Antoine Bordes, and Yoshua Bengio, *Deep sparse rectifier neural networks.*, in Aistats, vol. 15, 2011, p. 275.
[23] Klaus Greff, Rupesh K Srivastava, and Jürgen Schmidhuber, *Highway and residual networks learn unrolled iterative estimation*, arXiv preprint arXiv:1612.07771, (2016).
[24] Karol Gregor and Yann LeCun, *Learning fast approximations of sparse coding*, in Proceedings of the 27th International Conference on Machine Learning (ICML-10), 2010, pp. 399–406.
[25] K Hammernik, F Knoll, D Sodickson, and T Pock, *Learning a variational model for compressed sensing MRI reconstruction*, in Proceedings of the International Society of Magnetic Resonance in Medicine (ISMRM), 2016.
[26] Dongyoon Han, Jiwhan Kim, and Junmo Kim, *Deep pyramidal residual networks*, arXiv preprint arXiv:1610.02915, (2016).
[27] Yoseob Han, Jawook Gu, and Jong Chul Ye, *Deep learning interior tomography for region-of-interest reconstruction*, arXiv preprint arXiv:1712.10248, (2017).
[28] Yoseob Han and Jong Chul Ye, *Framing U-Net via deep convolutional framelets: Application to sparse-view CT*, arXiv preprint arXiv:1708.08333, (2017).
[29] Yoseop Han, Jaejoon Yoo, and Jong Chul Ye, *Deep residual learning for compressed sensing CT reconstruction via persistent homology analysis*, arXiv preprint arXiv:1611.06391, (2016).
[30] Yoseob Han, Jaejun Yoo, and Jong Chul Ye, *Deep learning with domain adaptation for accelerated projection reconstruction MR*, Magnetic Resonance in Medicine (in press), available also as arXiv preprint arXiv:1703.01135, (2018).
[31] Kaiming He, Xiangyu Zhang, Shaoqing Ren, and Jian Sun, *Delving deep into rectifiers: Surpassing human-level performance on imagenet classification*, in Proceedings of the IEEE International Conference on Computer Vision, 2015, pp. 1026–1034.
[32] ———, *Deep residual learning for image recognition*, in Proceedings of the IEEE Conference on Computer Vision and Pattern Recognition, 2016, pp. 770–778.
[33] Yingbo Hua and Tapan K Sarkar, *Matrix pencil method for estimating parameters of exponentially damped/undamped sinusoids in noise*, IEEE Transactions on Acoustics, Speech, and Signal Processing, 38 (1990), pp. 814–824.
[34] Kyong Hwan Jin, Dongwook Lee, and Jong Chul Ye, *A general framework for compressed sensing and parallel MRI using annihilating filter based low-rank hankel matrix*, IEEE Trans. on Computational Imaging, 2 (2016), pp. 480–495.
[35] Kyong Hwan Jin, Michael T McCann, Emmanuel Froustey, and Michael Unser, *Deep convolutional neural network for inverse problems in imaging*, arXiv preprint arXiv:1611.03679, (2016).
[36] Kyong Hwan Jin, Ji-Yong Um, Dongwook Lee, Juyoung Lee, Sung-Hong Park, and Jong Chul Ye, *MRI artifact correction using sparse+ low-rank decomposition of annihilating filter-based hankel matrix*, Magnetic Resonance in Medicine, 78 (2017), pp. 327–340.
[37] Kyong Hwan Jin and Jong Chul Ye, *Annihilating filter-based low-rank Hankel matrix approach for image inpainting*, IEEE Transactions on Image Processing, 24 (2015), pp. 3498–3511.
[38] ———, *Sparse and low rank decomposition of annihilating filter-based Hankel matrix for impulse noise removal*, IEEE Transactions on Image Processing (in press), (2017).
[39] Eunhee Kang, Junhong Min, and Jong Chul Ye, *A deep convolutional neural network using directional wavelets for low-dose x-ray CT reconstruction*, Medical Physics, 44 (2017).
[40] Eunhee Kang, Jong Chul Ye, et al., *Wavelet domain residual network (WavResNet) for low-dose x-ray CT reconstruction*, arXiv preprint arXiv:1703.01383, (2017).
[41] Eunhee Kang, Jaejun Yoo, and Jong Chul Ye, *Wavelet residual network for low-dose CT via deep convolutional framelets*, arXiv preprint arXiv:1707.09938, (2017).
[42] Jiwon Kim, Jung Kwon Lee, and Kyoung Mu Lee, *Accurate image super-resolution using very deep convolutional networks*, arXiv preprint arXiv:1511.04587, (2015).
[43] Diederik Kingma and Jimmy Ba, *Adam: A method for stochastic optimization*, arXiv preprint arXiv:1412.6980, (2014).
[44] Alex Krizhevsky, Ilya Sutskever, and Geoffrey E Hinton, *Imagenet classification with deep convolutional neural networks*, in Advances in Neural Information Processing Systems, 2012, pp. 1097–1105.
[45] Kinam Kwon, Dongchan Kim, and HyunWook Park, *A parallel MR imaging method using multilayer perceptron*, Medical Physics, (2017).
[46] K Kwon, D Kim, H Seo, J Cho, B Kim, and HW Park, *Learning-based reconstruction using artificial neural*

network for higher acceleration, in Proceedings of the International Society of Magnetic Resonance in Medicine (ISMRM), 2016.
[47] Yann LeCun, Yoshua Bengio, and Geoffrey Hinton, *Deep learning*, Nature, 521 (2015), pp. 436–444.
[48] Dongwook Lee, Kyong Hwan Jin, Eung Yeop Kim, Sung-Hong Park, and Jong Chul Ye, *Acceleration of MR parameter mapping using annihilating filter-based low rank hankel matrix (ALOHA)*, Magnetic resonance in medicine, 76 (2016), pp. 1848–1868.
[49] Juyoung Lee, Kyong Hwan Jin, and Jong Chul Ye, *Reference-free single-pass EPI Nyquist ghost correction using annihilating filter-based low rank Hankel matrix (ALOHA)*, Magnetic resonance in medicine, 76 (2016), pp. 1775–1789.
[50] Stéphane Mallat, *A wavelet tour of signal processing*, Academic press, 1999.
[51] ———, *Group invariant scattering*, Communications on Pure and Applied Mathematics, 65 (2012), pp. 1331–1398.
[52] Xiaojiao Mao, Chunhua Shen, and Yu-Bin Yang, *Image restoration using very deep convolutional encoder-decoder networks with symmetric skip connections*, in Advances in Neural Information Processing Systems, 2016, pp. 2802–2810.
[53] Junhong Min, Lina Carlini, Michael Unser, Suliana Manley, and Jong Chul Ye, *Fast live cell imaging at nanometer scale using annihilating filter-based low-rank Hankel matrix approach*, in SPIE Optical Engineering+ Applications, International Society for Optics and Photonics, 2015, pp. 95970V–95970V.
[54] Hyeonwoo Noh, Seunghoon Hong, and Bohyung Han, *Learning deconvolution network for semantic segmentation*, in Proceedings of the IEEE International Conference on Computer Vision, 2015, pp. 1520–1528.
[55] Greg Ongie and Mathews Jacob, *Off-the-grid recovery of piecewise constant images from few fourier samples*, SIAM Journal on Imaging Sciences, 9 (2016), pp. 1004–1041.
[56] Vardan Papyan, Yaniv Romano, and Michael Elad, *Convolutional neural networks analyzed via convolutional sparse coding*, Journal of Machine Learning Research, 18 (2017), pp. 1–52.
[57] Deepak Pathak, Philipp Krahenbuhl, Jeff Donahue, Trevor Darrell, and Alexei A Efros, *Context encoders: Feature learning by inpainting*, in Proceedings of the IEEE Conference on Computer Vision and Pattern Recognition, 2016, pp. 2536–2544.
[58] Ben Poole, Subhaneil Lahiri, Maithreyi Raghu, Jascha Sohl-Dickstein, and Surya Ganguli, *Exponential expressivity in deep neural networks through transient chaos*, in Advances In Neural Information Processing Systems, 2016, pp. 3360–3368.
[59] Olaf Ronneberger, Philipp Fischer, and Thomas Brox, *U-net: Convolutional networks for biomedical image segmentation*, in International Conference on Medical Image Computing and Computer-Assisted Intervention, Springer, 2015, pp. 234–241.
[60] Wenling Shang, Kihyuk Sohn, Diogo Almeida, and Honglak Lee, *Understanding and improving convolutional neural networks via concatenated rectified linear units*, in International Conference on Machine Learning, 2016, pp. 2217–2225.
[61] Wenzhe Shi, Jose Caballero, Ferenc Huszár, Johannes Totz, Andrew P Aitken, Rob Bishop, Daniel Rueckert, and Zehan Wang, *Real-time single image and video super-resolution using an efficient subpixel convolutional neural network*, in Proceedings of the IEEE Conference on Computer Vision and Pattern Recognition, 2016, pp. 1874–1883.
[62] Emil Y Sidky and Xiaochuan Pan, *Image reconstruction in circular cone-beam computed tomography by constrained, total-variation minimization*, Physics in medicine and biology, 53 (2008), p. 4777.
[63] Matus Telgarsky, *Benefits of depth in neural networks*, in JMLR: Workshop and Conference Proceedings, 2016, pp. 1–23.
[64] Lang Tong, Guanghan Xu, and Thomas Kailath, *Blind identification and equalization based on second-order statistics: A time domain approach*, IEEE Transactions on information Theory, 40 (1994), pp. 340–349.
[65] Andrea Vedaldi and Karel Lenc, *Matconvnet: Convolutional neural networks for Matlab*, in Proceedings of the 23rd ACM international conference on Multimedia, ACM, 2015, pp. 689–692.
[66] Martin Vetterli, Pina Marziliano, and Thierry Blu, *Sampling signals with finite rate of innovation*, IEEE Transactions on Signal Processing, 50 (2002), pp. 1417–1428.
[67] Shanshan Wang, Zhenghang Su, Leslie Ying, Xi Peng, Shun Zhu, Feng Liang, Dagan Feng, and Dong Liang, *Accelerating magnetic resonance imaging via deep learning*, in 2016 IEEE 13th International Symposium on Biomedical Imaging (ISBI), IEEE, 2016, pp. 514–517.
[68] Zhou Wang, Alan C Bovik, Hamid R Sheikh, and Eero P Simoncelli, *Image quality assessment: from error visibility to structural similarity*, IEEE transactions on image processing, 13 (2004), pp. 600–612.
[69] Thomas Wiatowski and Helmut Bölcskei, *A mathematical theory of deep convolutional neural networks for feature extraction*, arXiv preprint arXiv:1512.06293, (2015).
[70] Junyuan Xie, Linli Xu, and Enhong Chen, *Image denoising and inpainting with deep neural networks*, in Advances in Neural Information Processing Systems, 2012, pp. 341–349.
[71] Bo Xin, Yizhou Wang, Wen Gao, and David Wipf, *Maximal sparsity with deep networks*, (2016), pp. 4340–4348.
[72] Jong Chul Ye, Jong Min Kim, Kyong Hwan Jin, and Kiryung Lee, *Compressive sampling using annihilating filter-based low-rank interpolation*, IEEE Transactions on Information Theory, 63 (2017), pp. 777–801.
[73] Raymond Yeh, Chen Chen, Teck Yian Lim, Mark Hasegawa-Johnson, and Minh N Do, *Semantic image inpainting with perceptual and contextual losses*, arXiv preprint arXiv:1607.07539, (2016).
[74] Rujie Yin, Tingran Gao, Yue M Lu, and Ingrid Daubechies, *A tale of two bases: Local-nonlocal regularization on image patches with convolution framelets*, SIAM Journal on Imaging Sciences, 10 (2017), pp. 711–750.
[75] Chiyuan Zhang, Samy Bengio, Moritz Hardt, Benjamin Recht, and Oriol Vinyals, *Understanding deep*

learning requires rethinking generalization, arXiv preprint arXiv:1611.03530, (2016).

[76] Kai Zhang, Wangmeng Zuo, Yunjin Chen, Deyu Meng, and Lei Zhang, *Beyond a gaussian denoiser: Residual learning of deep CNN for image denoising*, arXiv preprint arXiv:1608.03981, (2016).

[77] ———, *Beyond a gaussian denoiser: Residual learning of deep cnn for image denoising*, IEEE Transactions on Image Processing, (2017).

[78] Bo Zhu, Jeremiah Z Liu, Bruce R Rosen, and Matthew S Rosen, *Image reconstruction by domain transform manifold learning*, arXiv preprint arXiv:1704.08841, (2017).